The Astrophysical Journal, 976:71 (43pp), 2024 November 20 https://doi.org/10.3847/1538-4357/ad7fde

Optical and Radio Analysis of Systematically Classified Broad-lined Type Ic Supernovae from the Zwicky Transient Facility

Gokul P. Srinivasaragavan[1,2,3], Sheng Yang[4], Shreya Anand[5], Jesper Sollerman[6], Anna Y. Q. Ho[7], Alessandra Corsi[8], S. Bradley Cenko[2,3], Daniel Perley[9], Steve Schulze[10], Marquice Sanchez-Fleming[7], Jack Pope[7], Nikhil Sarin[11,12], Conor Omand[6,9], Kaustav K. Das[5], Christoffer Fremling[5,13], Igor Andreoni[1,2,14], Rachel Bruch[15], Kevin B. Burdge[16], Kishalay De[17,18], Avishay Gal-Yam[19], Anjasha Gangopadhyay[6], Matthew J. Graham[5], Jacob E. Jencson[8,21], Viraj Karambelkar[5], Mansi M. Kasliwal[5], S. R. Kulkarni[5], Julia Martikainen[22], Yashvi S. Sharma[5], Anastasios Tzanidakis[23], Lin Yan[13], Yuhan Yao[24,25], Eric C. Bellm[23], Steven L. Groom[26], Frank J. Masci[26], Guy Nir[24], Josiah Purdum[13], Roger Smith[13], and Niharika Sravan[27]
[1] Department of Astronomy, University of Maryland, College Park, MD 20742, USA; gsriniv2@umd.edu
[2] Joint Space-Science Institute, University of Maryland, College Park, MD 20742, USA
[3] Astrophysics Science Division, NASA Goddard Space Flight Center, 8800 Greenbelt Road, Greenbelt, MD 20771, USA
[4] Henan Academy of Sciences, Zhengzhou 450046, Henan, People's Republic of China; sheng.yang@astro.su.se
[5] Division of Physics, Mathematics and Astronomy, California Institute of Technology, Pasadena, CA 91125, USA
[6] Department of Astronomy, The Oskar Klein Center, Stockholm University, AlbaNova, 10691 Stockholm, Sweden
[7] Department of Astronomy, Cornell University, Ithaca, NY 14853, USA
[8] William H. Miller III Department of Physics and Astronomy, Johns Hopkins University, Baltimore, MD 21218, USA
[9] Astrophysics Research Institute, Liverpool John Moores University, Liverpool Science Park, 146 Brownlow Hill, Liverpool L3 5RF, UK
[10] Center for Interdisciplinary Exploration and Research in Astrophysics (CIERA), Northwestern University, 1800 Sherman Avenue, Evanston, IL 60201, USA
[11] Oskar Klein Centre for Cosmoparticle Physics, Department of Physics, Stockholm University, AlbaNova, Stockholm SE-106 91, Sweden
[12] Nordita, Stockholm University and KTH Royal Institute of Technology, Hannes Alfvéns väg 12, SE-106 91 Stockholm, Sweden
[13] Caltech Optical Observatories, California Institute of Technology, Pasadena, CA 91125, USA
[14] Astrophysics Science Division, NASA Goddard Space Flight Center, Mail Code 661, Greenbelt, MD 20771, USA
[15] Department of Particle Physics and Astrophysics, Weizmann Institute of Science, 234 Herzl St. 76100 Rehovot, Israel
[16] Department of Physics, Massachusetts Institute of Technology, Cambridge, MA 02139, USA
[17] MIT Kavli Institute for Astrophysics and Space Research, 77 Massachusetts Avenue, Cambridge, MA 02139, USA
[18] NASA Einstein Fellow
[19] Department of Particle Physics and Astrophysics, Weizmann Institute of Science, 76100 Rehovot, Israel
[20] California Institute of Technology, 1200 E. California Boulevard, Pasadena, CA 91125, USA
[21] Space Telescope Science Institute, 3700 San Martin Drive, Baltimore, MD 21218, USA
[22] Instituto de Astrofísica de Andalucía, CSIC, Granada, Spain
[23] DIRAC Institute, Department of Astronomy, University of Washington, 3910 15th Avenue NE, Seattle, WA 98195, USA
[24] Department of Astronomy, University of California, Berkeley, 501 Campbell Hall, Berkeley, CA 94720, USA
[25] Miller Institute for Basic Research in Science, 468 Donner Lab, Berkeley, CA 94720, USA
[26] IPAC, California Institute of Technology, 1200 E. California Boulevard, Pasadena, CA 91125, USA
[27] Department of Physics, Drexel University, Philadelphia, PA 19104, USA
Received 2024 August 26; revised 2024 September 24; accepted 2024 September 24; published 2024 November 13

Abstract

We study a magnitude-limited sample of 36 broad-lined type Ic supernovae (SNe Ic-BL) from the Zwicky Transient Facility Bright Transient Survey (detected between 2018 March and 2021 August), which is the largest systematic study of SNe Ic-BL done in literature thus far. We present the light curves (LCs) for each of the SNe and analyze the shape of the LCs to derive empirical parameters, along with the explosion epochs for every event. The sample has an average absolute peak magnitude in the *r* band of $\overline{M}_{\rm r,max} = -18.51 \pm 0.15$ mag. Using spectra obtained around peak light, we compute expansion velocities from the Fe II 5169 Å line for each event with high enough signal-to-noise ratio spectra, and find an average value of $\overline{v}_{\rm ph} = 16,100 \pm 1100\,{\rm km\,s^{-1}}$. We also compute bolometric LCs, study the blackbody temperature and radii evolution over time, and derive the explosion properties of the SNe. The explosion properties of the sample have average values of $\overline{M}_{\rm Ni} = 0.37^{+0.08}_{-0.06}\,M_{\odot}$, $\overline{M}_{\rm ej} = 2.45^{+0.47}_{-0.41}\,M_{\odot}$, and $\overline{E}_{\rm K} = (4.02^{+1.37}_{-1.00}) \times 10^{51}$ erg. Thirteen events have radio observations from the Very Large Array, with eight detections and five non-detections. We find that the populations that have radio detections and radio non-detections are indistinct from one another with respect to their optically inferred explosion properties, and there are no statistically significant correlations present between the events' radio luminosities and optically inferred explosion properties. This provides evidence that the explosion properties derived from optical data alone cannot give inferences about the radio properties of SNe Ic-BL and likely their relativistic jet formation mechanisms.

Unified Astronomy Thesaurus concepts: Type Ic supernovae (1730); Relativistic jets (1390)

1. Introduction

Type Ic supernovae (SNe) represent the final fate of massive stars ($M_{\rm ZAMS} \gtrsim 8\,M_{\odot}$) whose hydrogen and helium envelopes have been stripped prior to explosion (A. Gal-Yam 2017).

These SNe are part of a larger sample of stripped-envelope SNe whose progenitors are either very massive stars ($M_{\rm ZAMS} \lesssim 30\,M_{\odot}$) whose outer layers have been stripped due to stellar winds or eruptions (P. S. Conti & N. R. Walborn 1976), or less massive stars ($M_{\rm ZAMS} \gtrsim 30\,M_{\odot}$) whose outer hydrogen and/or helium layers have been stripped by binary interactions (S.-C. Yoon et al. 2010; J. D. Lyman et al. 2016; F. Taddia et al. 2018).

Optical spectra of Type Ic SNe usually display photospheric expansion velocities of up to 10,000 km s^{-1} at peak from their Fe II lines (M. Modjaz et al. 2016). A subset of these events display broader Fe II and O I lines in their spectra, corresponding to velocities between 10,000 and 30,000 km s^{-1}. These events are referred to as broad-lined Type Ic (Ic-BL) SNe and are usually found in lower metallicity environments (I. Arcavi et al. 2011; S. Schulze et al. 2021) than normal stripped-envelope SNe. Their progenitors are also younger and more massive (N. E. Sanders et al. 2012; Z. Cano 2013). The light curves (LCs) of Type Ic-BL events also rise faster than normal stripped-envelope SNe and are brighter at peak magnitude (M. R. Drout et al. 2011; Z. Cano 2013; F. Taddia et al. 2015; J. D. Lyman et al. 2016; S. J. Prentice et al. 2016). LC modeling of these events has shown that they often have a larger amount of ^{56}Ni synthesized in the explosion, and they sometimes possess explosion energies (10^{52} erg) an order of magnitude higher than normal stripped-envelope events (10^{51} erg), though, peculiarly, their ejecta masses are similar (e.g., Z. Cano 2013; F. Taddia et al. 2015; J. D. Lyman et al. 2016; S. J. Prentice et al. 2016; F. Taddia et al. 2018; C. Barbarino et al. 2021).

SNe Ic-BL challenge the standard picture associated with the standard explosion mechanism of core collapse SNe (CCSNe), as the extra energy possessed by some of these explosions necessitates a deviation from the traditional picture of neutrino irradiation from a proto-neutron star (NS) reviving the bounce-back shock in the progenitor's core. A major open question is understanding how the same amount of ejecta can lead to higher amounts of ^{56}Ni and higher kinetic energies. A hypothesized scenario is that a relativistic jet driven from the core of the progenitor's proto-NS transfers the extra energy needed to the surrounding stellar medium such that an explosion can reach the order of 10^{52} erg observed in some events (S. E. Woosley et al. 2003). In fact, Ó. Rodríguez et al. (2024) found evidence of a non-radioactive power source for the majority of stripped-envelope SNe in their sample of 54 events, including 9 SNe Ic-BL.

This scenario is supported observationally by the detection of long gamma-ray bursts (LGRBs) unambiguously associated with a handful of SNe Ic-BL. Nearly all nearby LGRBs have observationally associated SNe Ic-BL (see, e.g., T. J. Galama et al. 1998; J. Hjorth et al. 2003; E. Pian et al. 2006; A. Melandri et al. 2012; V. D'Elia et al. 2015; Z. Cano et al. 2017; A. Melandri et al. 2019; Y. D. Hu et al. 2021; A. Kumar et al. 2022; A. Rossi et al. 2022; P. K. Blanchard et al. 2023; G. P. Srinivasaragavan et al. 2023; G. P. Srinivasaragavan et al. 2024). For more distant events, non-detections are not particularly constraining (with the exception of a few events; see M. Della Valle et al. 2006; J. P. U. Fynbo et al. 2006; A. Gal-Yam et al. 2006; M. Tanga et al. 2018). This is due to a few reasons: at high redshifts, detected gamma-ray bursts (GRBs) usually have very luminous afterglows that wash out their associated SN signature in their LCs; the SN spectral peak shifts to the near-infrared at high redshifts, making it difficult to detect with optical telescopes; and Type Ic-BL SNe rarely get brighter than −20 mag, giving a constraint on how far they can be detected regardless of their associated GRB.

However, it is clear that the majority of SNe Ic-BL do not have GRB counterparts. It has been suggested that some SNe Ic-BL may produce off-axis GRBs, whose jets are initially out of our line of sight, and emerge within our viewing angle through their radio emission at later times. Studies have shown that relativistic ejecta are not fully ubiquitous to SNe Ic-BL, and viewing angle effects solely cannot account for the lack of GRBs associated with most Type Ic-BL events (A. M. Soderberg et al. 2006; A. Corsi et al. 2016, 2023). Therefore, there are possible intrinsic differences in the explosion mechanisms between jet-powered SNe Ic-BL and normal SNe Ic-BL, and understanding this dichotomy can provide important insights into the current understanding of the landscape of massive stellar explosions.

In this work, we present a sample of 36 SNe Ic-BL observed with the Zwicky Transient Facility (ZTF; E. C. Bellm et al. 2019; M. J. Graham et al. 2019; F. J. Masci et al. 2019; R. Dekany et al. 2020) and analyze their optical properties. This sample builds on the sample of ZTF's predecessor, the intermediate Palomar Transient Facility (iPTF), whose 34 SNe Ic-BL were analyzed in F. Taddia et al. (2019). This work is the largest systematic study done on SNe Ic-BL in literature thus far. In addition to presenting the sample and analyzing its optical characteristics, we perform systematic comparisons of key optical properties between events that have radio detections and non-detections to see if the optical properties of SNe Ic-BL can provide a link to their radio observations, and therefore any insight into their jet formation mechanisms.

The structure of the paper is: in Section 2 we describe how the sample was created; in Section 3 we describe the facilities used to obtain observations of our sample; in Section 4 we describe the analysis done on the photometric observations; in Section 5 we describe the analysis done on the spectroscopic observations; in Section 6 we describe the creation of bolometric LCs and their analysis; in Section 7 we describe the derivation of explosion properties; in Section 8 we describe analysis done on a subset of events with radio observations; and in Section 9 we present a summary and conclusions of the work. We also present an Appendix, where we include discovery paragraphs on every event and their full spectral sequences, as well as efforts to model the LCs that have multi-wavelength data.

2. SN Sample Description

The sample was created by compiling all of the events that passed the internal quality cuts in ZTF's Bright Transient Survey (BTS) that were spectroscopically classified as SNe Ic-BL. BTS is a magnitude-limited survey that spectroscopically classifies all SNe $\lesssim$18.5 mag at peak brightness (C. Fremling et al. 2020; D. A. Perley et al. 2020). The quality cuts ensure that the objects have adequate LC coverage before and after peak. In addition, they ensure that the reference images used for image subtraction are uncontaminated by transient light, are in fields that are still visible one month after peak, and have low Galactic extinction ($A_V < 1$ mag). The final sample has a total of 36 events, selected from the BTS explorer website. Three events in the sample are subjects of single-object studies already published (SN 2018bvw, SN 2018gep, and SN

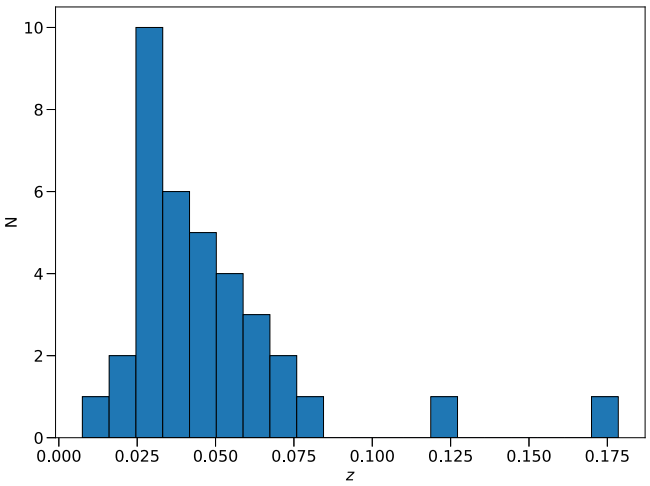

Figure 1. Redshift distribution for the SNe Ic-BL sample.

2020bvc; A. Y. Q. Ho et al. 2019, 2020a, 2020b; L. Izzo et al. 2020; S.-C. Leung et al. 2021; T. A. Pritchard et al. 2021; J. Rho et al. 2021; L. Li et al. 2023), and we refer to those works when necessary. Six events in the sample are also presented in S. Anand et al. (2024), in the context of near-infrared follow-up to search for *r*-process nucleosynthesis, as well as eight events in A. Corsi et al. (2023), in the context of radio follow-up observations searching for relativistic ejecta.

In Figure 1, we show the redshift distribution of events in our sample, which ranges from $z = 0.017$ to $z = 0.1785$. All of the events except for SN 2020wgz and SN 2018hsf have $z < 0.082$, and K-corrections are close to negligible for these events. To quantify this, we generate an SN 1998bw–like LC using `SNCosmo` (K. Barbary et al. 2016), setting the peak absolute magnitude of the SN equivalent to the average value of the sample found in Section 4.2 of -18.51 mag. We find that at peak light, the K-correction at $z = 0.082$ is just $\sim$0.1 mag. SN 2020wgz is a unique event that may be a superluminous SN (SLSN; see Section 7.1). The event has poor spectral coverage, with only three spectra obtained. Because of its unique evolution, utilizing existing templates to compute its K-corrections will not be sufficient, and more complex methods are necessary. SN 2018hsf is another event at high redshift ($z = 0.119$) that also has poor spectral coverage with only three spectra, and though it passed the quality cut there are only a few photometry points pre-peak. This event also is likely not powered by radioactive decay (more in Section 7) and therefore also likely exhibits unique spectral evolution that cannot be modeled with existing templates. Therefore, we do not apply K-corrections to our sample, following S. Anand et al. (2024) and A. Corsi et al. (2023).

In the Appendix, we include descriptions of all the events in this paper that have not been presented in previous works. We provide the first ZTF magnitudes along with the discovery and classification details in each of the descriptions. All magnitudes are reported in the AB system, and UT dates are used throughout this paper. We estimate and use the explosion dates throughout the paper, and measure the phases in rest-frame days with respect to the explosion epochs. We also use a flat ΛCDM cosmology, $H_0 = 69.6\,\mathrm{km\,s^{-1}\,Mpc^{-1}}$, $\Omega_M = 0.286$, and $\Omega_{vac} = 0.714$ (C. L. Bennett et al. 2014), to convert redshifts to distances. In Table 1 we provide the SN IAU name, the ZTF name, R.A. and decl. coordinates to the transient, redshift, distance, and Milky Way extinction (E. F. Schlafly & D. P. Finkbeiner 2011). All average values and errors are calculated through bootstrapping the sample with replacement 10,000 times and drawing from the 16th, 50th, and 84th percentile means derived in the process. We use the Hybrid Analytic Flux FittEr for Transients (HAFFET; S. Yang & J. Sollerman 2023) code for the analyzes presented in Sections 4, 6, and 7. A detailed description of the methodologies used for these analyzes is presented in S. Yang & J. Sollerman (2023), which we summarize in the applicable sections.

3. Observations

We describe here the facilities used to obtain photometric and spectroscopic observations of the SN sample. We note that for two events (SN 2020abxl and SN 2021epp) we did not obtain any spectroscopic observations and utilize publicly available spectra from the ESO Spectroscopic Survey of Transient Objects (ePESSTO+; S. J. Smartt et al. 2015) on the Transient Name Server for classification purposes.

3.1. ZTF

The ZTF camera (R. Dekany et al. 2020) on the Palomar 48 inch telescope was used for supernova discovery and photometric follow-up. ZTF surveys the entire observable northern sky every two to three days in the *r* and *g* bands, in addition to the *i* band for some selected observations, reaching a median 5σ detection depth of 20.5 m_{AB} in the *g* and *r* bands. The default observing mode is 30 s exposures, and alerts according to 5σ changes in brightness relative to the reference image are sent out through an avro format (M. T. Patterson et al. 2019). Real-time filtering through machine learning classifiers (A. Mahabal et al. 2019), star-galaxy classifiers (Y. Tachibana & A. A. Miller 2018), and light-curve properties is also performed for candidate events. ZTF observations of the SN sample last to $\sim$60 days after peak, until the SN is fainter than 20.5 mag. For more information about the data processing and image subtraction pipelines, see F. J. Masci et al. (2019). We utilized both the GROWTH marshal (M. M. Kasliwal et al. 2019) and the Fritz SkyPortal (S. van der Walt et al. 2019; M. W. Coughlin et al. 2023) to gather the data sets needed for this work.

3.2. SEDM

BTS used the Spectral Energy Distribution Machine's (SEDM; N. Blagorodnova et al. 2018; M. Rigault et al. 2019) low-dispersion ($R \sim 100$) integral field spectrograph (IFU) to obtain classification spectra shortly after discovery for many of the objects in our sample. The spectra obtained with the IFU are reduced through a custom data reduction pipeline (M. Rigault et al. 2019) that utilizes flat-fielding, wavelength calibration, extraction, flux calibration, and telluric corrections.

3.3. SPRAT

We used the Spectrograph for the Rapid Acquisition of Transients (SPRAT; A. S. Piascik et al. 2014), a low-resolution ($R \sim 350$) spectrograph mounted on the 2.0 meter Liverpool Telescope (LT; I. A. Steele et al. 2004) on La Palma, Spain, to obtain spectra for some of our events. Spectra are reduced and flux calibrated using a custom pipeline for the LT (R. J. Smith et al. 2016).

Table 1
Discovery Properties of the SNe Ic-BL Sample

ZTF name	SN Name	R.A (hms)	Decl. (° ‘ “)	z	$A_{v,\mathrm{MW}}$ (mag)	First Presented in
ZTF18aaqjovh	SN 2018bvw	11:52:43.62	+25:40:30.1	0.054	0.062	A. Y. Q. Ho et al. (2020a)
ZTF18abhhnnv	SN 2018ell	16:49:57.02	+27:38:26.7	0.0638	0.16	…
ZTF18abukavn	SN 2018gep	15:17:02.54	+03:56:38.7	0.0442	0.124	multiple references[a]
ZTF18acbvpzj	SN 2018hsf	02:40:12.79	−19:58:44.9	0.1184	0.093	…
ZTF18acxgoki	SN 2018keq	23:22:41.97	+21:00:43.2	0.0384	0.341	…
ZTF19aawqcgy	SN 2019hsx	18:12:56.21	+68:21:45.2	0.020652	0.129	S. Anand et al. (2024)
ZTF19aaxfcpq	SN 2019gwc	16:03:26.88	+38:11:02.6	0.038	0.036	S. Anand et al. (2024)
ZTF19abfsxpw	SN 2019lci	16:31:01.61	+08:28:23.7	0.0292	0.208	…
ZTF19ablesob	SN 2019moc	23:55:45.94	+21:57:19.7	0.055	0.171	S. Anand et al. (2024)
ZTF19abqshry	SN 2019oqp	16:38:33.20	+45:37:52.2	0.03082	0.037	…
ZTF19abupned	SN 2019pgo	23:53:00.04	+25:07:16.4	0.0500	0.156	…
ZTF19abzwaen	SN 2019qfi	21:51:07.89	+12:25:38.4	0.028	0.19	S. Anand et al. (2024)
ZTF20aafmdzj	SN 2020zg	04:02:36.39	−16:11:54.4	0.0557	0.087	…
ZTF20aaiqiti	SN 2020ayz	12:12:04.89	+32:44:01.7	0.025	0.038	…
ZTF20aalxlis	SN 2020bvc	14:33:57.00	+40:14:37.3	0.0252	0.031	multiple references[b]
ZTF20aapcbmc	SN 2020dgd	15:45:35.54	+29:18:38.4	0.032	0.071	S. Anand et al. (2024)
ZTF20aaurexl	SN 2020hes	17:47:05.71	+42:46:39.7	0.0700	0.106	…
ZTF20aavcvrm	SN 2020hyj	16:23:47.22	+29:58:58.5	0.055	0.077	…
ZTF20aazkjfv	SN 2020jqm	13:49:18.57	−03:46:10.3	0.03696	0.096	A. Corsi et al. (2023)
ZTF20abbplei	SN 2020lao	17:06:54.60	+30:16:17.3	0.030814	0.138	S. Anand et al. (2024)
ZTF20abrmmah	SN 2020rfr	22:39:49.30	−06:26:16.0	0.0725	0.105	…
ZTF20abswdbg	SN 2020rph	03:15:17.81	+37:00:50.6	0.042	0.65	S. Anand et al. (2024)
ZTF20abzoeiw	SN 2020tkx	18:40:09.00	+34:06:59.5	0.027	0.226	S. Anand et al. (2024)
ZTF20achvlbs	SN 2020wgz	08:57:33.27	+62:34:00.1	0.1785	0.217	…
ZTF20acvcxkz	SN 2020abxl	05:04:22.76	−14:02:46.4	0.0815	0.344	…
ZTF20acvmzfv	SN 2020abxc	01:00:34.04	−08:07:00.7	0.0600	0.255	…
ZTF20adadrhw	SN 2020adow	08:33:42.26	+27:42:43.7	0.0075	0.124	…
ZTF21aagtpro	SN 2021bmf	16:33:29.41	−06:22:49.4	0.017	0.85	S. Anand et al. (2024)
ZTF21aaocrlm	SN 2021epp	08:10:55.27	−06:02:49.3	0.0385	0.15	A. Corsi et al. (2023)
ZTF21aapecxb	SN 2021fop	07:46:42.90	+07:12:38.6	0.077	0.089	…
ZTF21aartgiv	SN 2021hyz	09:27:36.50	+04:27:11.0	0.046	0.125	A. Corsi et al. (2023)
ZTF21aaxxihx	SN 2021ktv	11:03:03.88	+08:51:39.7	0.0700	0.071	…
ZTF21abchjer	SN 2021ncn	22:36:32.92	+25:45:40.5	0.02461	0.143	…
ZTF20abcjdwu	SN 2021qjv	15:10:47.05	+49:12:18.0	0.03803	0.04	…
ZTF21abmjgwf	SN 2021too	21:40:54.28	+10:19:30.4	0.035	0.171	S. Anand et al. (2024)
ZTF21acbnfos	SN 2021ywf	05:14:10.99	+01:52:52.2	0.028249	0.292	S. Anand et al. (2024)

Notes.
[a] A. Y. Q. Ho et al. (2019), S.-C. Leung et al. (2021), T. A. Pritchard et al. (2021).
[b] A. Y. Q. Ho et al. (2020b), L. Izzo et al. (2020), J. Rho et al. (2021), L. Li et al. (2023).

3.4. LRIS

We used the Low Resolution Imaging Spectrometer (LRIS; J. B. Oke et al. 1995) on the 10 m Keck I telescope to obtain spectra for some of the events in our sample. We utilized typical exposure times of 600 s, long-slit masks of 1.″0 or 1.″5 width, and the 400/3400 grism on the blue arm and the 400/8500 grating on the red arm, with a central wavelength of 7830 Å. This enabled wavelength coverage from 3200 to 10000 Å. The reduction was done using LPipe (D. A. Perley 2019).

3.5. DBSP

We used the Double Beam Spectrograph (DBSP; J. B. Oke & J. E. Gunn 1982) on the Palomar 200 inch telescope to obtain low- to medium-resolution ($R \sim 1000$–$10{,}000$) spectra of many of the events in our sample. DBSP has a pixel scale of 0.″293 pixel^{-1} (red side) and 0.″389″ pixel^{-1} (blue side). We utilized a red grating of 316/7500, a blue grating of 600/400, a D55 dichroic, and slit masks of 1″, 1.″5, and 2″. The data reduction was done using a custom PyRAF DBSP reduction pipeline (E. C. Bellm & B. Sesar 2016), while the rest were reduced using a custom DBSP Data Reduction pipeline relying on Pypeit (J. X. Prochaska et al. 2019; M. S. Roberson et al. 2021).

3.6. ALFOSC

We used the Alhambra Faint Object Spectrograph and Camera (ALFOSC) on the 2.56 m Nordic Optical Telescope (NOT) at the Observatorio del Roque de los Muchachos on La Palma (Spain) to obtain low-resolution ($R \sim 700$) spectra for some events in our sample.[28] The spectra were obtained with a 1.″0 wide slit and grism #4 with a spectral resolution of 360. We reduced the data with IRAF and Pypeit.

3.7. Swift XRT and UVOT

The Neils Gehrels Swift observatory (N. Gehrels et al. 2004) observed a handful of events in our sample. A. Corsi et al.

[28] http://www.not.iac.es/instruments/alfosc

(2023) report the observations taken with the X-ray telescope (XRT; D. N. Burrows et al. 2005), with five non-detections (SN 2020lao, SN 2020tkx, SN 2020jqm, SN 2020rph, and SN 2021hyz) and two detected events (SN 2019hsx and SN 2019ywf). In addition, A. Y. Q. Ho et al. (2019, 2020a, 2020b) report Swift non-detections for two more events in the sample (SN 2018bvw and SN 2018gep) and one more detected event (SN 2020bvc). SN 2020adow was also detected by the XRT, but was not included in A. Corsi et al. (2023). We utilize the X-ray detections for the subset of events in our sample in Section 8. In this work, we also utilize observations taken with Swift's Ultra-Violet/Optical Telescope (UVOT; P. W. A. Roming et al. 2005) to better constrain the blackbody temperature and radii of the events in our sample. UVOT observed SN 2018etk, SN 2018hom, SN 2019hsx, SN 2020jqm, SN 2020lao, SN 2020rph, SN 2020tkx, and SN 2021ywf, across the *v*, *b*, *u*, uvw1, uvm2, and uvw2 filters. In addition to these observations, we also obtained target of opportunity observations in 2022 in the same filters as the SN initial measurements, to obtain late-time photometry of the host galaxies of these SNe. We did this in order to correct for any host-galaxy contamination in the SN photometry. We used the `uvotsource` task to measure the photometry, and utilize the photometry in Section 6.2 to better constrain the blackbody temperature and radii for part of the sample. We note that SN 2020adow also had measurements from UVOT; however, this event was added to our sample in 2024, and due to Swift's pointing constraints this event will not be visible again until late 2024. Therefore, we omit the Swift data.

3.8. Very Large Array

3.8.1. Individual Observations

A. Corsi et al. (2023) observed eight events in our sample using the Very Large Array (VLA). Five events in the sample (SN 2020lao, SN 2021hyz, SN 2020rph, SN 2021epp, and SN 2019hsx) had radio non-detections or detections that were consistent with emission from the host galaxy. Three events (SN 2020jqm, SN 2020tkx, and SN 2021ywf) have radio detections compatible with point sources along with variability over the timescale of observations. SN 2020adow was also observed by the VLA (A. Corsi et al. 2021) and has multiple radio point-source detections that evolve with time. In addition, A. Y. Q. Ho et al. (2019, 2020a, 2020b) and L. Izzo et al. (2020) report radio point-source detections for three more events in our sample (SN 2018gep, SN 2018bvw, and SN 2020bvc). SN 2018bvw and SN 2020bvc were clear transient radio sources.

At the time of publication in A. Y. Q. Ho et al. (2019), SN 2018gep's radio detections could not be ruled out from being due to its host galaxy. A. Y. Q. Ho et al. (2019) reports three detections in the VLA D configuration (of 34, 24.4, and 26.8 μJy at 9, 9.7, and 14 GHz) and two non-detections in the VLA C configuration two months after the last detection (of <16 and <17 μJy at 9 and 14 GHz), which is a comparable level to the declining trend in flux. Because the C configuration has a different resolution than the D configuration, it was unclear whether the detections in the D configuration were from the host galaxy and were simply being resolved out in the C configuration observations. Therefore, in 2021 April, more than two years after the initial observations, SN 2018gep's location was observed by VLA program ID 21A-308 (PI Ho) in the D configuration, with the same setup as the initial observations. The source was not detected, to an upper limit of <18 μJy, confirming the transient SN 2018gep displays fading radio emission with time. We therefore conclude that the radio detections of SN 2018gep reported in A. Y. Q. Ho et al. (2019) are from the transient.

3.8.2. VLASS

The Karl G. Jansky Very Large Array Sky Survey (VLASS) is conducted across multiple epochs in the *S*-Band at 2–4 GHZ to monitor and analyze the radio sky. The VLASS is divided into three distinct epochs, each with its own timeline:

1. Epoch 1. Commenced on 2017 September 13 and concluded on 2019 July 22.
2. Epoch 2. Started on 2020 May 27 and ended on 2022 March 7.
3. Epoch 3. Began on 2023 February 1, with observations planned to continue until the end of 2024.

The typical rms noise for an individual epoch detection in the VLASS is around 0.12 mJy, which provided a baseline for assessing the sensitivity of the survey and the significance of detections.

Using a cross-matching effort between the BTS and the VLASS, we searched for radio emission for the 36 SNe Ic-BL in our sample, and found that SN 2021bmf was the only object that showed transient radio emission across the three epochs. The first VLASS epoch had a nondetection on 2019 June 17, 19 months before the SNe. The second epoch had a detection on 2021 September 26, eight months after the SN's peak with a peak flux of 5.57 ± 0.526 mJy. This corresponds to a peak luminosity of 4.2×10^{28} erg s^{-1} Hz^{-1}.

Therefore, we consider eight events to have radio counterparts (SN 2018gep, SN 2018bvw, SN2020bvc, SN 2020jqm, SN 2020tkx, SN 2020adow, SN 2021bmf, and SN 2021ywf), and five events to have radio nondetections (SN 2019hsx, SN 2020lao, SN 2020rph, SN 2021epp, and SN 2021hyz).

4. Supernova Light Curves

4.1. Light-curve Interpolation

Before creating LCs for the events, we correct ZTF photometry for Galactic extinction with the Milky Way color excess $E(B-V)_{\rm MW}$ toward the position of every SN from E. F. Schlafly & D. P. Finkbeiner (2011). We use the J. A. Cardelli et al. (1989) extinction law to perform reddening corrections, setting $R_V = 3.1$. To be consistent with S. Anand et al. (2024) and A. Corsi et al. (2023), we also assume zero host-galaxy extinction (more in Section 5.2).

We use ZTF forced photometry to construct optical LCs for each event in the sample and show the LCs in Figure 2, along with the $g-r$ colors. The ZTF forced photometry is unevenly sampled, making it difficult to derive LC parameters. Therefore, we use a nonparametric data-driven interpolation technique, Gaussian Processing (GP), to interpolate the LCs. We focus on the *g*- and *r*-band fluxes and use the `GEORGE` (S. Ambikasaran et al. 2015) package with a stationary Matern 3/2 kernel and a flat mean function for the flux form. When the data either have large uncertainties or become more sparse, we fit the interpolated data with the analytic function from

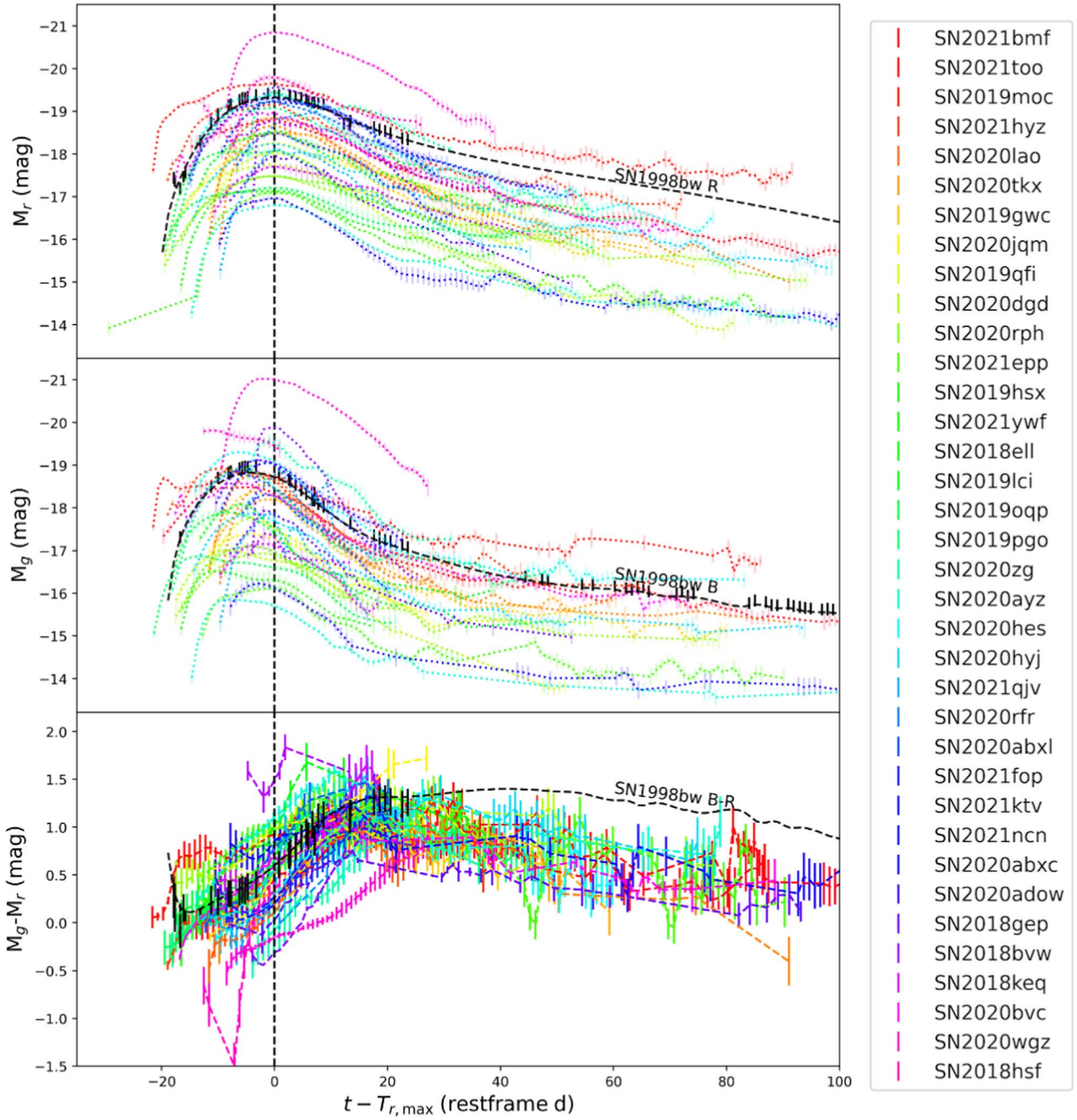

Figure 2. Light-curve and color comparison bewteen the SNe Ic-BL sample and SN 1998bw in r/R- and g/B-bands, with all magnitudes corrected for Galactic extinction, and the GP-processed LCs shown. The colors are computed with a combination of the data binned within 1 day, as well as the GP-processed LCs. The LC of SN 1998bw (A. Clocchiatti et al. 2011) was interpolated through GP techniques, and is shown as the black dashed lines.

G. Bazin et al. (2009), where the flux is represented as

$$F(t) = A\frac{e^{-(t-t_{0,\mathrm{Bazin}})/\tau_{\mathrm{fall,Bazin}}}}{1+e^{-(t-t_{0,\mathrm{Bazin}})/\tau_{\mathrm{rise,Bazin}}}} + B \quad (1)$$

where $\tau_{\mathrm{rise,Bazin}}$ and $\tau_{\mathrm{fall,Bazin}}$ represent the rising (which we note differs from τ_{rise} reported in Section 4.3, corresponding to the rise time of the SN from the explosion epoch to peak light), and declining time, A is a normalization parameter, $t_{0,\mathrm{Bazin}}$ is a characteristic timescale (which we note differs from t_0 reported in Section 4.2), and B is the baseline flux. After running a Monte Carlo simulation on the rest-frame LCs with priors and boundaries listed in Table 2, we find the best-fitting Bazin function for each of our events and use it in addition to the ZTF forced photometry and GP-interpolated data to help derive LC parameters. An example of this fitting procedure is shown in

Table 2
Priors Used for the Bazin Fits

Parameter	Prior	Boundary
$\tau_{\mathrm{rise,Bazin}}$	10	[0, 60] days
$\tau_{\mathrm{fall,Bazin}}$	−15	[0, 120] days
t_0	0	[−10, 10] days
A	$F_{\max}$	[$F_{\max}$*0.5, $F_{\max}$*2]
B	5	[−20, 20]

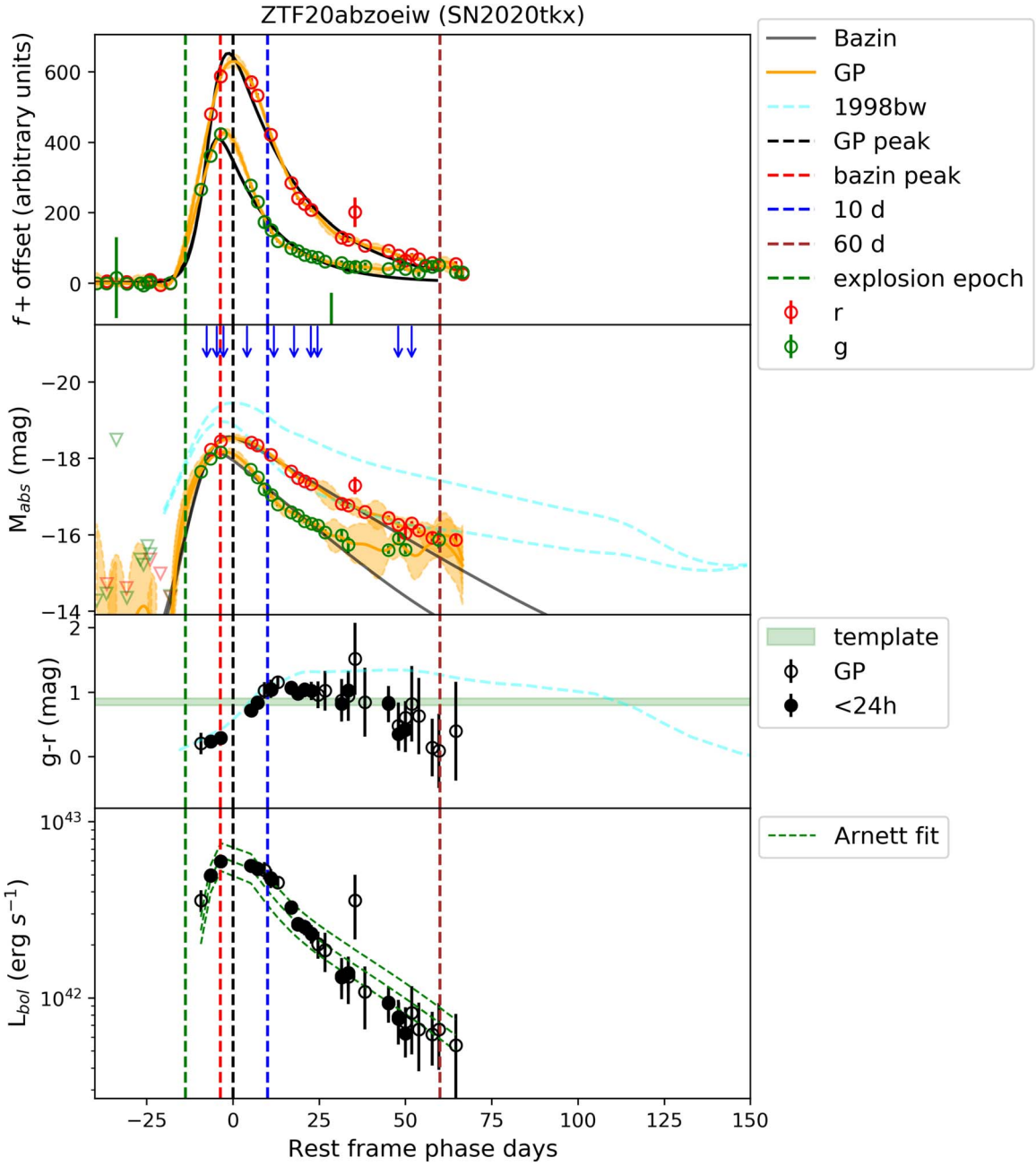

Figure 3. Example of LC fits for SN 2020tkx. Top panel: the photometry in flux space together with the GP interpolation and fit to the Bazin formula. This allows for estimates of peak time and other LC parameters, provided in Table 3. Peak magnitudes are shown in *r* band, along with the derived explosion epoch. Second panel: the absolute magnitude LC, along with the GP inteprolation and best-fit Bazin function. SN 1998bw's LCs are plotted as comparison. The blue arrows indicate epochs when spectra were taken. Third panel: the color evolution, along with that of SN 1998bw. The template shown is a range of colors for normal stripped-envelope SNe from J. Sollerman et al. (2022). Bottom panel: the bolometric luminosity LC, along with the best-fit W. D. Arnett (1982) model.

Figure 3. This same LC interpolation process was done for the events also presented in A. Corsi et al. (2023) and S. Anand et al. (2024) and for those events we redo the fits and find that they are consistent. For parameters that were already derived in their works, we quote their results.

4.2. Light-curve Empirical Parameters

After interpolating the LCs, we derive empirical LC parameters for every event and show the results in Table 3. For events shared with A. Corsi et al. (2023) and S. Anand et al. (2024), we report the peak absolute magnitudes in *r* band (M_r^{max}), the explosion epochs ($t_{exp,r}$), and the peak time in *r* band (t_0) derived in their works.

We begin by determining M_r^{max} and t_0 for new events using the GP-processed LCs. We show a histogram of the peak *r*-band absolute magnitude distributions of our sample in Figure 4. The distribution ranges over 4 mag from −16.86 to −20.89 mag. SN 2020wgz is a clear outlier with respect to the rest of the sample, with $M_r^{max} = -20.89 \pm 0.11$ mag, placing it in the luminosity regime of SLSNe. We discuss this event's properties at length in Section 7.1. The average peak magnitude is $\overline{M}_r^{max} = -18.51 \pm 0.15$ mag, with an associated 1σ standard deviation of 0.90 mag (shown in the Figure as dashed

Table 3
Empirical Parameters, Explosion Epochs, and Peak r-band Times for the SNe Ic-BL Sample

ZTF name	SN Name	$(g-r)_{10}$ (mag)	Δm_{15} (mag)	Δm_{-10} (mag)	$M_{\rm r,peak}$ (mag)	$t_{{\rm exp},r}$ (days)	t_0 (JD)
ZTF18aaqjovh	SN 2018bvw	⋯	0.63 (0.05)	1.42 (0.04)	−18.85 (0.10)	$-8.09^{+2.04}_{-2.04}$	2,458,248.80
ZTF18abhhnnv	SN 2018ell	1.13 (0.49)	0.87 (0.09)	0.65 (0.12)	−18.55 (0.12)	$-16.15^{+0.8}_{-0.84}$	2,458,330.71
ZTF18abukavn	SN 2018gep	0.51 (0.03)	1.15 (0.02)	⋯	−19.56 (0.09)	$-4.09^{+0.01}_{-0.01}$	2,458,374.74
ZTF18acbvpzj	SN 2018hsf	⋯	⋯	0.59 (0.36)	−19.85 (0.16)	$-12.43^{+2.43}_{2.43}$	2,458,432.83
ZTF18acxgoki	SN 2018keq	1.26 (0.22)	0.33 (0.11)	0.78 (0.17)	−17.62 (0.13)	$-14.07^{+4.1}_{-4.1}$	2,458,475.68
ZTF19aawqcgy	SN 2019hsx	1.32 (0.47)	0.88 (0.09)	0.65 (0.11)	−17.08 (0.02)	$-15.63^{+0.38}_{-0.53}$	2,458,647.57
ZTF19aaxfcpq	SN 2019gwc	0.90 (0.14)	0.88 (0.06)	1.14 (0.06)	−18.48 (0.01)	$-12.78^{+0.46}_{-0.46}$	2,458,651.08
ZTF19abfsxpw	SN 2019lci	0.87 (0.39)	⋯	0.07 (0.03)	−18.07 (0.10)	$-18.1^{+0.47}_{-0.2}$	2,458,693.71
ZTF19ablesob	SN 2019moc	1.00 (0.11)	0.77 (0.13)	0.21 (0.14)	−19.16 (0.03)	$-20.02^{+0.27}_{-3.23}$	2,4587,16.26
ZTF19abqshry	SN 2019oqp	0.89 (0.16)	0.69 (0.19)	0.21 (0.07)	−17.27 (0.11)	$-22.45^{+0.41}_{-0.41}$	2,458,737.71
ZTF19abupned	SN 2019pgo	1.39 (0.1)	0.85 (0.04)	0.43 (0.04)	−19.06 (0.10)	$-15.85^{+0.38}_{-0.66}$	2,458,743.91
ZTF19abzwaen	SN 2019qfi	1.03 (0.53)	0.92 (0.16)	0.76 (0.39)	−18.01 (0.02)	$-15.09^{+1.4}_{-1.4}$	2,458,754.06
ZTF20aafmdzj	SN 2020zg	0.37 (0.08)	0.37 (0.22)	⋯	−19.45 (0.21)	$-5.06^{+0.95}_{-0.95}$	2,458,867.74
ZTF20aaiqiti	SN 2020ayz	1.75 (0.13)	0.81 (0.03)	0.52 (0.06)	−16.86 (0.10)	$-14.33^{+0.32}_{-0.51}$	2,458,887.97
ZTF20aalxlis	SN 2020bvc	1.00 (0.02)	0.84 (0.03)	0.48 (0.02)	−19.02 (0.09)	$-18.11^{+0.89}_{-0.89}$	2,458,901.06
ZTF20aapcbmc	SN 2020dgd	1.10 (0.8)	0.75 (0.37)	0.28 (0.14)	−17.74 (0.02)	$-18.03^{+2.5}_{-2.5}$	2,458,914.55
ZTF20aaurexl	SN 2020hes	0.77 (0.13)	1.02 (0.09)	0.41 (0.03)	−19.39 (0.10)	$-16.03^{+4.97}_{-4.97}$	2,458,964.99
ZTF20aavcvrm	SN 2020hyj	0.92 (0.11)	0.66 (0.02)	0.66 (0.06)	−18.23 (0.13)	$-15.01^{+0.98}_{-0.98}$	2,458,969.94
ZTF20aazkjfv	SN 2020jqm	1.13 (0.5)	0.56 (0.08)	0.55 (0.08)	−18.26 (0.02)	-17^{+1}_{-1}	2,458,996.71
ZTF20abbplei	SN 2020lao	0.92 (0.07)	0.83 (0.08)	2.88 (0.1)	−18.66 (0.02)	$-10.6^{+0.99}_{-0.99}$	2,459,004.42
ZTF20abrmmah	SN 2020rfr	1.40 (0.26)	0.05 (0.11)	2.21 (0.14)	−18.90 (0.10)	$-6.99^{+1.96}_{-1.96}$	2,459,078.86
ZTF20abswdbg	SN 2020rph	0.96 (0.27)	0.48 (0.08)	0.49 (0.06)	−17.48 (0.02)	$-19.88^{+0.02}_{-0.02}$	2,459,092.84
ZTF20abzoeiw	SN 2020tkx	1.01 (0.15)	0.72 (0.13)	0.79 (0.22)	−18.49 (0.05)	$-12.77^{+4.54}_{-4.54}$	2,459,117.00
ZTF20achvlbs	SN 2020wgz	0.06 (0.05)	0.64 (0.04)	2.53 (0.09)	−20.89 (0.11)	$-10.04^{+0.15}_{-0.15}$	2,459,140.01
ZTF20acvcxkz	SN 2020abxl	1.45 (0.31)	0.8 (0.05)	0.45 (0.03)	−19.24 (0.15)	$-13.25^{+0.01}_{-0.01}$	2,459,200.97
ZTF20acvmzfv	SN 2020abxc	0.90 (0.14)	0.56 (0.05)	0.69 (0.05)	−19.30 (0.10)	$-12.95^{+0.47}_{-0.88}$	2,459,203.73
ZTF20adadrhw	SN 2020adow	0.59 (0.01)	0.99 (0.01)	1.9 (0.01)	−17.97 (0.09)	$-10.59^{+2.4}_{-2.4}$	2,459,218.95
ZTF21aagtpro	SN 2021bmf	0.72 (0.13)	1.14 (0.17)	0.13 (0.06)	−18.77 (0.14)	$-23.76^{+5.68}_{-5.52}$	2,459,265.62
ZTF21aaocrlm	SN 2021epp	1.30 (0.23)	0.32 (0.04)	0.4 (0.06)	−17.49 (0.03)	$-15.12^{+1.48}_{-1.48}$	2,459,292.33
ZTF21aapecxb	SN 2021fop	0.74 (0.15)	0.68 (0.08)	2.08 (0.36)	−18.49 (0.10)	$-7.05^{+5.01}_{-5.01}$	2,4592,92.75
ZTF21aartgiv	SN 2021hyz	0.84 (0.19)	1.04 (0.19)	1.52 (0.08)	−18.83 (0.05)	$-12.88^{+0.94}_{-0.94}$	2,459,319.81
ZTF21aaxxihx	SN 2021ktv	1.15 (0.29)	0.53 (0.09)	0.92 (0.07)	−19.22 (0.10)	$-12.04^{+2.94}_{-2.94}$	2,459,344.79
ZTF21abchjer	SN 2021ncn	1.01 (0.13)	1.1 (0.10)	1.19 (0.15)	−17.05 (0.10)	$-10.02^{+0.01}_{-0.01}$	2,459,364.97
ZTF20abcjdwu	SN 2021qjv	1.31 (0.08)	0.87 (0.10)	2.83 (0.20)	−18.12 (0.10)	$-10.01^{+0.02}_{-0.02}$	2,459,389.83
ZTF21abmjgwf	SN 2021too	1.20 (0.18)	0.59 (0.15)	0.22 (0.08)	−19.66 (0.02)	$-23.23^{+0.41}_{-0.41}$	2,459,434.59
ZTF21acbnfos	SN 2021ywf	1.1 (0.6)	0.68 (0.42)	0.44 (0.25)	−17.10 (0.05)	$-17.47^{+0.49}_{-0.49}$	2,459,485.95

Note. We draw from results in previous works where applicable (described in Section 4.2).

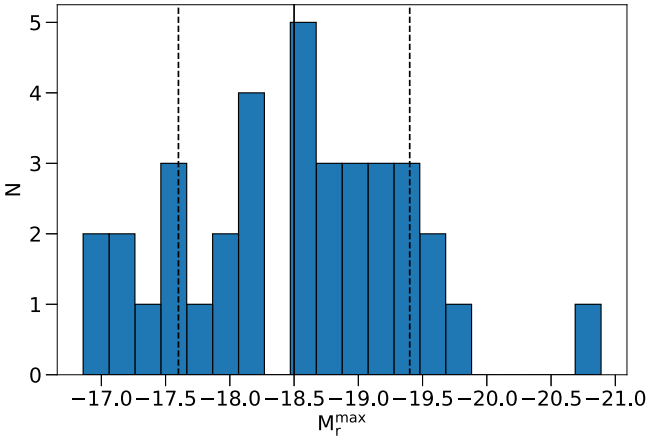

Figure 4. $M_{\rm r}^{\rm max}$ distribution of the SNe Type Ic-BL sample, with the mean magnitude (−18.51 mag) shown with a solid line and the standard deviation (0.90 mag) range shown with dashed lines.

lines). The average absolute magnitude derived is consistent with that found in the iPTF sample of F. Taddia et al. (2019) for events without an associated GRB ($\overline{M}_{\rm r}^{\rm max} = -18.6$ mag, with a 1σ standard deviation of 0.5 mag). When excluding SN 2020wgz from the sample, we find a mean peak magnitude of $\overline{M}_{\rm r}^{\rm max} = -18.44 \pm 0.14$ mag, and a 1σ standard deviation of 0.82 mag. The uncertainty that we report is derived from the uncertainty in photometric observations, and these magnitudes are all corrected for Milky Way extinction.

We then derive the $g-r$ colors for each of the events in the sample 10 days after peak, $(g-r)_{10}$, to compare the color evolution of the sample. We find an average value of $\overline{(g-r)}_{10} = 1.00 \pm 0.06$ mag, with a 1σ standard deviation of 0.43 mag. All of the events in the sample except for SN 2020ayz, SN 2018gep, SN 2020wgz, and SN 2020zg have $(g-r)_{10}$ values consistent within the average and 1σ standard deviation, showing that the sample has broadly consistent color evolution.

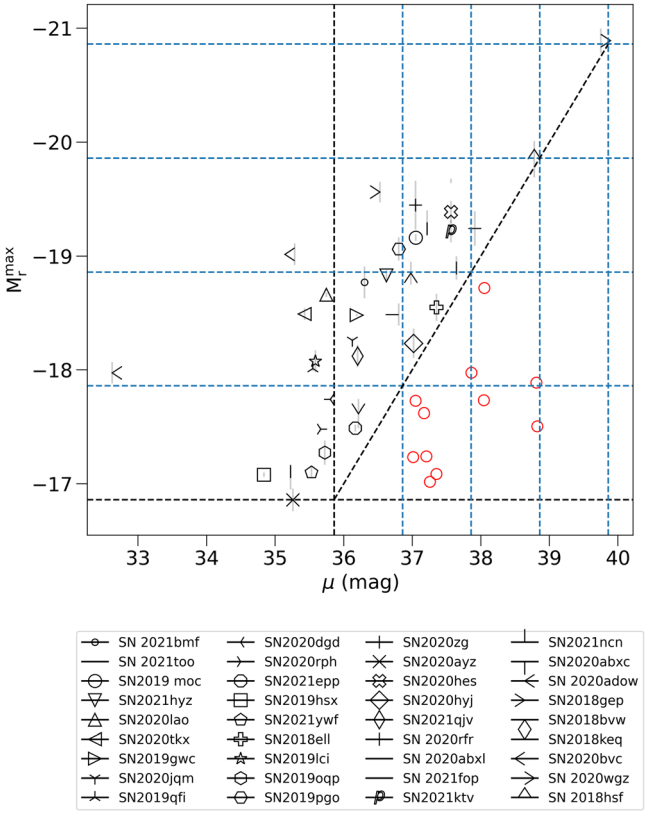

Figure 5. Investigation of the Malmquist bias on the sample. M_r^{max} and the distance modulus (μ) for the events are plotted, with the minimum absolute magnitude (−16.86 mag) of the sample shown as a black dashed horizontal line. The distance modulus where the sample is complete ($\mu = 35.86$ mag) is shown as a black dashed vertical line. One magnitude by one magnitude bins are marked by dashed blue lines, where the cutoff distance for the sample is marked by a black dashed vertical line. The random simulated events created through the method described in D. Richardson et al. (2014) are shown as red circles. The overall effect of the Malmquist bias is a 0.2 mag decrease in the overall average M_r^{max} of the sample.

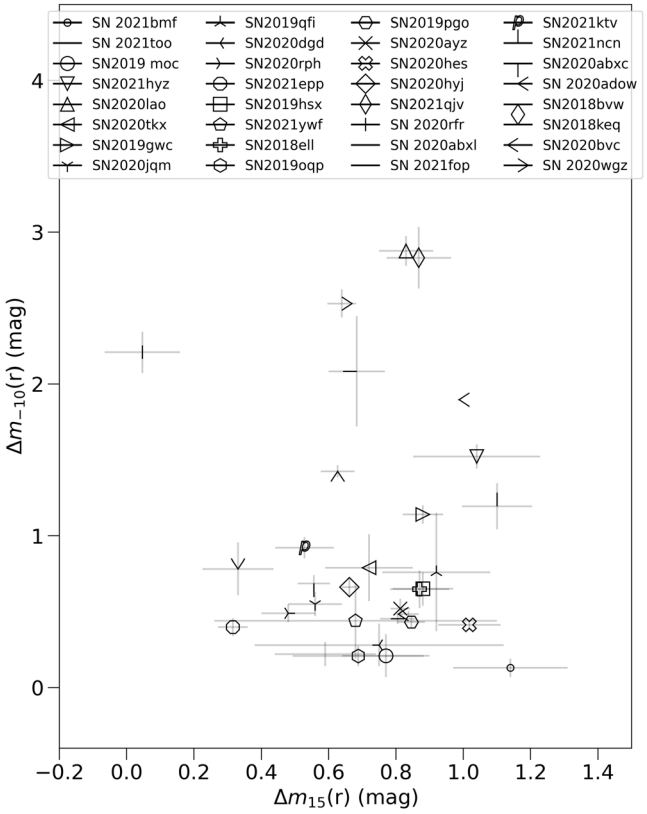

Figure 6. Parameter $\Delta m_{-10}(r)$ plotted against $\Delta m_{15}(r)$ for 32 events in the sample. We found no correlations between the two parameters, with a p-value of 0.98.

We then investigate the effects of the Malmquist bias on the peak r-band absolute magnitudes of the sample. The Malmquist bias arises because more luminous objects can be detected out to greater distances than less luminous objects. Because our sample is magnitude limited, it is likely that ZTF failed to detect fainter SNe that occurred at greater distances, and we quantify this effect below.

We plot the peak magnitude and distance modulus (μ) for each event in the sample in Figure 5. The faintest peak absolute r-band magnitude of the sample is −16.86. The BTS survey detects objects with an apparent magnitude as faint as ∼19 mag, so we use this value as the upper limit for SN detectability for the BTS survey. The minimum peak absolute r-band magnitude and upper limit for SN detectability sets $\mu = 35.86$ as the distance modulus for which we observe the complete peak magnitude distribution. We then utilize the method described in D. Richardson et al. (2014) to simulate the magnitude of missing SNe randomly in one magnitude bins, cutting off the sample at the furthest event. The results of the simulation are shown in Figure 5. We calculate a new average r-band peak absolute magnitude of −18.3 mag, with a 1σ dispersion of 0.91 mag. Therefore, the Malmquist bias produces a difference of ∼0.2 mag in the average peak magnitude distribution for the sample. This is the same difference found in F. Taddia et al. (2019) for their sample. We note that this difference is just an estimate, and more complicated effects (e.g., the distribution of events with respect to their position in the Milky Way plane, the assumption that there are no events fainter than the faintest in our sample for the whole population) were not accounted for.

We also derive the decline parameter $\Delta m_{15}(r)$ and rise parameter $\Delta m_{-10}(r)$, which are the difference in magnitudes in the r band from the peak to 15 days after the peak, and from 10 days before the peak to the peak, respectively, for every event in the sample. In Figure 6, we show $\Delta m_{-10}(r)$ plotted against $\Delta m_{15}(r)$ for our sample, with the exception of SN 2018hsf, SN 2019lci, SN 2020zg, and SN 2018gep, (the first three events lacked sufficient photometry at the times necessary to calculate these parameters, while SN 2018gep had a rise time from the explosion epoch to peak quicker than 10 days). Through a Spearman rank coefficient test, we do not find any correlation between the two parameters, with a p-value of 0.98. This contrasts with the results found in F. Taddia et al. (2019), who found that fast-rising objects also are fast decliners, with a p-value of 0.06. However, they only tested the correlation for 12 of the best-sampled events in their sample, while we test the correlation using 32 events, utilizing the GP interpolations and Bazin fits. Therefore, we show that, when removing observational biases with respect to the best-sampled LCs, fast-rising SNe Ic-BL are not necessarily also fast decliners.

We then test for the presence of a Phillips relation (M. M. Phillips 1993) between M_r^{max} and $\Delta m_{15}(r)$. A relation between the decline rate and luminosity was established for SNe Ia through this relation (C. R. Burns et al. 2011) and was also found for GRB-SNe (Z. Cano 2014; X. Li & J. Hjorth 2014). We show these two parameters plotted against

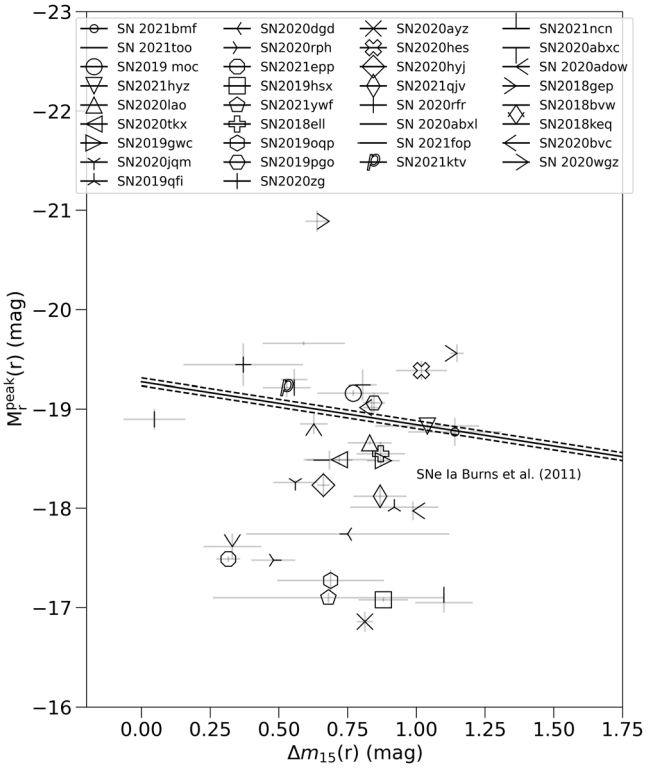

Figure 7. M_r^{max} plotted against $\Delta m_{15}(r)$ for 34 events in the sample. There is no evidence for a Phillips relation, which is shown for SNe Ia as the black line with the dashed lines representing the errors from C. R. Burns et al. (2011).

each other for 34 events in our sample (with the exception of SN 2018hsf and SN 2019lci), as well as the Phillips relation for SNe Ia from C. R. Burns et al. (2011) in Figure 7. We do not find this relation present in our sample, consistent with the findings from F. Taddia et al. (2019). Therefore, less luminous SNe do not necessarily decline faster than more luminous events.

4.3. Explosion Epochs

When sufficient early time photometry is available, we determine the explosion epoch ($t_{exp,r}$) and rise time (τ_{rise}) of every newly presented SN through Monte Carlo approaches, after characterizing the early emission of the transients in g and r bands through a power law following the methodology of A. A. Miller et al. (2020).[29] The power law is fit from the estimated baseline up to 40% of the maximum flux determined by the Bazin fit. For those SNe that do not have sufficient early time photometry, we take the average of the first detection and the last non-detection in ZTF forced photometry as the explosion epoch and determine the error through the half-width. SN 2018hsf did not have a ZTF nondetection prior to the first detection, due to the instrument not operating for some time period before. For this case, we use the last ATLAS nondetection in o band to calculate the explosion epoch. We calculate the rise time τ_{rise} obtained for our sample, measured from the derived explosion epoch to the peak epoch in r band, along with the average value and 1σ standard deviation. We find $\overline{\tau}_{rise} = 14.0 \pm 0.8$ days, with a 1σ standard deviation of 5.81 days. This is consistent with the value obtained in F. Taddia et al. (2019), who found $\overline{\tau}_{rise} = 15$ days with a 1σ standard deviation of 6 days.

[29] https://github.com/adamamiller/ztf_early_Ia_2018.

5. Supernova Spectra

We present the photospheric phase spectra for each of the new events in our sample in Figure 8, not presented in previous works. In Section 3, we detail the instruments used to obtain spectra of the events in our sample. All of the spectra were reduced in a standard manner, with wavelength and flux calibrations. All spectra will be made publicly available on WISeREP (O. Yaron & A. Gal-Yam 2012).

As shown in Figure 8, none of the spectra display hydrogen and helium features, while they all share characteristic broad absorption features. Their broad features are the result of the blending of multiple absorption lines due to Doppler broadening effects, and the Fe II and Si II absorption lines are indicated in the Figure.

5.1. Photospheric Velocities

In addition to the broadened features, the centers of the absorption troughs are blueshifted relative to the rest-frame Fe II and Si II absorption line wavelengths, due to the high velocity of the ejecta toward the observer. M. Modjaz et al. (2016) showed that the blueshifted absorption velocity of the Fe II line at 5169 Å is a good proxy for the photospheric expansion velocity (v_{ph}), and we calculate these velocities for each of the events in our sample. We use a similar method to S. Anand et al. (2024), beginning by using `WOMBAT` to remove host-galaxy emission lines and telluric features, and use `SESNSpectraPCA` (M. Williamson et al. 2019) to smooth the spectra. Finally, we utilize `SESNSpectraLib` (Y.-Q. Liu et al. 2016; M. Modjaz et al. 2016) to fit for the Fe II absorption velocity by convolving a blueshifted Gaussian with a Type Ic SN template and measuring the blueshift of the Fe II feature with respect to these templates. An example of this fititng procedure is shown in Figure 9.

In order to derive v_{ph} at the peak of the SNe LCs, we use the highest quality spectrum available closest to the peak of the SNe to measure the velocities. For some events, this is different than the spectrum used for classification purposes. The full set of spectra for each SN in our sample is shown in the Appendix. Through this method, we were able to obtain either an estimate or constraint of the peak v_{ph} for 26 out of the 36 events in our sample (10 events had spectra that lacked sufficent signal-to-noise ratios to obtain an accurate velocity measurement). For six of the events, we could only obtain velocity measurements more than 15 days post peak light, and therefore their velocities are not representative of the peak velocity. All the velocities are reported in Table 5, where we report the velocities derived for new events, along with those already presented in literature. In Figure 10, we show a histogram of the distribution of the peak v_{ph}, without the events with spectra taken greater than 15 days from peak. We find an average value of $16{,}100 \pm 1100$ km s^{-1}, with a 1σ standard deviation of 5600 km s^{-1}. In Figure 11, we show the evolution of v_{ph} over time for the sample, compared to other GRB-SNe, X-ray flash (XRF)-SNe, a "normal" Type Ic SN, the iPTF sample of F. Taddia et al. (2019), and the samples from S. Anand et al. (2024) and A. Corsi et al. (2023). We see that our sample's evolution is broadly consistent with that of the iPTF sample and the other single-object events shown, with the exception of the "normal" Type Ic SN 1994I.

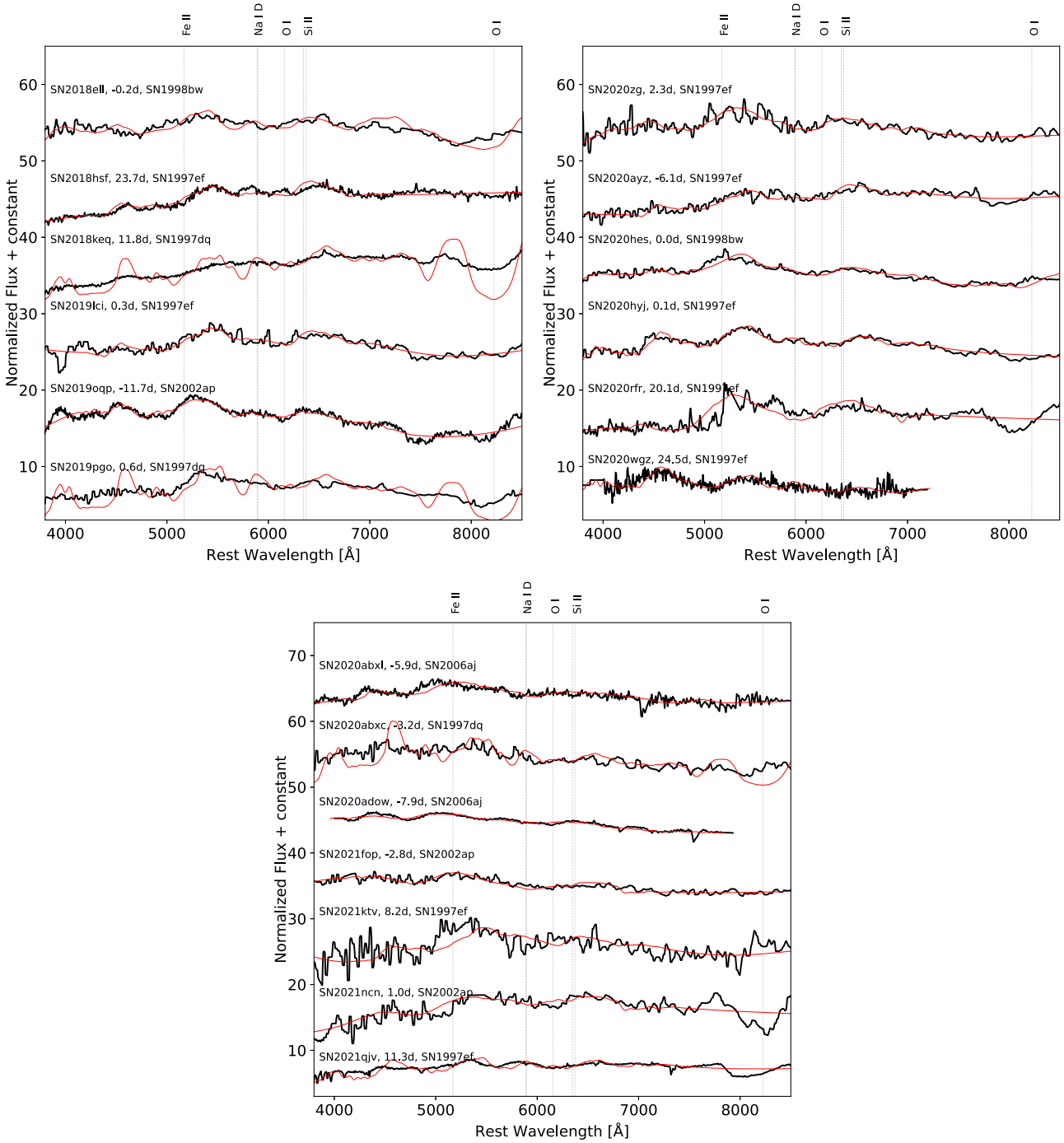

Figure 8. Photospheric phase spectra (black) and the SNID best-match templates (red) for the Ic-BL sample that has not been presented in previous works. The text shows the name of the transient, the observer-frame spectroscopic phase since *r*-band maximum, and the name of the transient template used for the fitting.

5.2. Na I Equivalent Width

Out of the 36 events in the sample, 20 had spectra from either DBSP or LRIS, which are the highest resolution spectra in the sample (though still low resolution in general). We measure the equivalent width (EW) of the Na I absorption feature for every event in the sample, as this feature has been shown to be a proxy for the amount of host-galaxy extinction present (M. D. Stritzinger et al. 2018). Fourteen events, including the majority of events in A. Corsi et al. (2023) and S. Anand et al. (2024) had Na I EWs consistent with 0 within error bars. There are five new events not previously analyzed in literature that have EWs greater than 0: SN 2018hsf, SN 2018keq, SN 2019lci, SN 2020ayz, and SN 2020bvc. One event from S. Anand et al. (2024), SN 2019hsx, showed a significant Na I feature, which is at odds with their conclusion that no events in the sample demonstrated the feature. The EWs are shown in Table 4.

It is possible to convert the EWs to host-galaxy extinctions through the relation from M. D. Stritzinger et al. (2018): $A_V^{\rm host}$[mag] $= 0.78(\pm0.15) \times {\rm EW}_{\rm Na\,I}$. However, this relation only holds strongly when using high-resolution spectra for these measurements; when using low-resolution spectra, D. Poznanski et al. (2011) showed that even though a weak

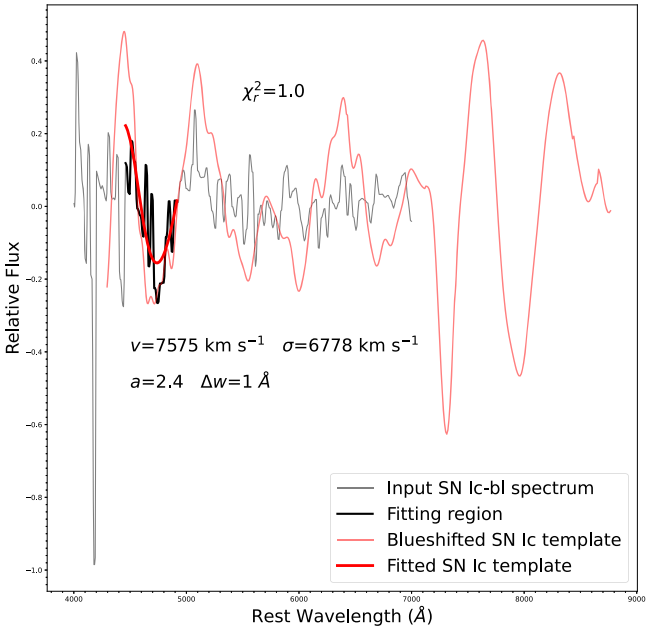

Figure 9. Example of the convolution fitting of the Fe II feature for the photospheric phase spectra of SN 2018hsf. The spectrum of the transient is shown in gray, with the fitting region bolded in black. The blueshifted Ic template is shown in red, with the fitting region bolded in red. The reduced chi-square value for the fit is shown (χ^2_r), along with the blueshifted velocity with respect to the Ic template (v), the Doppler broadened line width velocity (σ), the amplitude (a), and the wavelength range (δw).

correlation exists the large scatter makes any relation between the two quantities useless. Therefore, it is possible that these six events have additional host-galaxy extinction; however, due to the lack of high-resolution spectra, we cannot quantify the amount or say with certainty that a significant amount of extinction is present. Therefore, we compute a conservative upper limit on the amount of host-galaxy extinction for these events, and show the results in Table 4. However, given the lack of constraints, we do not correct for host-galaxy extinction for any of these events during our analysis.

6. Bolometric LCs and Properties

6.1. Bolometric Light Curves and Peak Luminosites

There is a lack of complete multiband coverage for the majority of events in our sample—in particular the coverage in the i band is sparse. Therefore, due to the sufficient coverage in g and r bands, we use the $g-r$ colors calculated in Section 4.2 along with the bolometric correction (BC) coefficients of J. D. Lyman et al. (2014, 2016) to compute bolometric LCs for our sample. According to J. D. Lyman et al. (2014), stripped-envelope supernovae possess a BC as follows:

$$\mathrm{BC}_g = 0.054 - 0.195 \times (g-r) - 0.719 \times (g-r)^2. \quad (2)$$

This BC is valid after the initial shock-breakout phase. We calculate the BC_g coefficient for every epoch in our sample using the GP-interpolated data. Then, using the definition of BC coefficients,

$$\mathrm{BC}_x = M_{\mathrm{bol}} - M_x, \quad (3)$$

where x is the relevant filter, M_{bol} is the absolute bolometric magnitude, and M_x is the absolute magnitude in the relevant filter, we calculate M_{bol} at every epoch. In Figure 12, we show

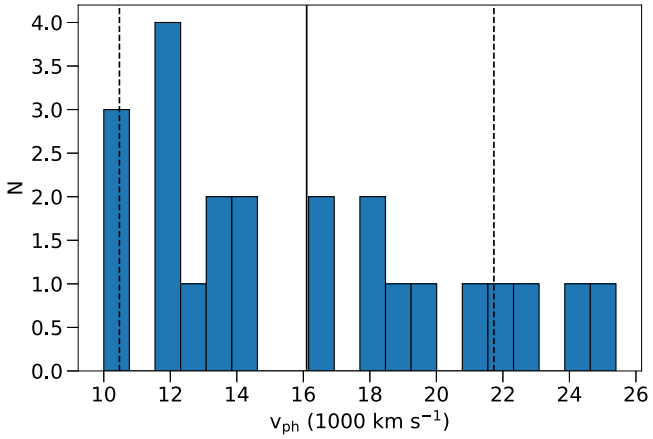

Figure 10. The peak v_{ph} for the sample, with the mean velocity (16,100 km s^{-1}) shown with a solid line, and 1σ standard deviation (5600 km s^{-1}) range shown with dashed lines.

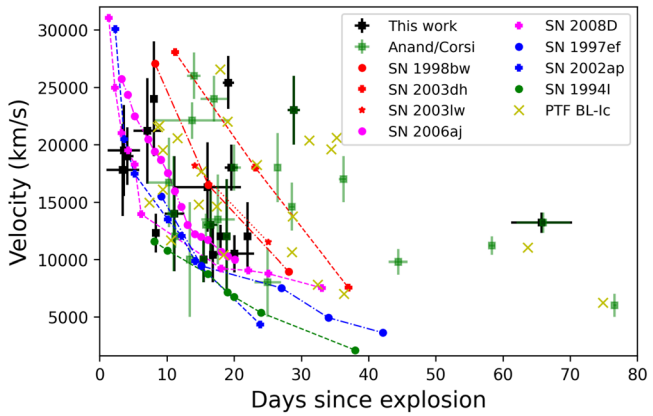

Figure 11. SN velocities measured from the Fe II 5169 Å line as a function of the spectroscopic phase for every event in the sample for which a velocity was obtained (26 events). The black points indicate the velocities at the spectral epoch, plotted with measured velocities of SNe Ic-BL from literature, the iPTF sample (F. Taddia et al. 2019), and the samples from S. Anand et al. (2024) and A. Corsi et al. (2023). Red symbols represent GRB-SNe (K. Iwamoto et al. 1998; P. A. Mazzali et al. 2003, 2006b); magenta represents XRF/X-ray transient-SNe (P. A. Mazzali et al. 2006a; E. Pian et al. 2006; M. Modjaz et al. 2009); blue represents SNe Ic-BL (P. A. Mazzali et al. 2000, 2002); and green represents the "normal" Type Ic SN 1994I (D. N. Sauer et al. 2006).

Table 4
Na I EW and Host-galaxy Extinction Upper Limits for Events Having Evidence of Na I Absorption

Event	$\mathrm{EW}_{\mathrm{Na\ I}}$ (Å)	$<A_V^{\mathrm{host}}$ (mag)
SN 2018hsf	1.23 ± 0.14	1.3
SN 2018keq	1.01 ± 0.33	1.2
SN 2019hsx	0.80 ± 0.39	1.1
SN 2019lci	0.47 ± 0.22	0.6
SN 2020ayz	1.52 ± 0.13	1.5
SN 2020bvc	0.55 ± 0.17	0.7

the distribution of $M_{\mathrm{bol}}^{\mathrm{max}}$ for the sample. The distribution ranges from -16.28 to -20.91 mag, and we find an average $\overline{M}_{\mathrm{bol}}^{\mathrm{max}}$ of -18.34 ± 0.16 mag, with a 1σ standard deviation of 0.98 mag. This is consistent with the value found in F. Taddia et al. (2019), who found $\overline{M}_{\mathrm{bol}}^{\mathrm{max}} = -18.5$ with a 1σ standard

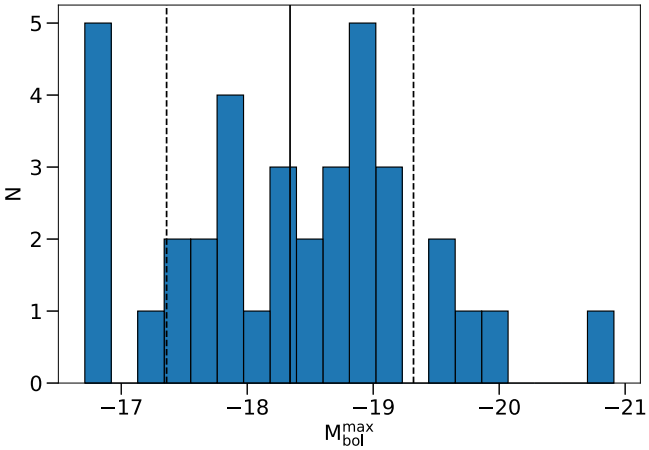

Figure 12. M_{bol}^{max} of all SNe in the sample, with the mean magnitude (−18.34 mag) shown with a solid line, and 1σ standard deviation range (0.98 mag) shown with dashed lines.

deviation of 0.5 mag. When excluding SLSN SN 2020wgz from the sample, we find an average $\overline{M_{bol}^{max}}$ of -18.27 ± 0.15 mag, with a 1σ standard deviation of 0.89 mag.

We then convert M_{bol} to a bolometric luminosity. To calculate uncertainties we include the photometric uncertainty on the peak magnitude that we estimate from the GP analysis and a 15% correction to take into account Milky Way extinction, a peculiar velocity correction uncertainty of 150 km s^{-1}, and the uncertainty of the Hubble constant, ± 3 km s^{-1} Mpc^{-1}. In Figure 13, we show the bolometric luminosity LCs of our sample.

6.2. Blackbody Temperature and Radii Evolution

Because we have multiband photometry, we are able to investigate the spectral energy distribution (SED) evolution over time for the events in our sample. In particular, we calculate how the blackbody temperature and radius evolve over time, through fitting a diluted blackbody function to the SEDs:

$$F_\lambda = (R/d)^2 \cdot \epsilon^2 \cdot \pi \cdot B(\lambda, T) \times 10^{-0.4 \cdot A_\lambda}. \quad (4)$$

In this function, F_λ is the flux at wavelength λ, B is the Planck function, A_λ is the extinction, T is the temperature, R is the radius, d is the distance, and ϵ is the dilution factor (R. G. Eastman et al. 1996; M. Hamuy et al. 2001; L. Dessart & D. J. Hillier 2005) representing a correction between the blackbody distribution we fit to the observed fluxes.

The SEDs consist of photometry binned within 0.5 days of each other, using g-, r-, and i-band data. For some cases, we also have Swift host-corrected UVOT photometry (detailed in Section 3.7) and include those points in the SEDs when available. We estimate the luminosity by integrating the blackbody distributions from 2000 to 20000 Å. The blackbody temperature and radius evolution over time are shown in Figure 14. We find that the temperature shows a progressive decline until ∼5 days after peak, when the distribution begins to flatten out between 4000 and 7000 K, which is similar to what is found in F. Taddia et al. (2019). We find that the radius increases to around 10 days after peak and then decreases for the majority of the sample, again consistent with what is found in F. Taddia et al. (2019).

7. Explosion Properties

After computing bolometric LCs, we fit the LCs up to the peak luminosity (usually 20–60 rest-frame days from first detection) to analytic models from W. D. Arnett (1982). In these models, the instantaneous heating rate from the decay of ^{56}Ni and ^{56}Co is equivalent to the peak bolometric luminosity of the SN. The model also assumes spherical symmetry in the explosion and full gamma-ray trapping of the ejecta. In these models, the nickel mass (M_{Ni}) and characteristic photon diffusion timescale (τ_m) are free parameters. These parameters are important probes of the explosion mechanisms, as the amount of M_{Ni} powers the bolometric LC, while τ_m is a proxy for the rise timescale of the SN, along with relating to the kinetic energy (E_K) and ejecta mass (M_{ej}) of the SN. We note that A. Corsi et al. (2023) and S. Anand et al. (2024) used the same methods to derive the explosion parameters for events in their sample, so for overlapping events we report the values derived in their works.

We use HAFFET to generate semianalytic bolometric luminosity LCs corresponding to different M_{Ni} and τ_m values and use Markov Chain Monte Carlo techniques to find the best fit and 16%, 50%, and 84% confidence interval values corresponding to each event not presented in A. Corsi et al. (2023) and S. Anand et al. (2024). The distribution of M_{Ni} masses derived is shown in Figure 15, and the values along with their statistical uncertainties are reported in Table 5. The values range from 0.05 to 2.46 $M_\odot$, with a mean of $0.37^{+0.08}_{-0.06}$ $M_\odot$ and a 1σ standard deviation of 0.42 $M_\odot$. This is consistent with the normal SNe Ic-BL SN sample from F. Taddia et al. (2019), who found a mean value of 0.31 $M_\odot$ with a 1σ standard deviation of 0.17 $M_\odot$. Twelve events in our sample were also included in Ó. Rodríguez et al. (2023), who performed a systematic study of the iron yield in different classes of stripped-envelope SNe. They find an average nickel mass of SNe Ic-BL of 0.14 ± 0.02 $M_\odot$, which is around a factor of 2 less than the value we derived. This is due to a different fitting procedure, as they calculated the nickel masses based on the radioactive decay tail, rather than the peak of the LC using the W. D. Arnett (1982) model. Due to the Malmquist bias (see Section 4.2, where the peak absolute magnitude distribution is 0.2 mag lower after accounting for this effect), the corrected nickel mass distribution is 17% lower than what we measure (F. Taddia et al. 2019), which is a small effect. When we exclude the SLSN SN 2020wgz from the sample, we find a new mean of 0.32 ± 0.03 $M_\odot$ and 1σ standard deviation of 0.21 $M_\odot$.

We note that for SN 2020bvc the M_{Ni} we derive (0.41 ± 0.01 $M_\odot$) is inconsistent with what is derived in A. Y. Q. Ho et al. (2020b), 0.13 ± 0.01 $M_\odot$. The reason for this discrepancy is that A. Y. Q. Ho et al. (2020b) used the radioactive decay tail to derive M_{Ni} rather than the peak of the LC. However, the M_{Ni} we derive is consistent with the results from J. Rho et al. (2021), who found $M_{Ni} \sim 0.4$ $M_\odot$. This value is likely more accurate as they used hydrodynamical LC modeling to derive this value. The value we derive for SN 2018gep ($M_{Ni} = 0.13 \pm 0.01$ $M_\odot$) is consistent with what is found in A. Y. Q. Ho et al. (2019), $M_{Ni} < 0.3$ $M_\odot$. The value we derive for SN 2018bvw ($M_{Ni} = 0.52 \pm 0.05$ $M_\odot$) is slightly larger than the value derived in A. Y. Q. Ho et al. (2020a) of ∼0.3 $M_\odot$, though they did not report any errors in their work.

Armed with τ_m and v_{ph}, we then derive the M_{ej} and E_{KE} for each of the events in our sample using the equations from

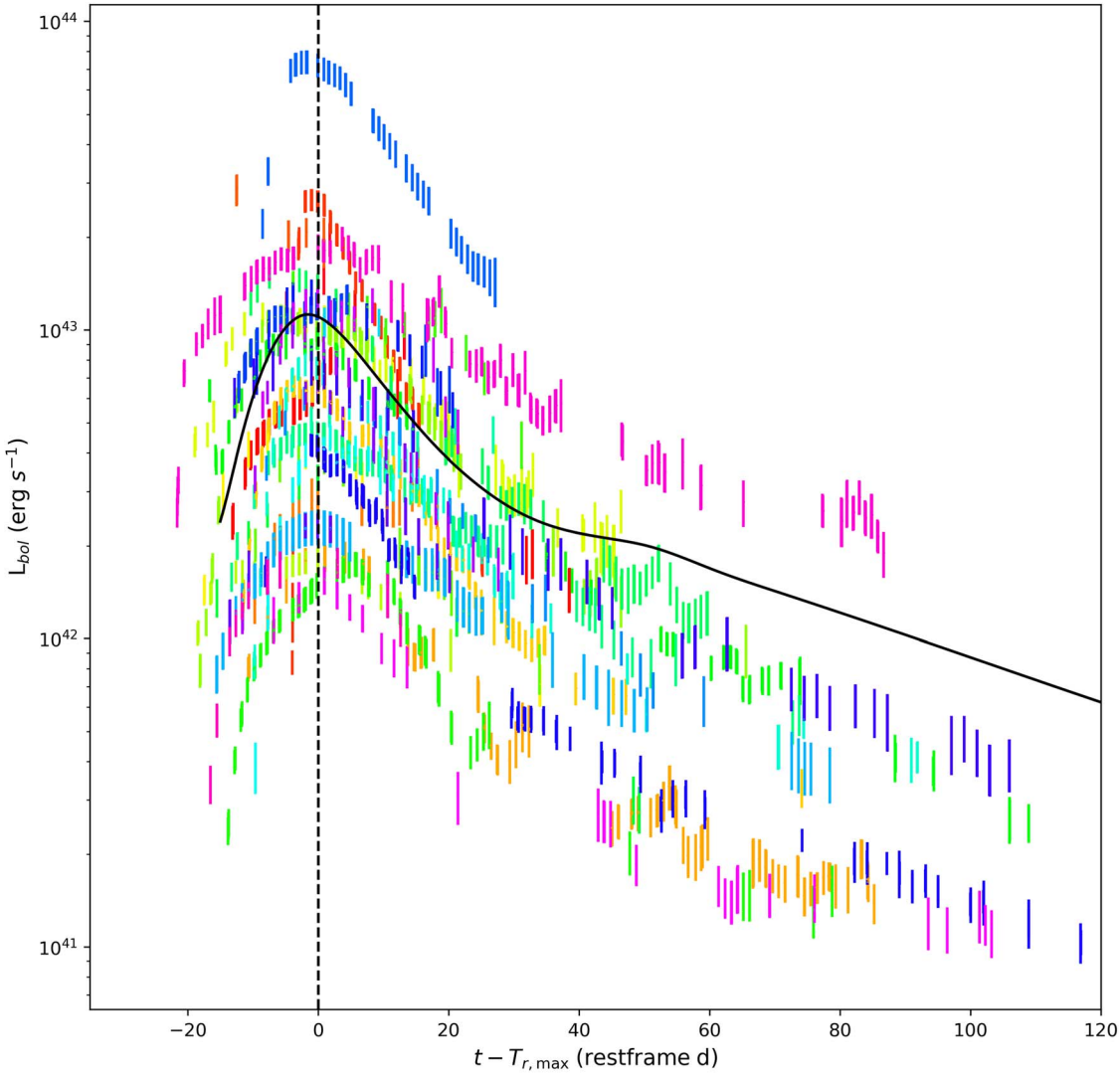

Figure 13. Bolometric luminosity LCs for the SNe Ic-BL sample, calculated using Lyman BC coefficients (described in Section 6.1). The bolometric luminosity LC of SN 1998bw (A. Clocchiatti et al. 2011) is also shown as comparison.

J. D. Lyman et al. (2016). $M_{\rm ej}$ is described as

$$M_{\rm ej} = \frac{\tau_{\rm m}^2 \beta c v_{\rm sc}}{2\kappa_{\rm opt}}, \quad (5)$$

and $E_{\rm KE}$ is described as

$$E_{\rm KE} = \frac{3 v_{\rm sc}^2 M_{\rm ej}}{10}, \quad (6)$$

where $\beta = 13.8$ is a constant, c is the speed of light, $\kappa_{\rm opt}$ is a constant, average optical opacity, and $v_{\rm sc}$ is the photospheric velocity $v_{\rm ph}$ at maximum light. Opacity $\kappa_{\rm opt}$ varies in the literature for stripped-envelope SNe, and we adopt the value used by N. N. Chugai (2000), L. Tartaglia et al. (2021), and C. Barbarino et al. (2021), $\kappa_{\rm opt} = 0.07\,{\rm cm^2\,g^{-1}}$ (which was shown to accurately recreate hydrodynamical LCs of observed stripped-envelope SNe; F. Taddia et al. 2018).

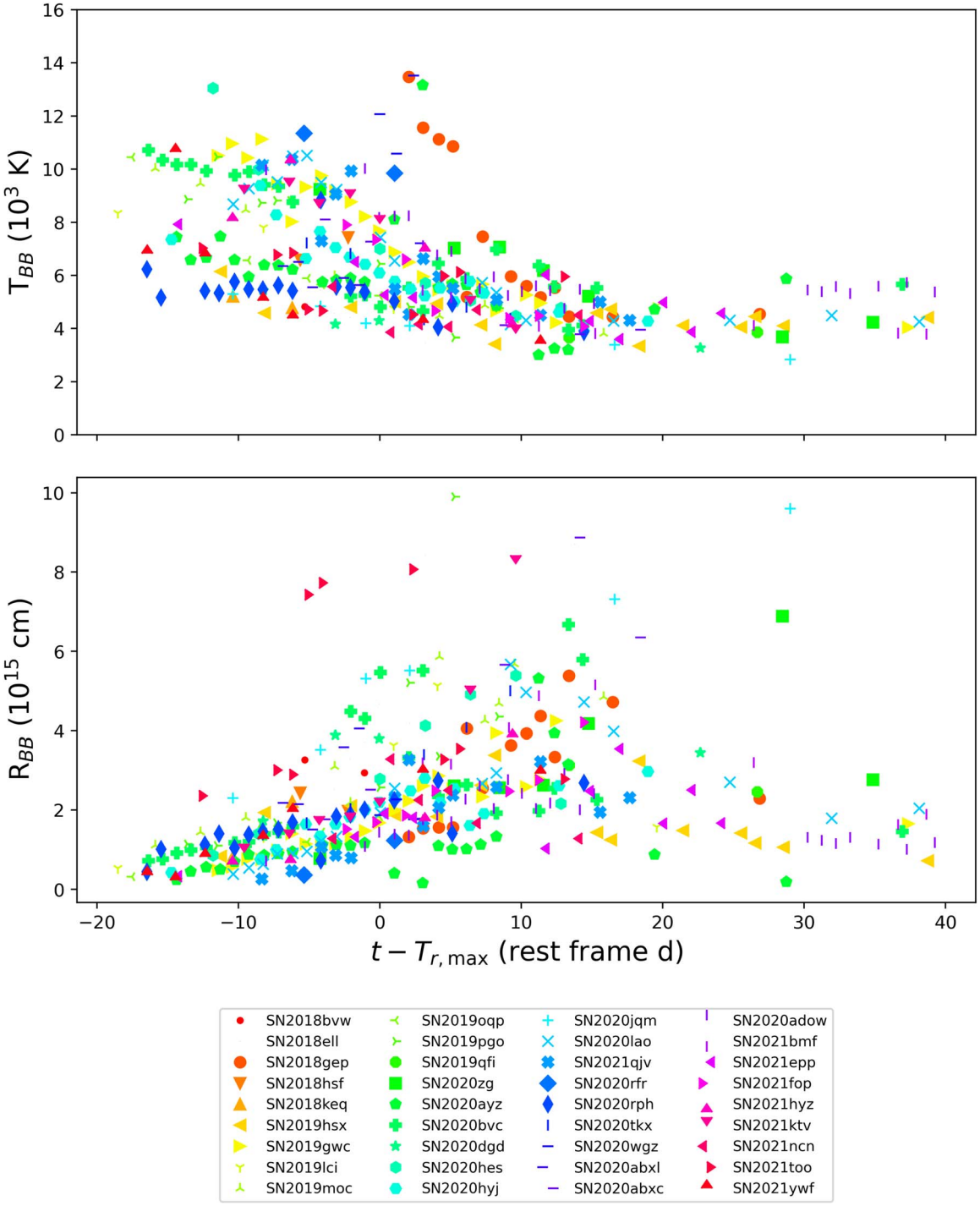

Figure 14. Blackbody temperature and radii evolution for the SNe Ic-BL sample, calculated through the methods reported in Section 6.2.

Because a measurement of $v_{\rm ph}$ is needed to derive $M_{\rm ej}$ and $E_{\rm KE}$, we were able to derive values for the 20 events that we estimated $v_{\rm ph}$ at peak for (described in Section 5). For the six events that did not have spectra within 15 days of the peak epoch, we derive lower limits on their $M_{\rm ej}$ and $E_{\rm KE}$. We present the values in Table 5 and show their distributions in Figure 15. The $M_{\rm ej}$ values range from 0.2 to 8.05 $M_\odot$, with a mean of $2.45^{+0.47}_{-0.41}$ $M_\odot$ and 1σ standard deviation of 2.35 $M_\odot$. This is consistent with the normal Ic-BL sample from F. Taddia et al. (2019), who found a mean value of 4.0 $M_\odot$ with a 1σ standard deviation of 2.9 $M_\odot$. $E_{\rm KE}$ ranges from 6.6×10^{50} erg to 2.4×10^{52} erg, with an average of $4.02^{+1.37}_{-1.00} \times 10^{51}$ erg and 1σ standard deviation of 6.60×10^{51} erg. This is consistent with the distribution found in F. Taddia et al. (2019), who found an average of 7×10^{51} erg with a 1σ standard deviation of 5.8×10^{51} erg.

In Figure 16, we plot the three explosion parameters against each other to test for the presence of any correlations using the Spearman rank test. We find no significant correlations between $M_{\rm Ni}$ and $M_{\rm ej}$ (p-value of 0.86), no correlation between $M_{\rm Ni}$ and $E_{\rm K}$ (p-value of 0.75), and a significant correlation between $M_{\rm ej}$ and $E_{\rm K}$ (p-value of 0.007). The correlation

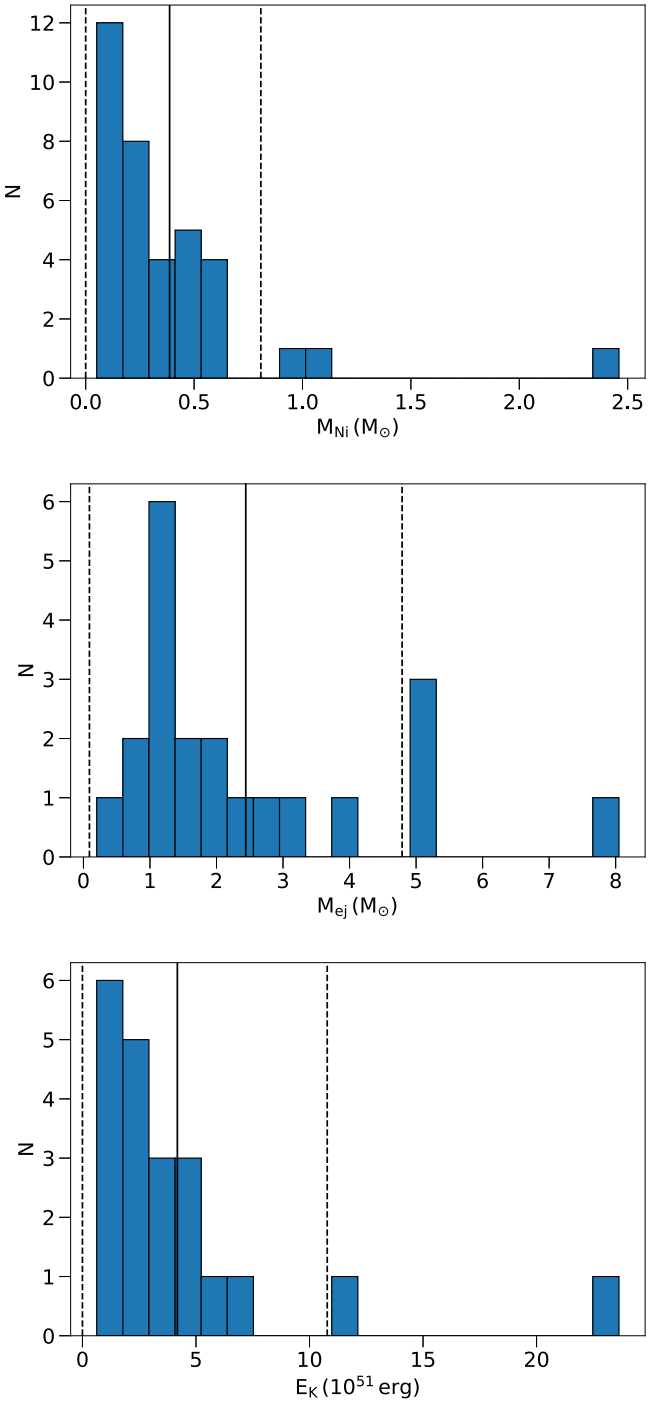

Figure 15. Histograms of the explosion properties derived for the Ic-BL sample. The mean values and 1σ dispersions for the properties are shown with solid and dashed lines, respectively. Top panel: the M_{Ni} distribution for the SNe Ic-BL sample. Middle panel: the M_{ej} distribution for the SNe Ic-BL sample. Lower panel: the E_K distribution for the SNe Ic-BL sample.

between M_{ej} and E_K is expected due to the relationships shown in Equations (5) and (6).

We also show the boundary of $M_{Ni} = M_{ej}/2$, which is the boundary used by F. Taddia et al. (2019) that indicates a shift from an event powered by radioactive decay up to its peak luminosity to one that must be powered by additional mechanisms, including the spindown of a magnetar (D. Kasen & L. Bildsten 2010). We note that there is one event (SN 2018gep) that is clearly in this regime, and A. Y. Q. Ho et al. (2019) showed that this event is best modeled as a shock-breakout event in a dense circumstellar medium. There are two events whose error bars extend into this regime (SN 2019pgo and SN 2020hes), and one event that has $M_{Ni} > M_{ej}/2$, SN 2021ktv. However, SN 2021ktv's error bars for M_{ej} make it uncertain that it solely exists in this regime, so we cannot firmly establish the presence of any additional powering mechanisms for these three events through this method. SN 2018hsf possesses a relatively high $M_{Ni} = 0.7\,M_\odot$, and the lower limits derived for M_{ej} find $M_{ej} > 0.31$. Therefore, it is possible that SN 2018hsf possesses additional powering mechanisms. SN 2020wgz also likely exists in this regime, as it possesses an extremely high $M_{Ni} = 2.46\,M_\odot$ and also has a luminosity that places it in the regime of SLSN. However, only lower limits on its M_{ej} and E_K were derived due to a lack of a velocity measurement close to peak light. We provide more details on this event in Section 7.1.

7.1. SN 2020wgz—an SLSN-I?

SLSNe are a subclass of SNe that can reach peak magnitudes of ~ -21 mag, a factor of 100 more than normal CCSNe (R. M. Quimby et al. 2011; A. Gal-Yam 2012). A subset of SLSNe do not show hydrogen features in their spectra and are classified as SLSN-I. These events have slow rise times and peak much later than normal CCSNe (typically 20–100 days after explosion). SLSN-I spectra possess a blue continuum, often along with Fe II, Mg II, and O II absorption lines. Due to their high luminosity and spectral composition, the spindown of magnetar is the most favored physical model for describing these events (L. Dessart et al. 2012).

SN 2020wgz possesses a peak absolute bolometric magnitude of $M_{bol}^{max} = -20.91 \pm 0.09$ mag, placing it in the luminosity class of SLSNe. The two spectra obtained near peak light shown in the Appendix show no hydrogen features, along with a blue featureless continuum. The spectra are too low quality/noisy to make out the presence of any absorption features. Therefore, SN 2020wgz's LC and early time spectra have similarities to SLSN-I. However, SN 2020wgz has a rapid rise time of $\sim$10 days, differing from normal SLSN-I. Furthermore, a spectrum taken 21 days after peak shows a transition to a redder continuum, along with the development of broad spectral features, which enabled a classification of SN Ic-BL.

SN 2011kl is an SLSN-I that was associated with an ultra-long GRB 111209A (J. Greiner et al. 2015). To date, it is the only SN associated with a GRB that is not an SN Ic-BL. SN 2020wgz possesses a peak absolute magnitude around 1 order of magnitude higher than SN 2011kl ($M_{bol}^{max} \sim -20.0$ mag) and has a similar rise time to SN 2011kl ($\sim$14 days). However, SN 2011kl's spectra do not show the same transition to a redder continuum and the development of broad absorption features that SN 2020wgz does. LC modeling of SN 2011kl showed that it likely was solely powered by a magnetar.

This spectral transition was seen in a few other objects (e.g., A. Pastorello et al. 2010), and most recently in SLSN-I SN 2017dwh (P. K. Blanchard et al. 2019), which was a nickel-rich SLSN-I possessing a similar but slightly fainter peak absolute magnitude of ~ -20.5 mag and a slightly longer rise time of $\sim$19 days. P. K. Blanchard et al. (2019) found that the high amount of nickel in the explosion may be due to enhanced production, or due to more efficient mixing of Fe group elements in the outer ejecta. They concluded that SN 2017dwh

Table 5
Explosion Properties and Photospheric Velocities for the SNe Ic-BL Sample

ZTF name	SN Name	M_{Ni} ($M_\odot$)	E_K (10^{51} erg)	M_{ej} ($M_\odot$)	v_{ph} (10^3 km s^{-1})	Spectrum Phase (day)
ZTF18aaqjovh	SN 2018bvw	$0.52^{+0.05}_{-0.05}$	4.45 ± 2.7	1.66 ± 0.5	21.2 ± 4.6	−1
ZTF18abhhnnv	SN 2018ell	$0.31^{+0.01}_{-0.01}$	11.44 ± 3.84	3 ± 0.35	25.4 ± 2.3	3.2
ZTF18abukavn	SN 2018gep	$0.61^{+0.01}_{-0.01}$	0.7 ± 0.6	0.2 ± 0.04	24 ± 5	4
ZTF18acbvpzj	SN 2018hsf	$0.7^{+0.13}_{-0.1}$	>0.07	>0.31	8.2 ± 0.94	23.7
ZTF18acxgoki	SN 2018keq	$0.16^{+0.05}_{-0.05}$	…	…	…	…
ZTF19aawqcgy	SN 2019hsx	$0.07^{+0.01}_{-0.01}$	0.99 ± 0.5	1.64 ± 0.43	10 ± 2	−0.2
ZTF19aaxfcpq	SN 2019gwc	$0.22^{+0.01}_{-0.01}$	>0.44	>0.6	11.1 ± 0.9	46.0
ZTF19abfsxpw	SN 2019lci	$0.24^{+0.01}_{-0.01}$	…	…	…	…
ZTF19ablesob	SN 2019moc	$0.52^{+0.01}_{-0.02}$	3.48 ± 1.85	2.09 ± 0.5	16.8 ± 3.9	−9.7
ZTF19abqshry	SN 2019oqp	0.08^{+0}_{-0}	…	…	…	…
ZTF19abupned	SN 2019pgo	$0.55^{+0.01}_{-0.01}$	0.89 ± 0.6	1.37 ± 0.4	10.4 ± 2.4	1
ZTF19abzwaen	SN 2019qfi	$0.13^{+0.01}_{-0.01}$	>0.7	>1.22	9.59 ± 1.2	29.3
ZTF20aafmdzj	SN 2020zg	$0.5^{+0.01}_{-0.01}$	…	…	…	…
ZTF20aaiqiti	SN 2020ayz	0.07^{+0}. $01_{-0.01}$	1.85 ± 0.92	2 ± 0.3	12.3 ± 1.7	−6.1
ZTF20aalxlis	SN 2020bvc	$0.41^{+0.01}_{-0.01}$	5.15 ± 2.45	2.39 ± 0.45	19 ± 2.5	−14
ZTF20aapcbmc	SN 2020dgd	$0.13^{+0.03}_{-0.03}$	3.07 ± 2.42	2.81 ± 1.5	13.5 ± 3.9	−0.43
ZTF20aaurexl	SN 2020hes	$0.58^{+0.01}_{-0.01}$	2 ± 1.9	1.26 ± 0.36	16.3 ± 3.9	0
ZTF20aavcvrm	SN 2020hyj	$0.22^{+0.01}_{-0.01}$	…	…	…	…
ZTF20aazkjfv	SN 2020jqm	$0.29^{+0.05}_{-0.04}$	5 ± 3	5 ± 1	13 ± 3	−0.5
ZTF20abbplei	SN 2020lao	$0.23^{+0.01}_{-0.01}$	2.48 ± 0.71	1.22 ± 0.16	18 ± 2	9
ZTF20abrmmah	SN 2020rfr	$0.47^{+0.03}_{-0.03}$	…	…	…	…
ZTF20abswdbg	SN 2020rph	$0.07^{+0.01}_{-0.01}$	3.08 ± 2.81	3.83 ± 1.59	12 ± 5	−1
ZTF20abzoeiw	SN 2020tkx	$0.22^{+0.01}_{-0.01}$	>1.5	>1.5	13.2 ± 0.9	53
ZTF20achvlbs	SN 2020wgz	$2.46^{+0.02}_{-0.02}$	>0.12	>0.48	11.1 ± 0.3	25
ZTF20acvcxkz	SN 2020abxl	$0.4^{+0.01}_{-0.01}$	…	…	…	…
ZTF20acvmzfv	SN 2020abxc	$0.61^{+0.02}_{-0.02}$	…	…	…	…
ZTF20adadrhw	SN 2020adow	$0.14^{+0.02}_{-0.02}$	2.2 ± 1.1	1 ± 0.2	19.5 ± 3.96	−7.9
ZTF21aagtpro	SN 2021bmf	$0.98^{+0.16}_{-0.17}$	23.63 ± 16.14	8.05 ± 5.37	21.9 ± 1.5	−10.0
ZTF21aaocrlm	SN 2021epp	$0.12^{+0.02}_{-0.02}$	6 ± 5	5 ± 2	14 ± 5	−4
ZTF21aapecxb	SN 2021fop	0.19^{+0}_{-0}	…	…	…	…
ZTF21aartgiv	SN 2021hyz	$0.29^{+0.01}_{-0.02}$	>4	>1.3	23 ± 3	16
ZTF21aaxxihx	SN 2021ktv	$0.48^{+0.01}_{-0.01}$	0.63 ± 0.4	0.95 ± 0.2	10.5 ± 1.6	8.2
ZTF21abchjer	SN 2021ncn	$0.05^{+0.01}_{-0.01}$	…	…	…	…
ZTF20abcjdwu	SN 2021qjv	$0.17^{+0.01}_{-0.01}$	1 ± 1	1.16 ± 0.35	12 ± 3	11.3
ZTF21abmjgwf	SN 2021too	$0.92^{+0.03}_{-0.03}$	6.42 ± 2.09	5.06 ± 0.78	14.4 ± 2.1	5.4
ZTF21acbnfos	SN 2021ywf	$0.06^{+0.01}_{-0.01}$	0.9 ± 0.3	1.1 ± 0.2	12 ± 1	0.5

Note. Values reported include those newly derived and those presented in previous works.

was likely powered by a combination of the spindown of a magnetar and radioactive decay. This event provides evidence that the progenitors for SLSN-I and SNe Ic-BL might be similar for certain cases.

In Section 7, we determined that SN 2020wgz had too high of a nickel mass to be powered purely by the W. D. Arnett (1982) model. Utilizing the spectral similarities to SN 2017dwh, we use the open-source electromagnetic transient Bayesian fitting software package `redback` to fit a `general magnetar driven supernova` model (C. M. B. Omand & N. Sarin 2024) to the observed *r*- and *g*-band LCs. This model utilizes the combination of both the spindown of a magnetar along with radioactive decay to power the LC. We show the best-fit model in Figure 17, along with the corner plot in the Appendix. We see that the model fits the LC well in both the *g* and *r* bands, showing that it is likely SN 2020wgz was powered by a magnetar, at least to some extent.

8. Discussion in Context of Multiwavelength Observations

There are eight events in the sample that have transient radio counterparts (SN 2018bvw, SN 2018gep, SN 2020tkx, SN 2020jqm, SN 2020bvc, SN 2020adow, SN 2021bmf, and SN 2021ywf). SN 2018bvw, SN 2018gep, and SN 2020tkx are subjects of single-object papers, and the physical mechanisms of their explosions are discussed at length in those works. SN 2018bvw likely is a transition event between engine-driven GRB-SNe (A. Y. Q. Ho et al. 2020a) and normal SNe Ic-BL, and the event shows possible signs of harboring a mildly relativistic jet. SN 2018gep originates from a shock breakout in a massive shell of dense circumstellar material without an accompanying relativistic jet (A. Y. Q. Ho et al. 2019; S.-C. Leung et al. 2021; T. A. Pritchard et al. 2021), and SN 2020bvc shows a double peak LC due to shock cooling emission followed by radioactive decay, with the event showing similar multiwavelength features to low-luminosity

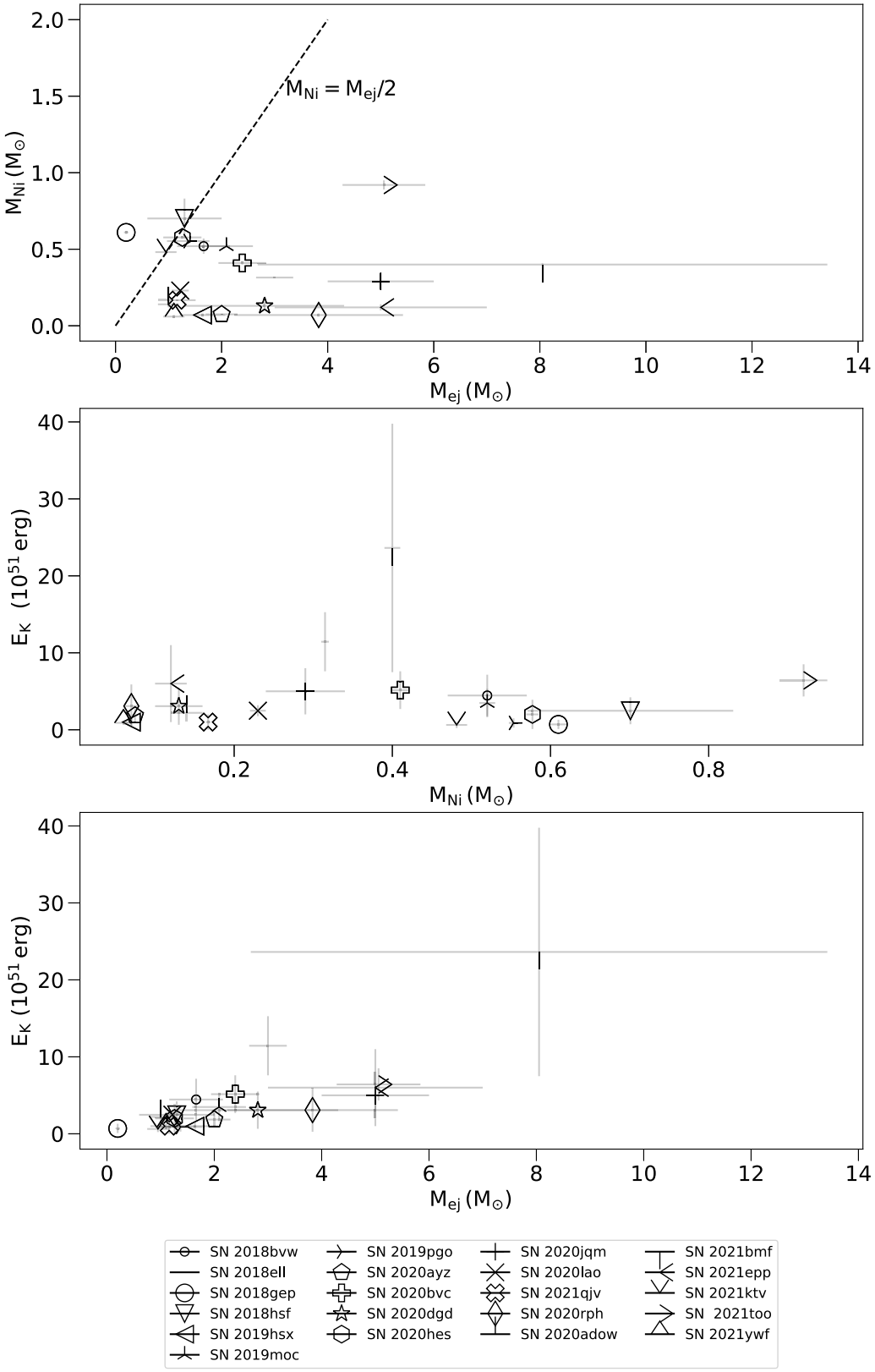

Figure 16. Explosion properties (M_{Ni}, M_{ej}, and E_K) plotted against each other. Top panel: M_{Ni} plotted against M_{ej}. We do not find any correlations between the two, with a p-value of 0.86. The dashed line indicates the boundary of $M_{Ni} = M_{ej}/2$. Events above that boundary are likely not solely powered by radioactive decay (D. Kasen & L. Bildsten 2010). Middle panel: E_K plotted against M_{Ni}. We do not find any correlation between the two, with a p-value of 0.75. Bottom panel: E_K plotted against M_{ej}. We find a significant correlation between the two, with a p-value of 0.007.

GRB 060218/SN 2006aj. This event also shows signs of mildly relativistic ejecta (A. Y. Q. Ho et al. 2020b; L. Izzo et al. 2020). Furthermore, A. Corsi et al. (2023) showed that SN 2020jqm's erratic radio LC and derived shock properties place it in the same regime as radio-loud circumstellar medium–interacting SNe like PTF11qcj (A. Corsi et al. 2014). The rest

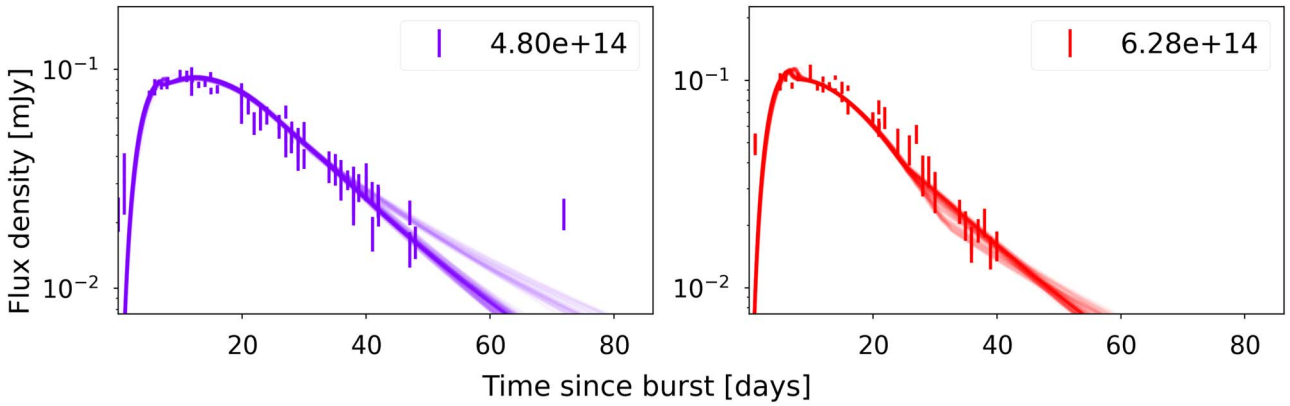

Figure 17. The best-fit magnetar powered model fit to SN 2020wgz in the *r* band on the left, and *g* band on the right.

of the events only have one to two radio observations, making multiwavelength modeling efforts for these objects rather non-constraining with respect to both model comparison and parameter estimation. However, we include multiwavelength modeling efforts for SN 2020tkx, SN 2020adow, and SN 2021ywf in the Appendix. Modeling efforts for SN 2021bmf will be explored in a future work.

8.1. Search for Gamma Rays

Using the derived explosion epochs for the sample, we search for potential GRB coincidences in several online archives. A. Corsi et al. (2023) did this search for their sample of events, which includes eight of the events in our sample. They found no Swift or Fermi GRBs spatially and temporally coincident to any of their events. The only coincident GRBs were from the Konus instrument on the Wind satellite, which does not provide localizations. They found that the number of events found within the explosion epochs were consistent with random fluctuations, and also found that no events with an explosion epoch constrained to less than 1 day had a coincident GRB within that time frame. Furthermore, A. Y. Q. Ho et al. (2019) and A. Y. Q. Ho et al. (2020b) determined that SN 2018gep and SN 2020bvc had no GRB counterparts. A. Y. Q. Ho et al. (2020a) found that SN 2018bvw had one possible GRB counterpart from Wind-Konus, corresponding to a low-luminosity GRB on 2018 May 3 03:41:01; however, they determine that this association is most likely due to chance.

We repeat this search for the 25 events in our sample not covered above. We find no spatially and temporally coincident Swift or Fermi GRBs for any of the events. There were 11 SNe that had Wind-Konus GRBs that were detected within their explosion epochs, corresponding to 31 coincident GRB events over a time period of 78.29 days searched. This rate is also consistent with random fluctuations. Therefore, we determine that no events in the sample have certain, coincident gamma-ray emission.

8.2. Comparison of Explosion Properties with Radio Observations

We then test whether statistical differences exist between the explosion properties for the subsample of 13 events that have radio observations, between the eight events with detections and five events with non-detections (A. Corsi et al. 2023). In Figure 18, we show the distributions of $M_{\rm Ni}$, $M_{\rm ej}$, $E_{\rm K}$, and $v_{\rm ph}$ for the subsample with radio observations. Through running a two-sample Kolmogorov–Smirnov (K-S) test, we do not find statistical differences between the populations for any of the properties, though we note that due to the small sample sizes moderately different populations cannot be ruled out. We note that for the $M_{\rm ej}$ and $E_{\rm K}$ analysis we do not include events that only have lower limits derived. Specifically, we compute a K-S test statistic of 0.50 with a *p*-value of 0.31 for the $M_{\rm Ni}$ distribution, a K-S test statistic of 0.42 with a *p*-value of 0.66 for the $M_{\rm Ej}$ distribution, a K-S test statistic of 0.32 with a *p*-value of 0.89 for the $E_{\rm K}$ distribution, and a K-S test statistic of 0.71 with a *p*-value of 0.12 for the $v_{\rm ph}$ distribution.

We also investigate whether correlations exist between the peak radio luminosity and explosion properties. If correlations do exist, they may point to a connection between the optically described explosion properties and the existence of radio emission, possibly from accompanying off-axis relativistic jets. In order to check this, we extrapolate the peak radio fluxes for every event to 6 GHz through assuming a spectrum $F_\nu \propto \nu^{-1}$, and convert this flux to a luminosity using the distance of the SN. Once armed with the radio luminosities, we use a linear regression code, `Linmix`, that takes into account both detections and nondetections when fitting linear models to the data (B. C. Kelly 2007). `Linmix` assumes symmetric error bars, so for $M_{\rm Ni}$ values that have asymmetric error bars, we assume the larger error bar value for both the positive and negative error.

We show the linear regression results in Figure 19. For $M_{\rm Ni}$, we calculate a linear correlation coefficient of 0.32 ± 0.32, with a *p*-value of 0.33, showing there are no significant correlations present between the radio luminosity and the $M_{\rm Ni}$. For $M_{\rm ej}$, we calculate a linear correlation coefficient of 0.46 ± 0.32, with a *p*-value of 0.18, while for $E_{\rm K}$ we calculate a linear correlation coefficient of 0.58 ± 0.33 with a *p*-value of 0.11, again showing a lack of significant correlations. Finally, for $v_{\rm ph}$, we calculate a linear correlation coefficient of 0.17 ± 0.42, with a *p*-value of 0.70. We note that we do not include events that have lower limits for this analysis.

Therefore, we find that there are no statistically significant correlations between the radio luminosities and the explosion properties derived from optical data of SNe Ic-BL. We note that there do seem to be slightly positive correlations between the radio luminosities and $M_{\rm ej}$ and $E_{\rm K}$; however, these correlations are not statistically significant. Future radio observations of SNe Ic-BL will increase the sample of radio-detected events,

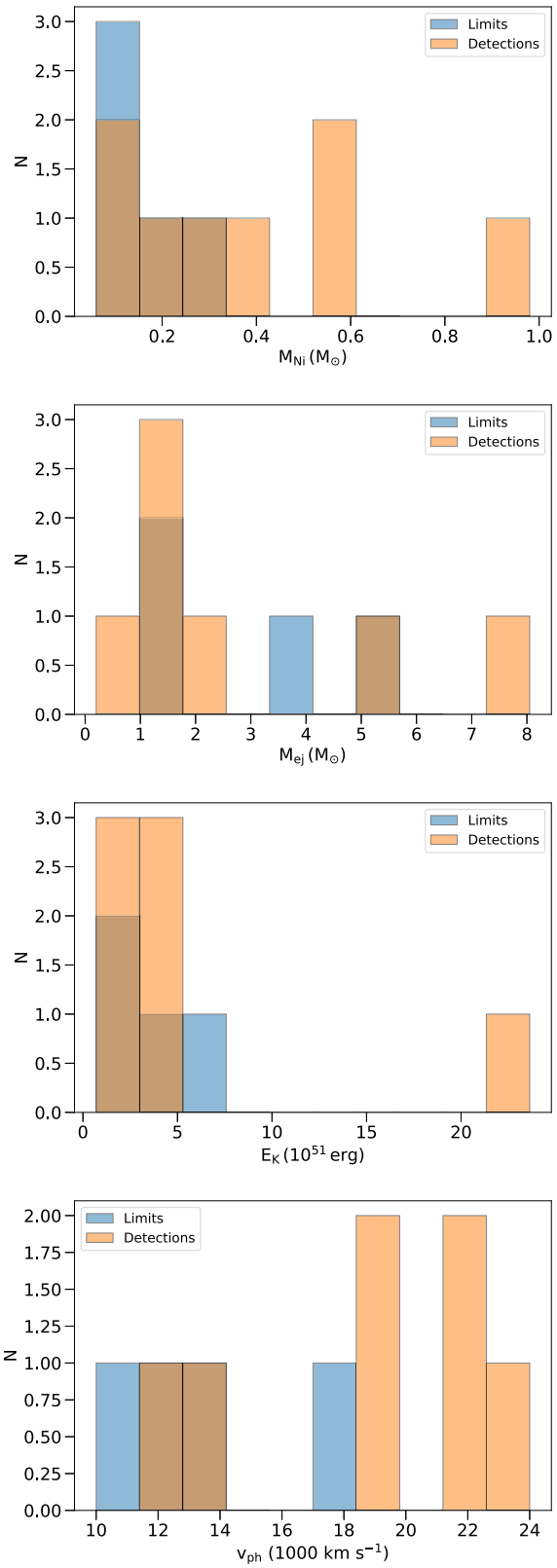

Figure 18. Histograms showing the distribution of explosion properties and v_{ph} for the population of events with radio observations. We distinguish events that have radio detections in orange and events that have radio nondetections in blue. We find no statistical differences between the populations for any of the properties.

and future analyzes can use this work as a stepping stone to probe deeper into the relationship between events' optical and radio properties.

9. Summary and Conclusions

We analyzed 36 SNe Ic-BL from ZTF between 2018 March and 2021 August as part of the BTS survey, building upon iPTF's sample reported by F. Taddia et al. (2019). We present the ZTF LCs, along with spectra obtained for every event. Below we present a summary of some of our findings:

1. We find the average peak absolute magnitude in r band of the sample $\bar{M}_{r,\mathrm{max}} = -18.51 \pm 0.15$ mag, with a 1σ standard deviation of 0.90 mag. This is consistent with the distribution from F. Taddia et al. (2019).
2. We calculate expansion velocities for each event with sufficient signal-to-noise ratio spectra to estimate the photospheric velocity at peak and find an average of $16{,}100 \pm 1100$ km s^{-1}, with a 1σ standard deviation of 5600 km s^{-1}.
3. We also utilize the W. D. Arnett (1982) model to determine the explosion properties for each of the events. We determine an average M_{Ni} of $0.39^{+0.08}_{-0.06}\,M_\odot$ and 1σ standard deviation of 0.42 $M_\odot$, an average M_{ej} of $2.45^{+0.47}_{-0.41}\,M_\odot$ and 1σ standard deviation of 2.35 $M_\odot$, and an average E_{KE} of $4.02^{+1.37}_{-1.00} \times 10^{51}$ erg and 1σ standard deviation of 6.5×10^{51} erg. All these values are consistent with the averages found in the previous sample of F. Taddia et al. (2019).
4. SN 2020wgz has the luminosity and spectral features of an SLSN-I that transitions to an SN Ic-BL. Its LC fits well to a magnetar and nickle-powered combined model.
5. We do not find associated gamma-ray emission for any of the events, through searches of archival data from gamma-ray satellites.
6. We find that SN 2018gep's radio detections reported in A. Y. Q. Ho et al. (2019) are from the transient and not its host galaxy. We also search the VLASS survey for any transient radio emission for the SNe, and find SN 2021bmf displays transient radio emission over the three epochs of the survey.
7. When comparing the optical properties of the radio-loud and radio-quiet population, we find no correlations between the radio luminosity and optical properties of the sample, showing evidence that the optically inferred explosion parameters alone are not sufficient to make inferences about relativistic jet formation mechanisms in SNe Ic-BL.

Disentangling the picture of SNe Ic-BL and their different physical mechanisms continues to be a challenging task, and this work shows that purely studying the global optical properties of SNe Ic-BL will limit our understanding of these explosions. Future radio studies are integral to understanding this landscape. These studies should follow up a large fraction of optically discovered SNe Ic-BL at early times across multiple epochs, enabling the creation of robust radio LCs or deep, constraining upper limits for a large amount of events. Furthermore, the next generation of X-ray space-based missions like Einstein Probe (W. Yuan et al. 2022) and SVOM (J. Wei et al. 2016) can be utilized to discover low-luminosity GRBs and X-ray flash events that peak at lower peak energies than normal GRBs. This will allow for more opportunities to study these understudied events' associated SNe Ic-BL and characterize a new subset of events within the landscape of relativistic stellar explosions.

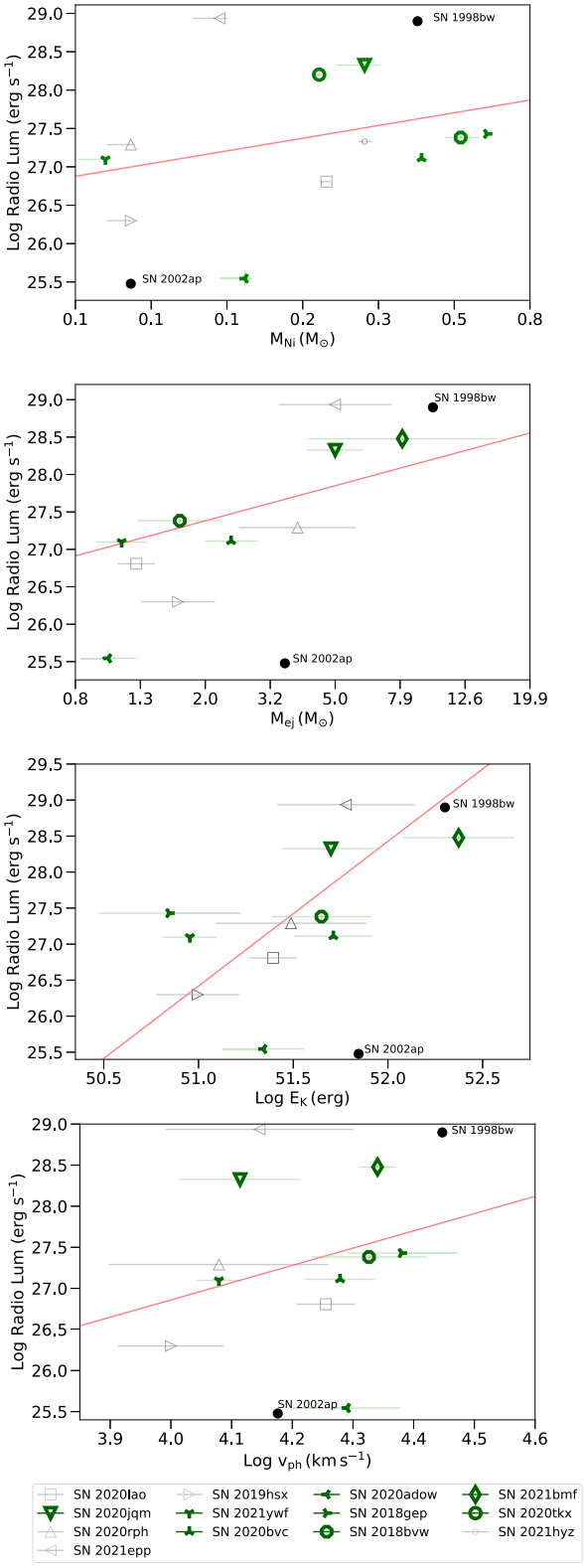

Figure 19. Best-fit Linmix linear regression model fitting between the peak radio luminosities and the explosion properties and photospheric velocities shown in red. Black points indicate limits, while green points indicate detections. We find no statistically significant correlations between the peak radio luminosities and any of the parameters. The parameters for SN 1998bw (J. Sollerman et al. 2000; K. W. Weiler et al. 2001) and SN 2002ap (E. Berger et al. 2002; P. A. Mazzali et al. 2002) are shown as reference.

Acknowledgments

G.P.S. thanks Alexander Dittman, Cole Miller, Isiah Holt, Muhammad Mousa, and Maryam Modjaz for useful discussions regarding this work. G.P.S. thanks Cristina Barbarino, Tassilo Schweyer, Joonas Viuho, and Amanda Djupvik for obtaining spectra from NOT. G.P.S. also thanks Simi Bhullar for her moral support throughout the paper-writing process. S. Y. acknowledges the funding from the National Natural Science Foundation of China under grant No. 12303046 and the Henan Province High-Level Talent International Training Program. S.A. acknowledges generous support from the David and Lucile Packard Foundation and the National Science Foundation GROWTH PIRE grant No. 1545949. A.C. acknowledges support from the National Science Foundation via AST-2431072, and from the NASA Swift GI program via the award 80NSSC23K0314. S.S. is partially supported by LBNL Subcontract No. 7707915. N.S. acknowledges support from the Knut and Alice Wallenberg foundation through the "Gravity Meets Light" project (PIs: Rosswog & Jerkstrand).

This work was supported by the GROWTH project (M. M. Kasliwal et al. 2019) funded by the National Science Foundation under grant No. 1545949. M.M.K. acknowledges generous support from the David and Lucille Packard Foundation. Some of the data presented herein were obtained at the W.M. Keck Observatory, which is operated as a scientific partnership among the California Institute of Technology, the University of California, and the National Aeronautics and Space Administration. The Observatory was made possible by the generous financial support of the W. M. Keck Foundation. The authors wish to recognize and acknowledge the very significant cultural role and reverence that the summit of Maunakea has always had within the indigenous Hawaiian community. We are most fortunate to have the opportunity to conduct observations from this mountain. SED Machine is based upon work supported by the National Science Foundation under grant No. 1106171. Based on observations obtained with the Samuel Oschin Telescope 48 inch and the 60 inch Telescope at the Palomar Observatory as part of the Zwicky Transient Facility project.

ZTF is supported by the National Science Foundation under grant No. AST-2034437 and a collaboration including Caltech, IPAC, the Weizmann Institute of Science, the Oskar Klein Center at Stockholm University, the University of Maryland, Deutsches Elektronen-Synchrotron and Humboldt University, the TANGO Consortium of Taiwan, the University of Wisconsin at Milwaukee, Trinity College Dublin, Lawrence Livermore National Laboratories, IN2P3, University of Warwick, Ruhr University Bochum, and Northwestern University. Operations are conducted by COO, IPAC, and UW. The ZTF forced-photometry service was funded under the Heising-Simons Foundation grant No. 12540303 (PI: Graham). The Gordon and Betty Moore Foundation, through both the Data-Driven Investigator Program and a dedicated grant, provided critical funding for SkyPortal. The Liverpool Telescope is operated on the island of La Palma by Liverpool John Moores University in the Spanish Observatorio del Roque de los Muchachos of the Instituto de Astrofisica de Canarias with financial support from the UK Science and Technology Facilities Council.

Appendix A
Discovery Paragraphs

Below we present the discovery paragraphs for every event. We note here that the first ZTF photometry reported is not from forced photometry, but from ZTF's nightly alerts that are reported to the Transient Name Server (TNS).

A.1. SN 2018bvw

We refer the reader to A. Y. Q. Ho et al. (2020a) for details about this event.

A.2. SN 2018ell

The first ZTF photometry of SN 2018ell (ZTF18abhhnnv) was obtained on 2018 July 17 (JD = 2,458,316.72). This first detection was in the r band with a host-subtracted magnitude of 20.09 ± 0.19 at $\alpha = 16^{\rm h}49^{\rm m}57\overset{\rm s}{.}02$, $\delta = +27°38'26.''94$ (J2000.0, throughout). The discovery was reported to TNS (C. Fremling 2018a) two days later on 2018 July 19, with a note saying the latest non-detection from ZTF was five days prior to discovery (July 12, $g > 20.81$). The event was first classified as a Type Ia SN based on a P60 SEDM spectrum obtained on 2018 July 31 (C. Fremling 2018a), but was reclassified two years later as a Type Ic-BL SN (A. Dahiwale & C. Fremling 2020a). The SN exploded in the outskirts of the spiral galaxy WISEA J164957.78+273828.3, with a well-established redshift of $z = 0.0638$.

A.3. SN 2018gep

We refer the reader to A. Y. Q. Ho et al. (2019), S.-C. Leung et al. (2021), and T. A. Pritchard et al. (2021) for details about this event.

A.4. SN 2018hsf

The first ZTF photometry of SN 2018hsf (ZTF18acbvpzj) was obtained on 2018 October 31 (JD = 2,458,422.83). This first detection was in the r band, with a host-subtracted magnitude of 19.58 ± 0.16 at $\alpha = 02^{\rm h}40^{\rm m}12\overset{\rm s}{.}78$, $\delta = -19°58'44.''94$. The discovery was reported to TNS (C. Fremling 2018b) with no prior non-detection from ZTF. The transient was classified as a Type Ic-BL event based on an LRIS spectrum obtained on 2018 December 4 (C. Fremling et al. 2018). The SN exploded in the plane of spiral galaxy PSO J040.0536-19.9798, and a redshift of $z = 0.119$ was determined through narrow host lines from the LRIS spectrum.

A.5. SN 2018keq

The first ZTF photometry of SN 2018keq (ZTF18acxgoki) was obtained on 2018 December 17 (JD = 2,458,469.59). This first detection was in the r band with a host-subtracted magnitude of 19.03 ± 0.10 at $\alpha = 23^{\rm h}22^{\rm m}41\overset{\rm s}{.}97$, $\delta = +21°00'43.''17$. The discovery was reported to TNS (C. Fremling 2020) two days later on 2018 December 19, with a note saying the latest non-detection from ZTF was four days prior to discovery ($r > 20.2$ mag). The event was classified as a Type Ic-BL SN (C. Fremling et al. 2019c) based on a spectrum obtained by LRIS on 2019 January 4. The SN exploded in the spiral galaxy SDSS J232241.80+210042.6, with a well-established redshift of $z = 0.038$.

A.6. SN 2019hsx

We refer the reader to S. Anand et al. (2024) for details about this event.

A.7. SN 2019gwc

We refer the reader to S. Anand et al. (2024) for details about this event.

A.8. SN 2019lci

The first ZTF photometry of SN 2019lci (ZTF19abfsxpw) was obtained on 2019 July 11 (JD = 2,458,675.79) with the P48. This first detection was in the g band, with a host-subtracted magnitude of 19.15 ± 0.12 at $\alpha = 16^{\rm h}31^{\rm m}01\overset{\rm s}{.}62$, $\delta = 8°28'23.''74$. The discovery was reported to TNS (J. Nordin et al. 2019) three days later on 2019 July 14, with a note saying that the latest nondetection was two hours prior to discovery ($g > 20.0$ mag). The transient was classified as a Type Ic-BL event based on a P60 SEDM spectra obtained on 2019 July 16 (A. Dugas et al. 2019). The SN exploded in the outskirts of spiral galaxy WISEA J163101.63+082829.7, with a well-established redshift of $z = 0.0292$.

A.9. SN 2019moc

We refer the reader to S. Anand et al. (2024) for details about this event.

A.10. SN 2019oqp

The first ZTF photometry of SN 2019oqp (ZTF19abqshry) was obtained on 2019 August 21 (JD = 2,458,716.66). This first detection was in the r band, with a host-subtracted magnitude of 20.20 ± 0.15 at $\alpha = 16^{\rm h}49^{\rm m}57\overset{\rm s}{.}02$, $\delta = 27°38'26.''94$. The discovery was first reported to TNS by ATLAS (J. Tonry et al. 2019) on 2021 August 25 ($c = 19.32$). The transient was classified as a Type Ic-BL event based on a DBSP spectrum obtained on 2019 August 27 (C. Fremling et al. 2019b). The SN exploded in the outskirts of the spiral galaxy MCG +08-30-042 with a redshift of $z = 0.0308$.

A.11. SN 2019pgo

The first ZTF photometry of SN 2019pgo (ZTF19abupned) on 2019 August 30 (JD = 2,458,725.89). The first detection was in the g band, with a host-subtracted magnitude of 20.69 ± 0.22 at $\alpha = 23^{\rm h}53^{\rm m}00\overset{\rm s}{.}05$, $\delta = 25°07'16.''46$. The discovery was reported by the Tsinghua-NAOC Transient Survey to TNS two days later (T. Zhang et al. 2019) on 2019 September 1. The transient was classified as a Type Ic-BL event based on a spectrum obtained on 2019 September 18 (C. Fremling et al. 2019a) with SPRAT on the Liverpool Telescope. The SN exploded in the galaxy WISEA J235300.28 +250717.2. The galaxy does not have a well-established redshift, but a redshift of $z = 0.0500$ was determined through narrow host lines from a Liverpool Telescope spectrum.

A.12. SN 2019qfi

We refer the reader to S. Anand et al. (2024) for details about this event.

A.13. SN 2020zg

The first ZTF photometry of SN 2020zg (ZTF20aafmdzj) was obtained on 2020 January 15 (JD = 2,458,863.63). The first detection was in the g band, with a host-subtracted magnitude of $g = 17.91 \pm 0.02$ at $\alpha = 4^{h}02^{m}36^{s}.40$, $\delta = -16°11'54.''33$. The discovery was reported to TNS (F. Forster et al. 2020d) with a note saying the latest nondetection by ZTF was two days prior to discovery on 2020 January 13 ($g > 19.32$). The transient was classified as a Type Ic-BL event (A. Dahiwale & C. Fremling 2020b) based on a DBSP spectrum obtained on 2020 February 26. The SN exploded in the edge of galaxy WISEA J040236.46-161152.0. The galaxy does not have a well-established redshift, but a redshift of $z = 0.0557$ was determined through narrow host lines from the DBSP spectrum.

A.14. SN 2020ayz

The first ZTF photometry of SN 2020ayz (ZTF20aaiqiti) was obtained on 2020 January 26 (JD = 2,458,874.83). The first detection was in the r band, with a host-subtracted magnitude of $r = 19.77 \pm 0.13$ at $\alpha = 12^{h}12^{m}04^{s}.90$, $\delta = 32°44'01.''73$. The discovery was reported to TNS (F. Forster et al. 2020e) on the same day ($g = 20.0$) with a note saying the latest nondetection by ZTF was three days prior to discovery on 2020 January 23 ($g > 20.23$). The transient was classified as a Type Ic-BL event (A. Dahiwale & C. Fremling 2020b) based on an SEDM spectrum obtained on 2020 February 03. The SN exploded in the center of the spiral galaxy MCG+06-27-025, with a well-established redshift of $z = 0.025437$.

A.15. SN 2020bvc

We refer the reader to A. Y. Q. Ho et al. (2020b), L. Izzo et al. (2020), J. Rho et al. (2021), and L. Li et al. (2023) for details about this event.

A.16. SN 2020dgd

We refer the reader to S. Anand et al. (2024) for details about this event.

A.17. SN 2020hes

The first ZTF photometry of SN 2020hes (ZTF20aaurexl) was obtained on 2020 April 14 (JD = 2,458,953.93). The first detection was in the g band, with a host-subtracted magnitude of $g = 18.62 \pm 0.07$ at $\alpha = 17^{h}47^{m}05^{s}.71$, $\delta = 42°46'39.''72$. The discovery was reported to TNS (F. Forster et al. 2020a) with a note saying the latest nondetection by ZTF was ten days prior to discovery on 2020 April 4 ($g > 20.60$). The transient was classified as a Type Ic-BL event (A. Dahiwale & C. Fremling 2020c) based on an SEDM spectrum obtained on 2020 April 25. The SN exploded in the galaxy WISEA J174706.10 +424640.5. The galaxy does not have a well-established redshift, but a redshift of $z = 0.0700$ was determined through narrow host lines from a DBSP spectrum.

A.18. SN 2020hyj

The first ZTF photometry of SN 2020hyj (ZTF20aavcvrm) was obtained on 2020 April 16 (JD = 2,458,955.92). This first detection was in the g band, with a host-subtracted magnitude of 20.33 ± 0.21 at $\alpha = 16^{h}23^{m}47^{s}.22$, $\delta = 29°58'58.''38$. The discovery was reported to TNS (J. Nordin et al. 2020) on 2020 April 16 with a note saying the latest nondetection by ZTF was two days prior to discovery on 2020 April 14 ($g > 20.32$). The transient was classified as a Type Ic-BL event (A. Dahiwale & C. Fremling 2020d) based on an SEDM spectrum obtained on 2020 April 29. No host galaxy was found upon inspection of archival images through the NASA/IPAC Extragalactic Database. The redshift of $z = 0.055$ was determined through narrow host lines from the SEDM spectrum.

A.19. SN 2020jqm

We refer the reader to A. Corsi et al. (2023) for details about this event.

A.20. SN 2020lao

We refer the reader to S. Anand et al. (2024) for details about this event.

A.21. SN 2020rfr

The first ZTF photometry of SN 2020rfr (ZTF20abrmmah) was obtained on 2020 August 12 (JD = 2,459,073.84). This first detection was in the g band, with a host-subtracted magnitude of 19.67 ± 0.15 at $\alpha = 22^{h}39^{m}49^{s}.30$, $\delta = -06°26'15.''92''$. The discovery was reported to TNS (F. Forster et al. 2020b) with a note saying the latest nondetection by ZTF was four days prior to discovery on 2020 August 8 ($r > 19.96$). The transient was classified as a Type Ic-BL event (A. Dahiwale & C. Fremling 2020e) based on an LRIS spectrum obtained on 2020 September 20. The SN exploded in spiral galaxy WISEA J223949.24-062616.9. The galaxy does not have a well-established redshift, but a redshift of $z = 0.073$ was determined through narrow host lines from the LRIS spectrum.

A.22. SN 2020rph

We refer the reader to S. Anand et al. (2024) for details about this event.

A.23. SN 2020tkx

We refer the reader to S. Anand et al. (2024) for details about this event.

A.24. SN 2020wgz

Our first ZTF photometry of SN 2020wgz (ZTF20achvlbs) was obtained on 2020 October 8 (JD = 2,459,130.99). This first detection was in the r band, with a host-subtracted magnitude of 20.08 ± 0.24 at $\alpha = 08^{h}57^{m}33^{s}.32$, $\delta = 62°34'00.''07$, The discovery was reported to TNS (C. Fremling 2020) with a note saying the latest nondetection by ZTF was one hour prior to the first detection. The SN has no visible galaxy counterpart, and a redshift of $z = 0.1785$ was determined through narrow host lines from a DBSP spectrum obtained on 2020 October 21.

A.25. SN 2020abxl

The first ZTF photometry of SN 2020abxl (ZTF20acvcxkz) was obtained on 2020 December 5 (JD = 2,459,188.79). This first detection was in the r band, with a host-subtracted magnitude of 19.48 ± 0.16 at $\alpha = 05^{h}04^{m}22^{s}.76$, $\delta = -14°02'46.''42$. The discovery was reported to TNS (J. Tonry et al. 2020) by ATLAS on 2020 December 7 ($o = 19.65$) with a note saying the latest

nondetection by ATLAS was one day prior to discovery on 2020 December 6 ($o > 19.33$). The transient was classified as a Type Ic-BL event (J. P. Anderson et al. 2020) based on a spectrum obtained by the EFOSC2-NTT on the ESO New Technology Telescope on 2020 December 11. The SN exploded in spiral galaxy SDSS J223949.25-062616.3. The galaxy does not have a well-established redshift, but a redshift of $z = 0.0815$ was determined through narrow host lines from the NTT spectrum.

A.26. SN 2020abxc

Our first ZTF photometry of SN 2020abxc (ZTF20acvmzfv) was obtained on 2020 December 7 (JD = 2,459,190.65). This first detection was in the r band, with a host-subtracted magnitude of 19.22 ± 0.09 at $\alpha = 01^{h}00^{m}34^{s}.04$, $\delta = -08°07'00.''67$. The discovery was reported to TNS (F. Forster et al. 2020c) with a note saying the latest nondetection by ZTF was two days prior to discovery on 2020 December 5 ($g > 20.03$). The transient was classified as a Type Ic-BL event (R. Cartier et al. 2020) based on a spectrum obtained by the IMACS instrument on the Walter Baade Magellan 6.5 m telescope on 2020 December 8. The SN exploded in the spiral galaxy WISEA J010033.88-080656.9. The galaxy does not have a well-established redshift, but a redshift of $z = 0.0600$ was determined through narrow host lines from the IMACS spectrum.

A.27. SN 2020adow

Our first ZTF photometry of SN 2020adow (ZTF20adadrhw) was obtained on 2020 December 27 (JD = 2,459,210.7560). This first detection was in the g band, with a host-subtracted magnitude of 15.84 ± 0.03 at $\alpha = 08^{h}33^{m}42^{s}.26$, $\delta = +27°42'43.''8$. The transient was discovered by ASASSN already the day before, on 2020 December 26 (K. Z. Stanek & C. S. Kochanek 2020). The transient was classified as a Type Ic-BL on December 27 (S. Zheltoukhov et al. 2020) from a spectrum obtained with the Liverpool Telescope. The SN exploded in the spiral galaxy KUG 0830+278, with a well-established redshift of $z = 0.0075$.

A.28. SN 2021bmf

We refer the reader to S. Anand et al. (2024) for details about this event.

A.29. SN 2021epp

We refer the reader to A. Corsi et al. (2023) for details about this event.

A.30. SN 2021fop

The first ZTF photometry of SN 2021fop (ZTF21aapecxb) was obtained on 2021 March 17 (JD = 2,459,290.71). This first detection was in the g band, with a host-subtracted magnitude of 18.61 ± 0.05 at $\alpha = 07^{h}46^{m}42^{s}.91$, $\delta = 07°12'38.''70$. The discovery was reported to TNS (J. Tonry et al. 2021a) on 2021 March 15 by ATLAS ($o = 18.63$) with a note saying the latest nondetection by ATLAS was eight days prior to discovery on 2021 March 7 ($o > 19.76$). The transient was classified as a Type Ic-BL event (M. A. Tucker 2021a) based on a spectrum obtained by the SNIFS instrument on the UH 88 inch telescope on 2021 March 20. The SN exploded in the spiral galaxy WISEA J074642.81+071238.0. The galaxy does not have a well-established redshift, but a redshift of $z = 0.077$ was determined through narrow host lines from a spectrum on 2021 March 18 obtained by the SPRAT instrument aboard the Liverpool Telescope.

A.31. SN 2021hyz

We refer the reader to A. Corsi et al. (2023) for details about this event.

A.32. SN 2021ktv

The first ZTF photometry of SN 2021ktv (ZTF21aaxxihx) was obtained on 2021 May 1 (JD = 2,459,335.69). This first detection was in the r band, with a host-subtracted magnitude of 19.38 ± 0.13 at $\alpha = 11^{h}03^{m}03^{s}.89$, $\delta = 08°51'39.''75$. The discovery was reported to TNS (J. Tonry et al. 2021b) on the same day by ATLAS ($o = 19.50$) with a note saying the latest nondetection by ATLAS was two days prior to discovery on 2021 April 30 ($o > 19.4$). The transient was classified as a Type Ic-BL event (M. A. Tucker 2021b) based on a spectrum obtained by the SNIFS instrument on the UH 88 inch telescope on 2021 May 19. The SN exploded in galaxy WISEA J110303.81+085140.9. The galaxy does not have a well-established redshift, but a redshift of $z = 0.07$ was determined through narrow host lines from a spectrum taken by DBSP on 2021 June 4.

A.33. SN 2021ncn

The first ZTF photometry of SN 2021ncn (ZTF21abchjer) was obtained on 2021 May 23 (JD = 2,459,357.97). This first detection was in the r band, with a host-subtracted magnitude of 18.58 ± 0.06 at $\alpha = 22^{h}36^{m}32^{s}.93$, $\delta = 25°45'40.''58$. The discovery was reported to TNS (F. Forster et al. 2021) with a note saying the latest nondetection by ZTF was three days prior to discovery on 2021 May 20 ($g > 19.64$). The transient was classified as a Type Ic-BL event (A. Dahiwale & C. Fremling 2021) based on a spectrum obtained by the SEDM on 2021 May 30. The SN exploded in the outskirts of spiral galaxy IC 5233, with a well-established redshift of $z = 0.0246$.

A.34. SN 2021qjv

The first ZTF photometry of SN 2021qjv (ZTF20abcjdwu) was obtained on 2021 June 18 (JD = 2,459,383.72). This first detection was in the r band, with a host-subtracted magnitude of 19.38 ± 0.18 at $\alpha = 15^{h}10^{m}47^{s}.04$, $\delta = 49°12'18.''14$. The discovery was reported to TNS (K. De 2021) two days earlier on 2021 June 16 ($g = 19.67$) with a note saying the latest nondetection by ZTF was two days prior to discovery on 2021 May 20 ($r > 20.57$). The transient was classified as a Type Ic-BL event (M. Chu et al. 2021) based on a spectrum obtained by LRIS on 2021 July 9. Two galaxies, WISEA J151047.04+491218.1 and SDSS J151046.89+491215.4 are spatially consistent with the location of the SN, both with a redshift of $z = 0.0383$.

A.35. SN 2021too

We refer the reader to S. Anand et al. (2024) for details about this event.

A.36. SN 2021ywf

We refer the reader to S. Anand et al. (2024) for details about this event.

Appendix B
Spectral Sequences

Figures 20–34 show the spectra for every event in our sample. Spectra are all shown at their rest wavelengths, and fluxes have been normalized to the median of the spectrum. The rest-frame phase of the spectrum with respect to the *r*-band peak is also shown to the right of each individual spectrum. We show a log of the spectroscopic observations in Table 6.

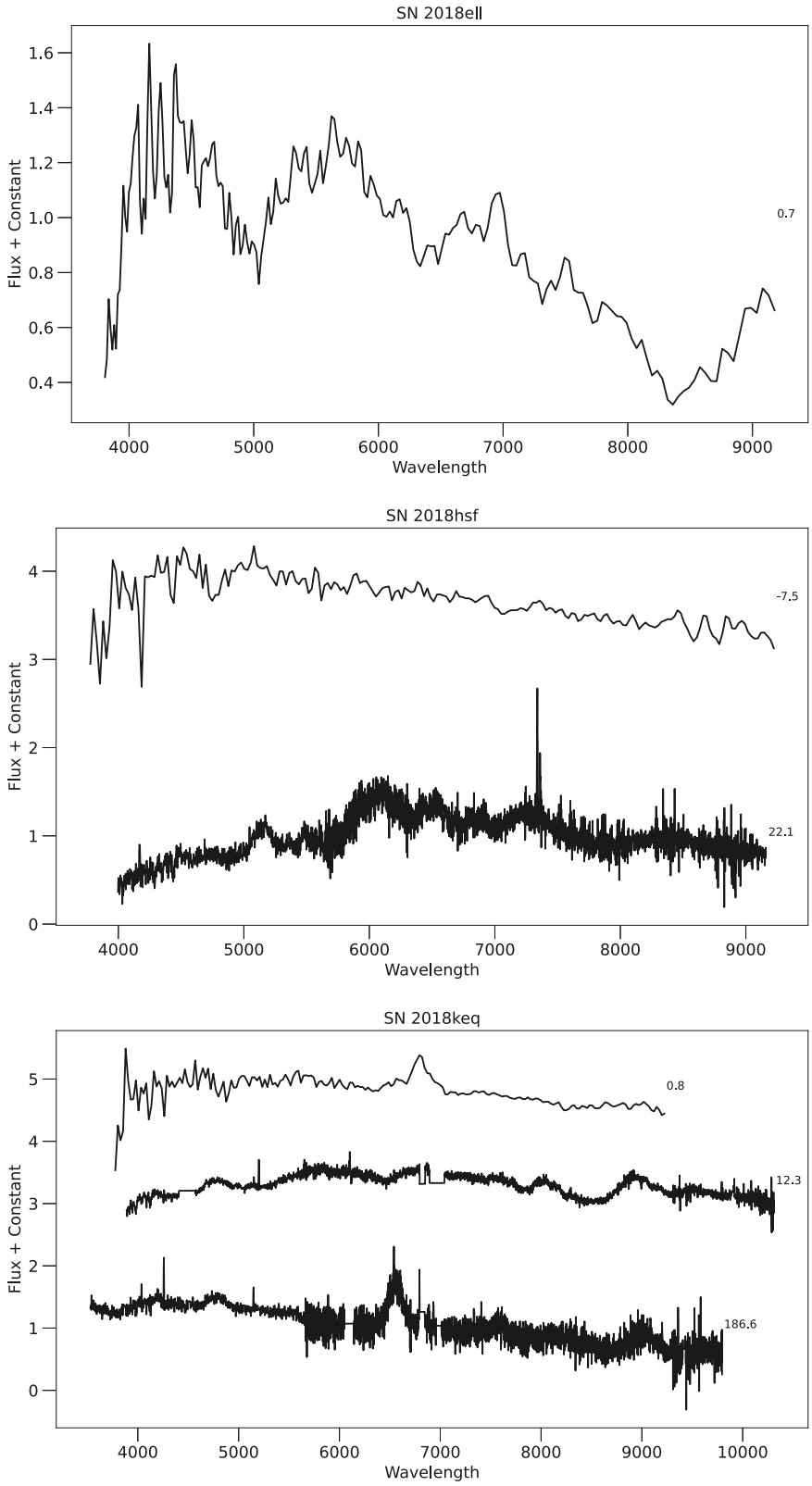

Figure 20. Spectral sequences of SN 2018ell, SN 2018hsf, and SN 2018keq. The phases next to each spectrum are the rest-frame days since the maximum *r*-band flux from the GP processing. The spectra for the rest of the events except for those presented in single-object works (SN 2018bvw, SN 2018gep, and SN 2020bvc) are presented in a similar format below.

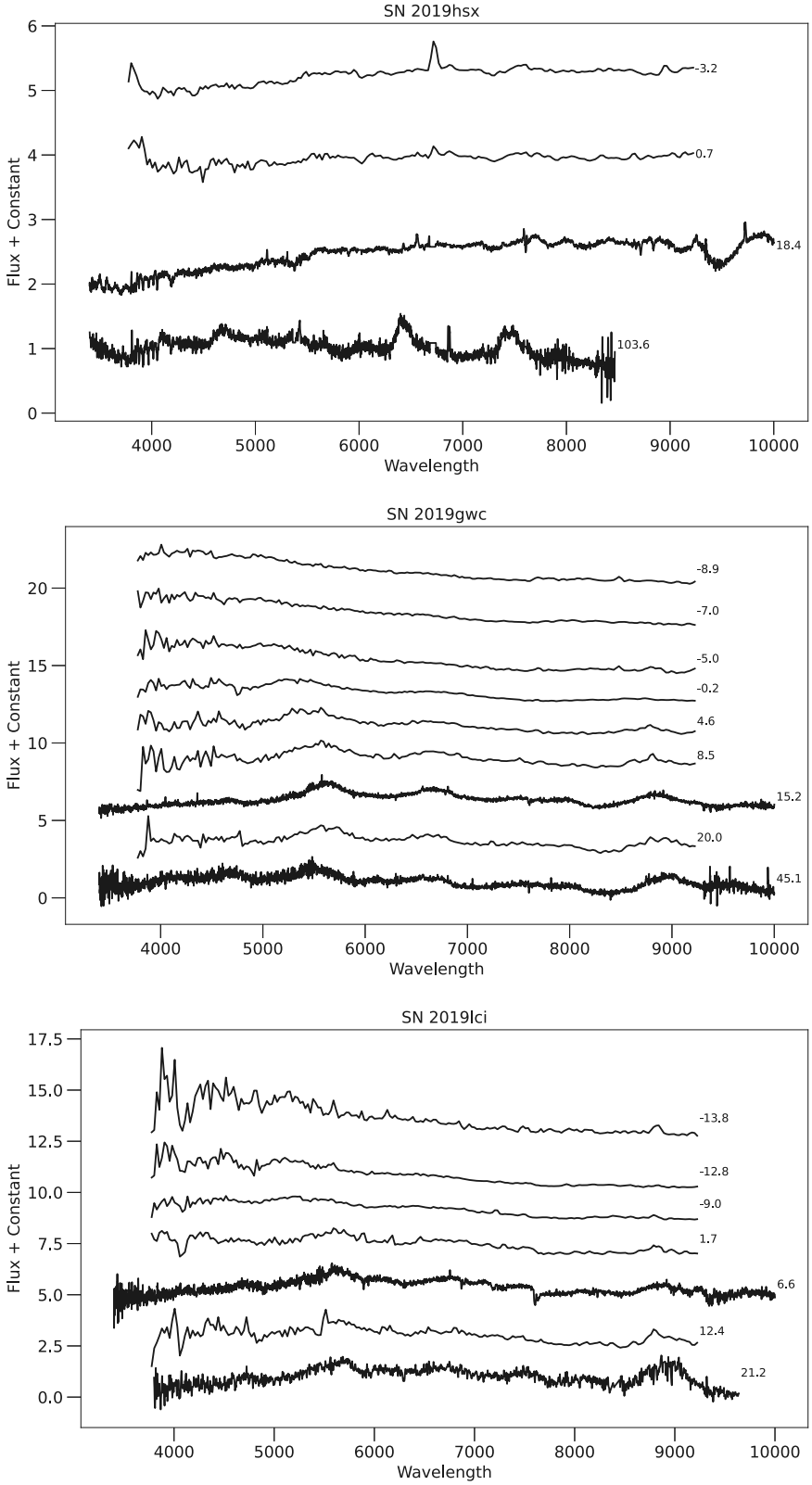

Figure 21. Spectral sequences of SN 2019hsx, SN 2019gwc, and SN 2019lci.

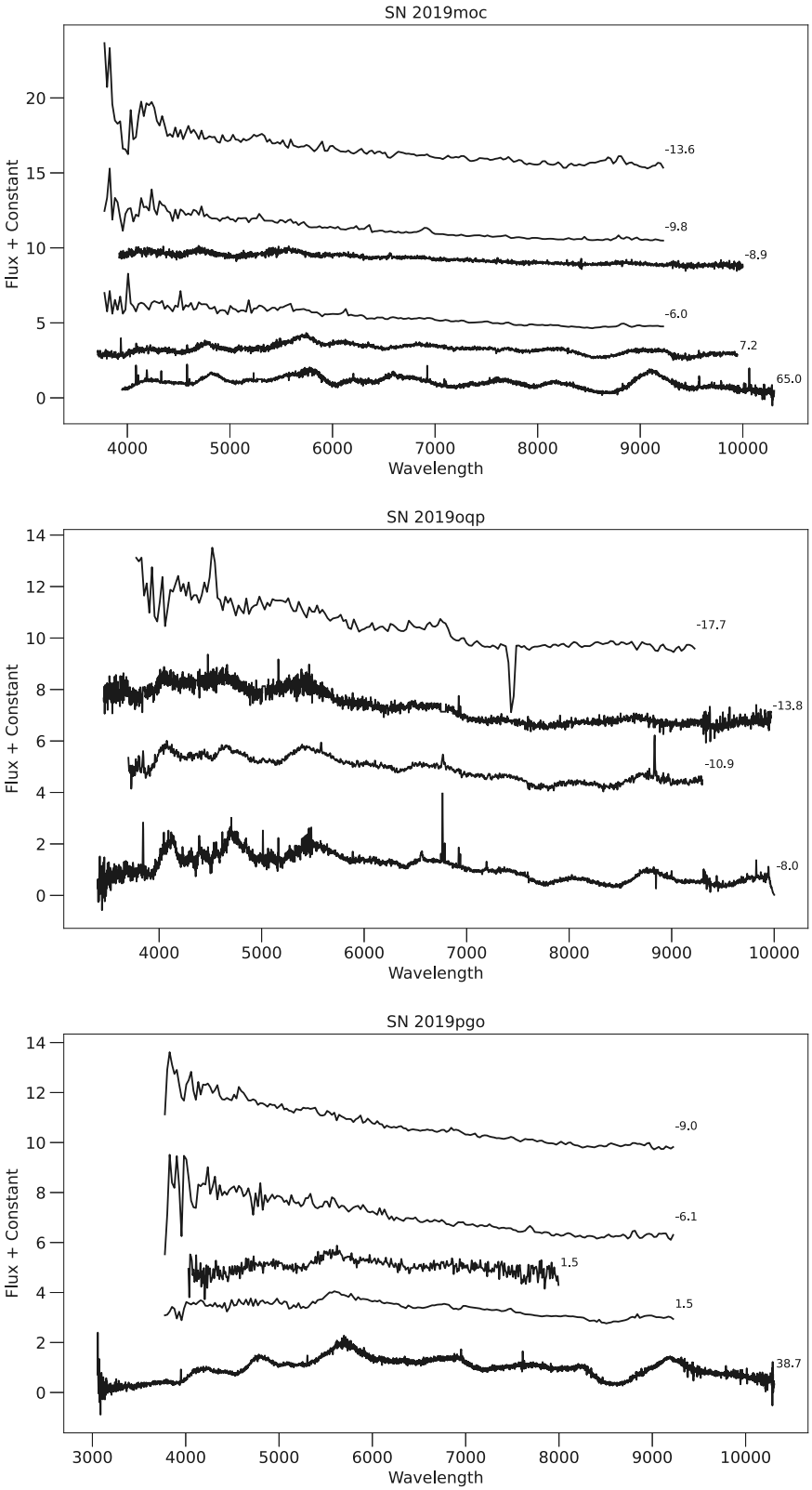

Figure 22. Spectral sequences of SN 2019moc, SN 2019oqp, and SN 2019pgo.

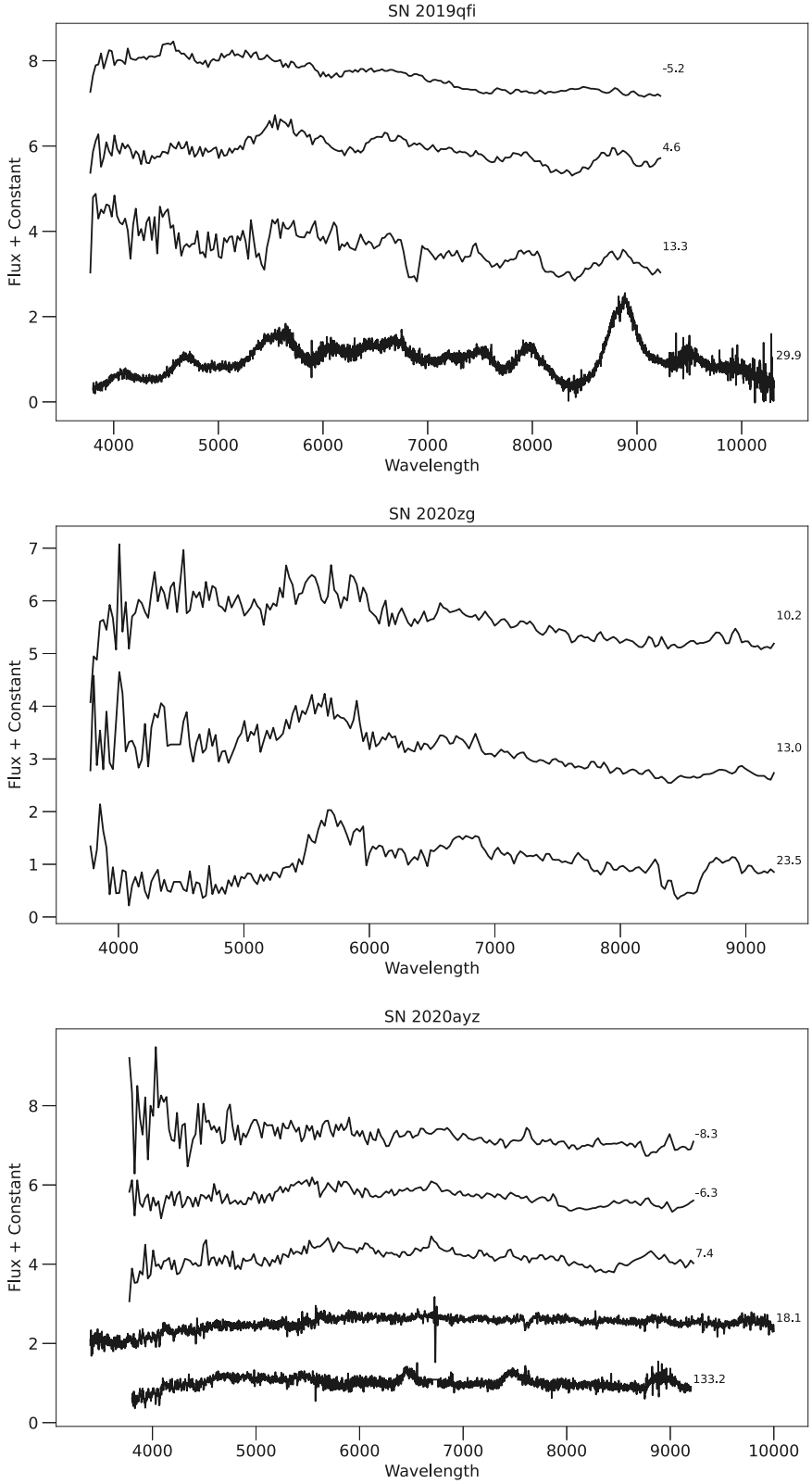

Figure 23. Spectral sequences of SN 2019qfi, SN 2020zg, and SN 2020ayz.

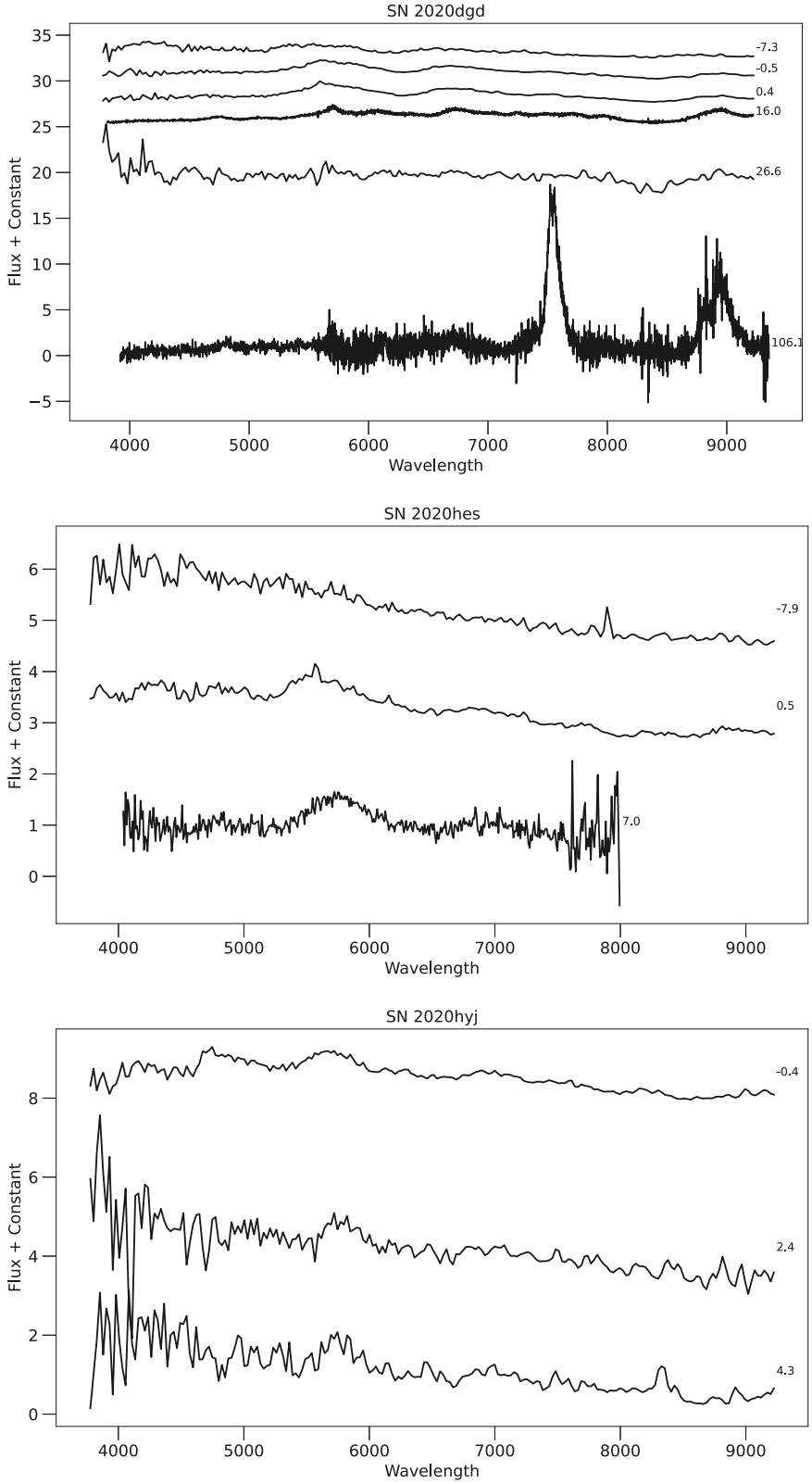

Figure 24. Spectral sequences of SN 2020dgd, SN 2020hes, and SN 2020hyj.

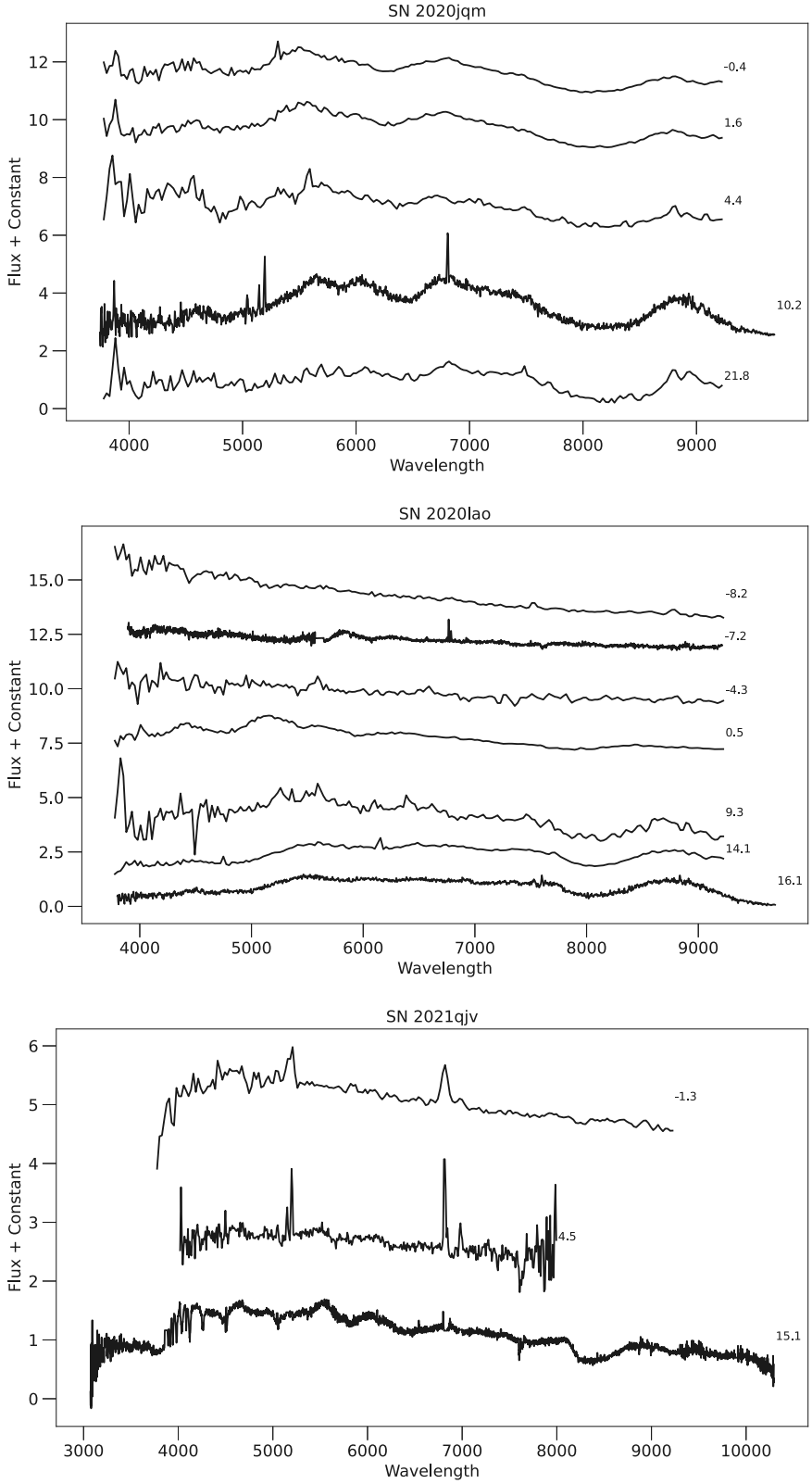

Figure 25. Spectral sequences of SN 2020jqm, SN 2020lao, and SN 2021qjv.

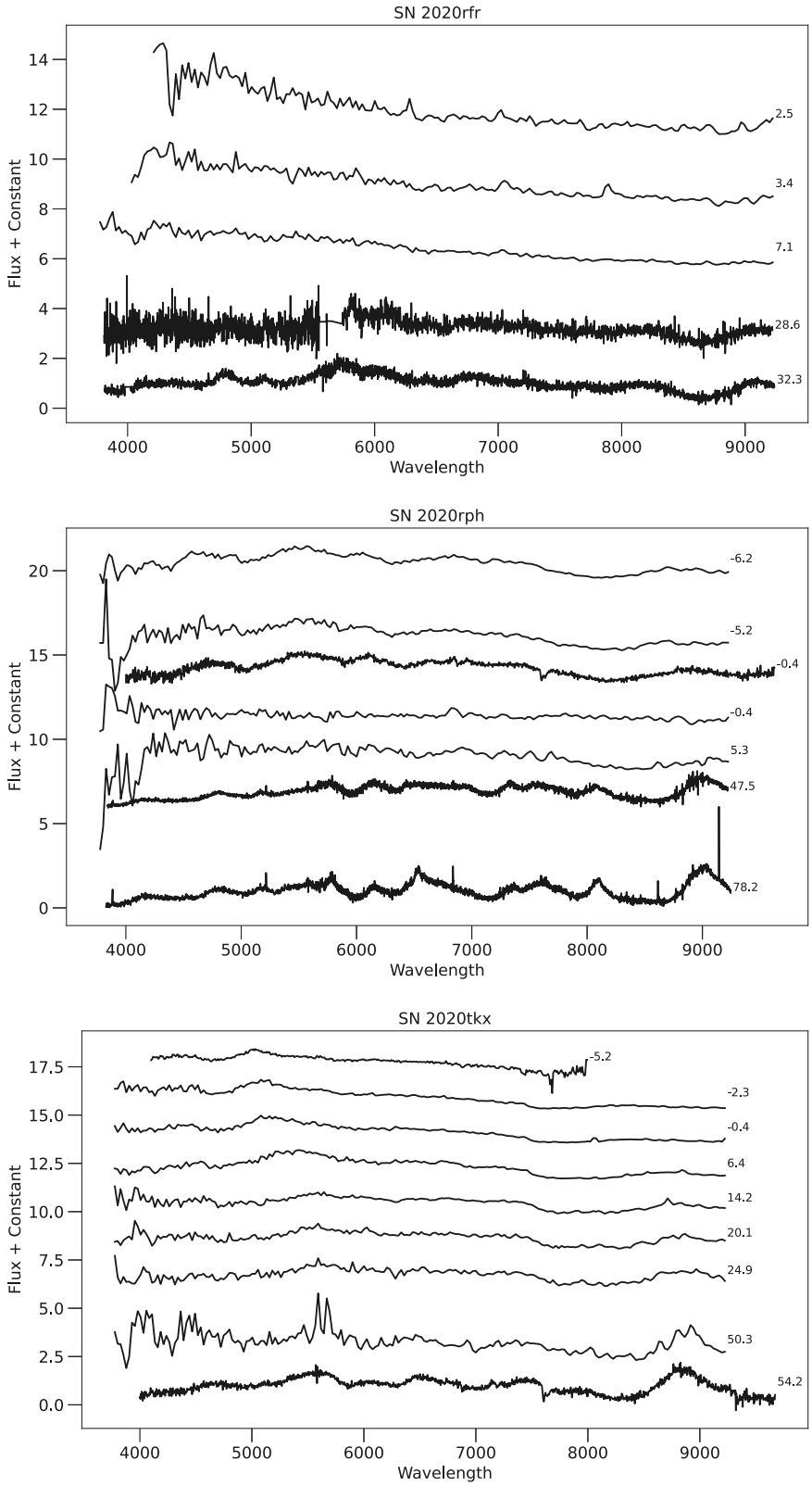

Figure 26. Spectral sequences of SN 2020rfr, SN 2020rph, and SN 2020tkx.

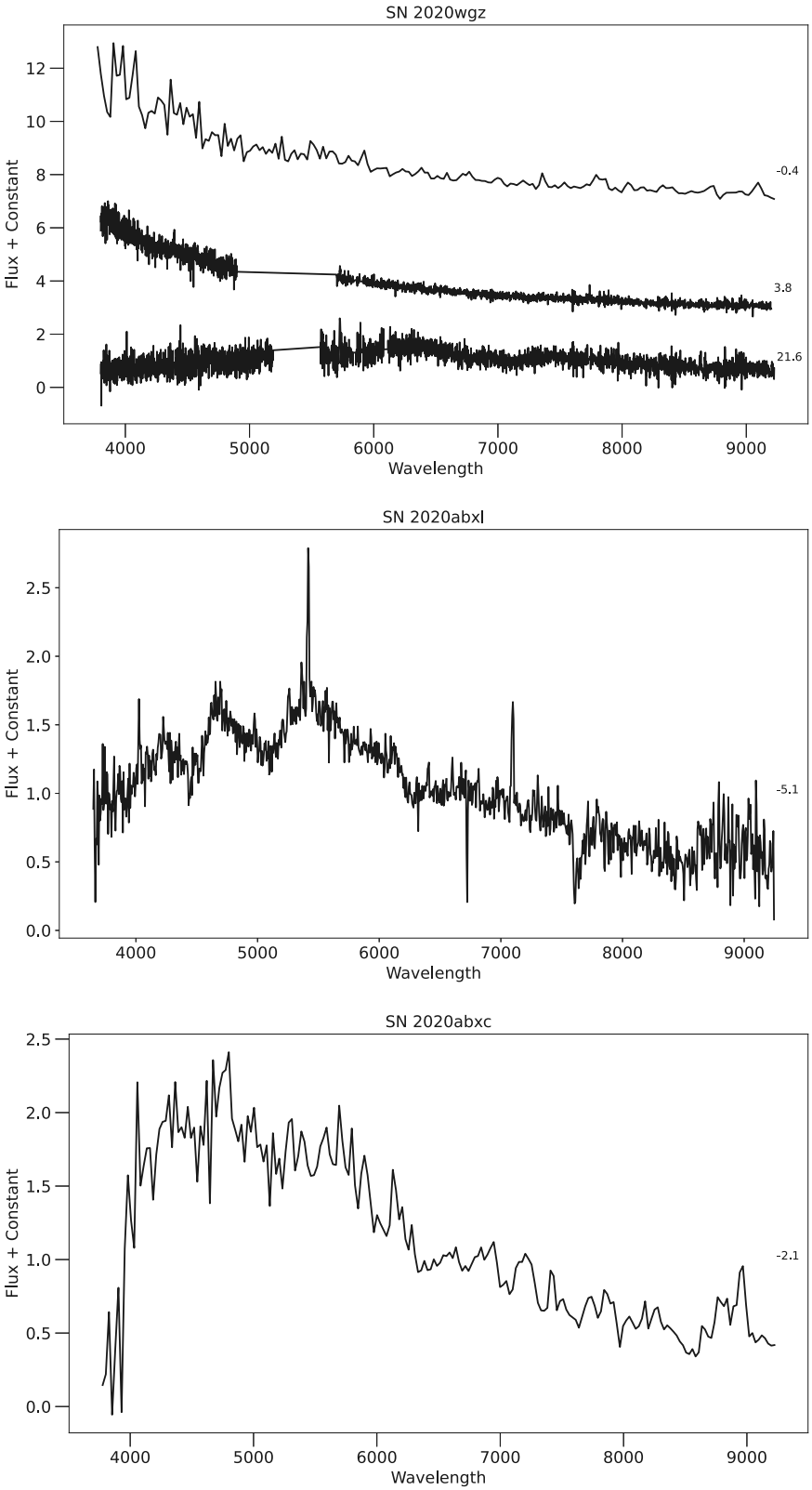

Figure 27. Spectral sequences of SN 2020wgz, SN 2020abxl, and SN 2020abxc.

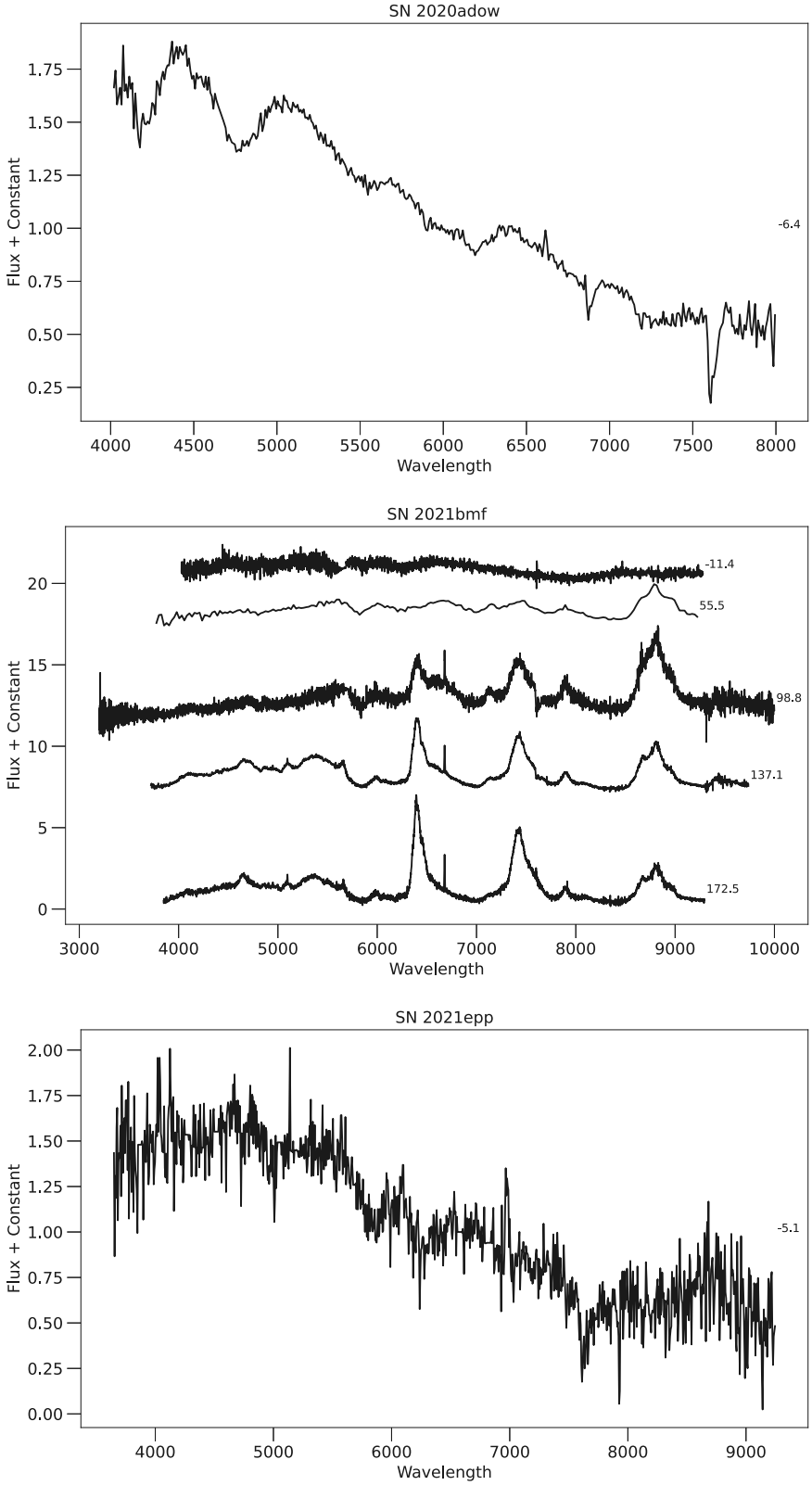

Figure 28. Spectral sequences of SN 2020adow, SN 2021bmf, and SN 2021epp.

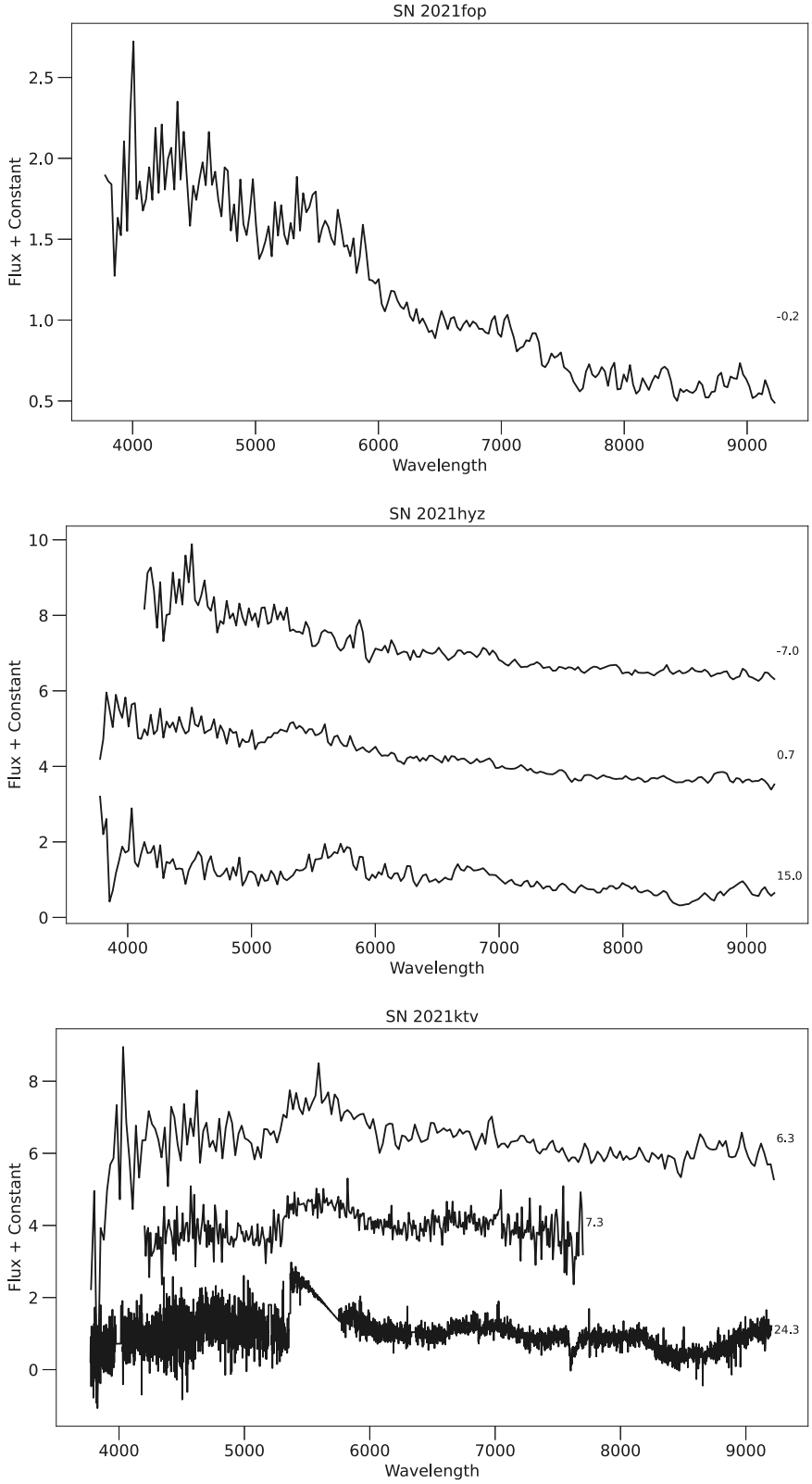

Figure 29. Spectral sequences of SN 2021fop, SN 2021hyz, and SN 2021ktv.

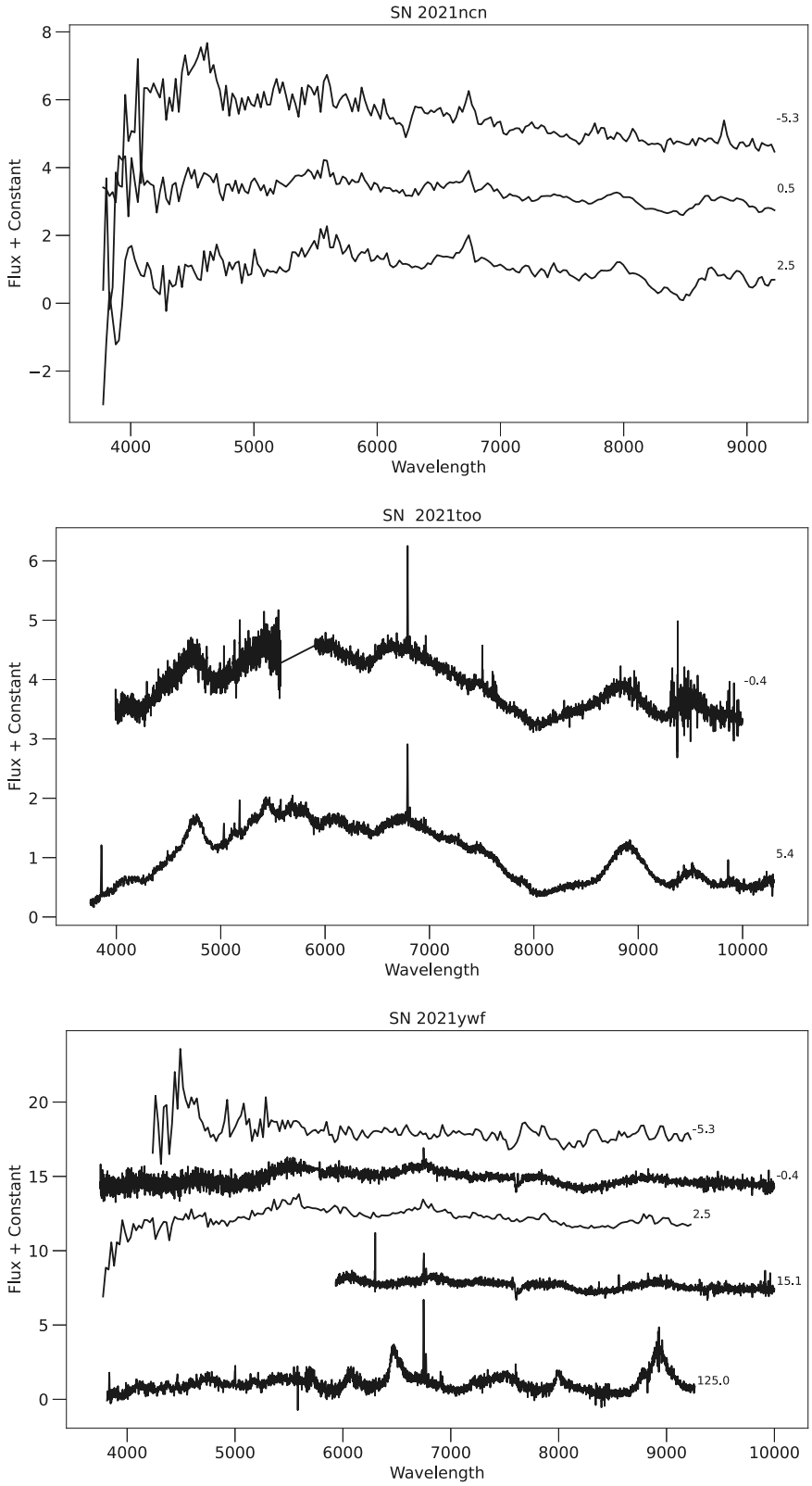

Figure 30. Spectral sequences of SN 2021ncn, SN 2021too, and SN 2021ywf.

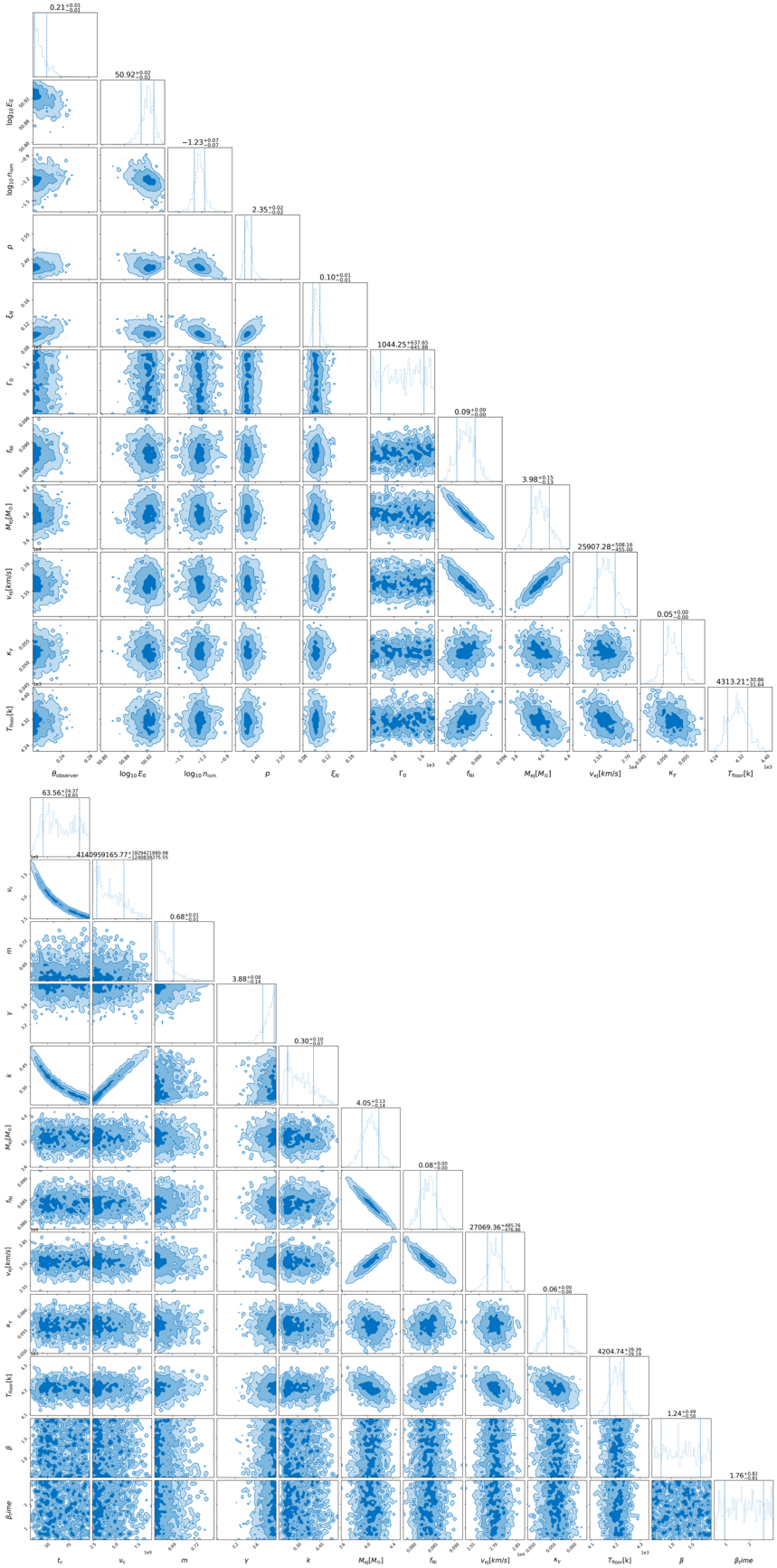

Figure 31. `Redback` modeling results for SN 2020tkx, with the `arnett + tophat` model above and the Radio SSA model below.

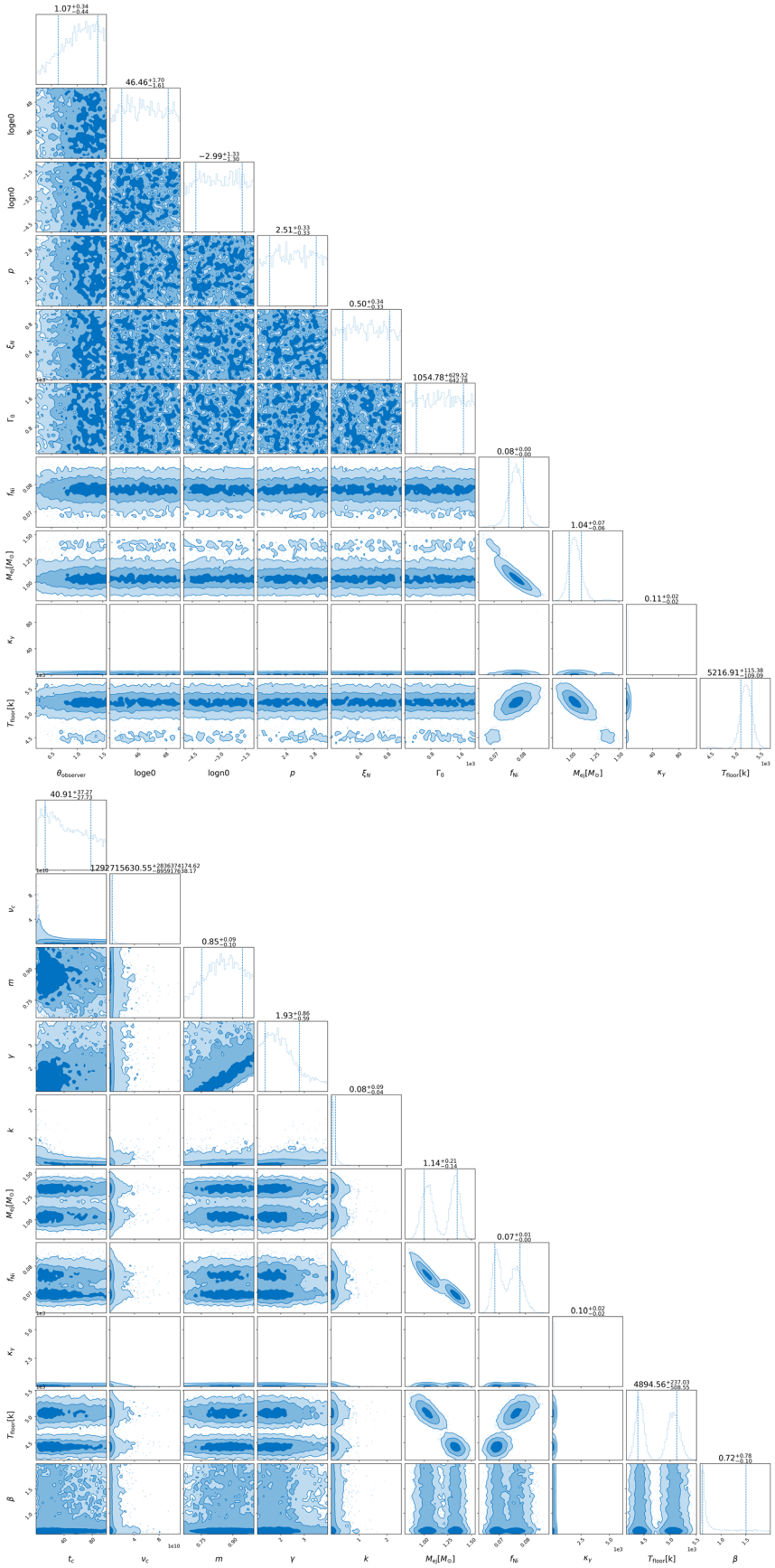

Figure 32. `Redback` modeling results for SN 2021ywf, with the `arnett + tophat` model above and the Radio SSA model below.

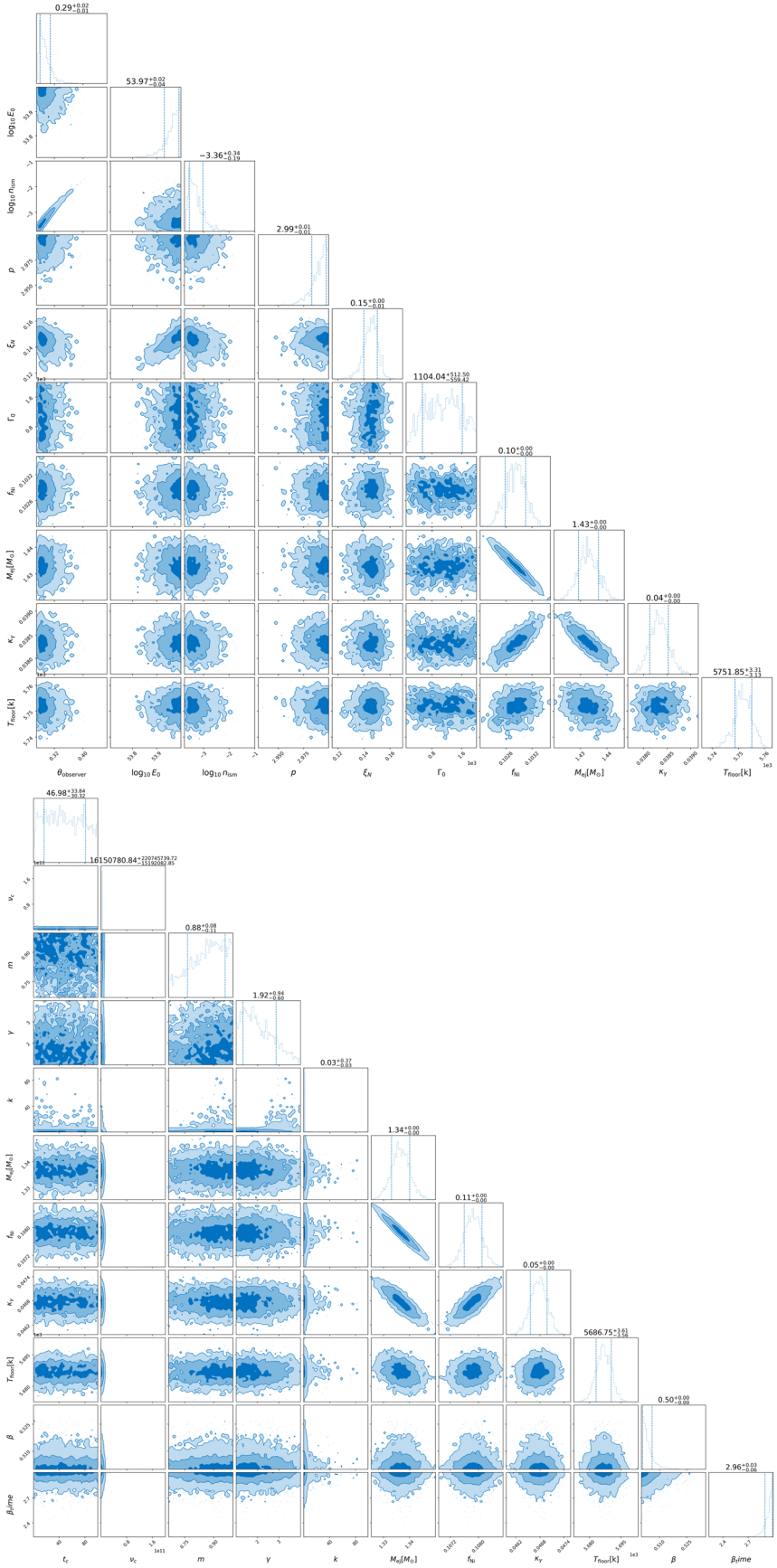

Figure 33. `Redback` modeling results for SN 2020adow, with the `arnett + tophat` model above and the Radio SSA model below.

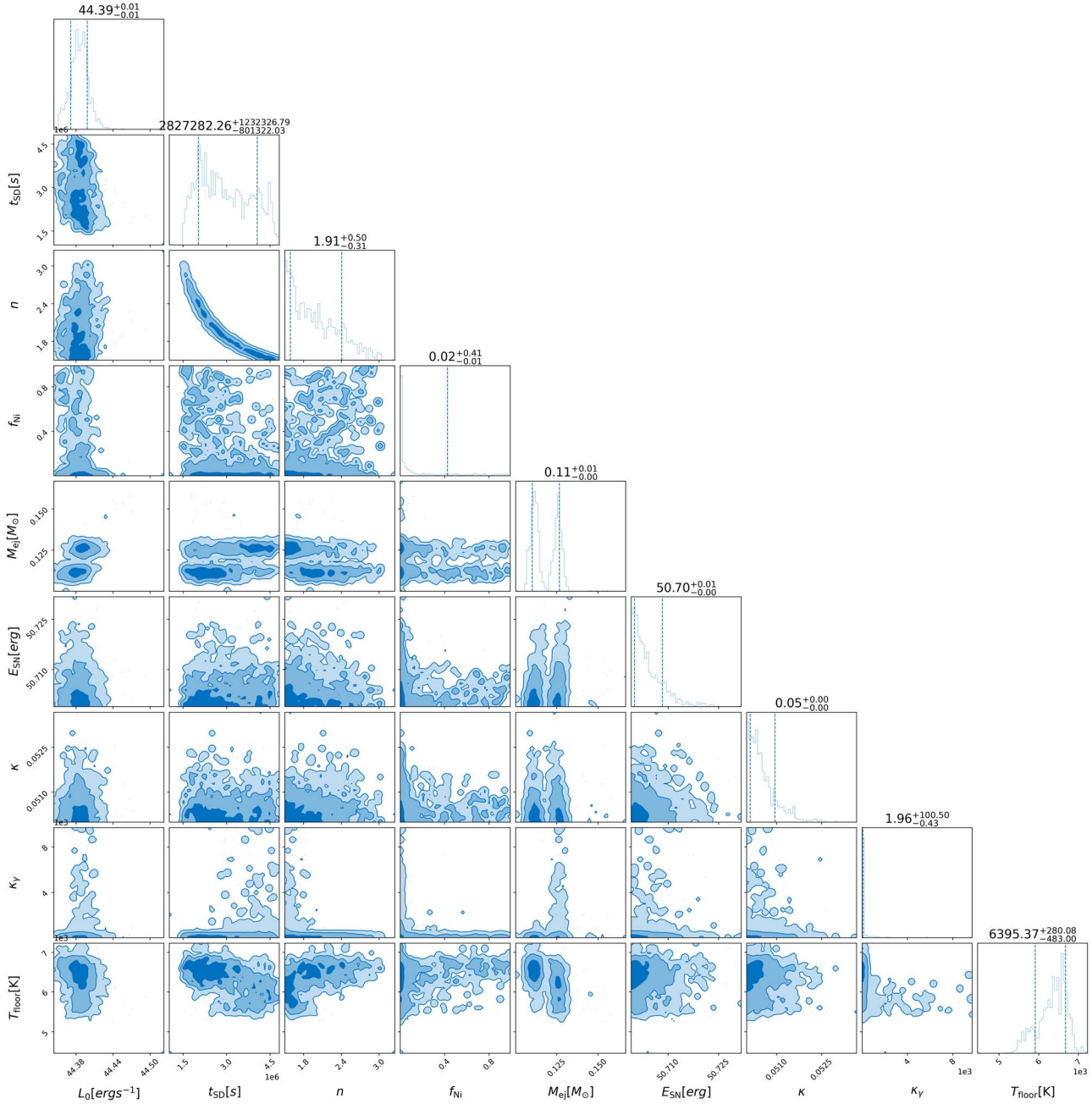

Figure 34. `Redback` modeling results for SN 2020wgz, for the magnetar- and nickel-powered model.

Table 6
Spectral Log of Observations

ZTF name	SN Name	Spectrum Phase	Instrument
ZTF18abhhnnv	SN 2018ell	0.7	SEDM
ZTF18acbvpzj	SN 2018hsf	−7.5	SEDM
		22.1	LRIS
ZTF18acxgoki	SN 2018keq	0.8	SEDM
		12.3	LRIS
		186.6	LRIS
ZTF19aawqcgy	SN 2019hsx	−3.2	SEDM
		0.7	SEDM
		18.4	DBSP
		103.6	LRIS
ZTF19aaxfcpq	SN 2019gwc	−8.9	SEDM
		−7.0	SEDM
		−5.0	SEDM
		−0.2	SEDM
		4.6	SEDM
		8.5	SEDM
		15.2	DBSP
		20.0	SEDM
		45.1	DBSP
ZTF19abfsxpw	SN 2019lci	−13.8	SEDM
		−12.8	SEDM
		−9.0	SEDM
		1.7	SEDM
		6.6	DBSP
		12.4	SEDM
		21.2	NOT
ZTF19ablesob	SN 2019moc	−13.6	SEDM
		−9.8	SEDM
		−8.9	DBSP
		−6.0	SEDM
		7.2	DBSP
		65.0	LRIS
ZTF19abqshry	SN 2019oqp	−17.7	SEDM
		−13.8	DBSP
		−10.9	NOT
		−8.0	DBSP
ZTF19abupned	SN 2019pgo	−9.0	SEDM
		−6.1	SEDM
		1.5	SPRAT
		1.5	SEDM
		38.7	LRIS
ZTF19abzwaen	SN 2019qfi	−5.2	SEDM
		4.6	SEDM
		13.3	SEDM
		29.9	LRIS
ZTF20aafmdzj	SN 2020zg	10.2	SEDM
		13.0	SEDM
		23.5	SEDM
ZTF20aaiqiti	SN 2020ayz	−8.3	SEDM
		−6.3	SEDM
		7.4	SEDM
		18.1	DBSP
		133.2	LRIS
ZTF20aapcbmc	SN 2020dgd	−7.3	SEDM
		−0.5	SEDM
		0.4	SEDM
		16.0	LRIS
		28.6	SEDM
		106.1	LRIS
ZTF20aaurexl	SN 2020hes	−7.9	SEDM
		0.5	SEDM
		7.0	SPRAT
ZTF20aavcvrm	SN 2020hyj	−0.4	SEDM
		2.4	SEDM
		4.3	SEDM
ZTF20aazkjfv	SN 2020jqm	−0.4	SEDM
		1.6	SEDM
		4.4	SEDM
		10.2	NOT
		21.8	SEDM
ZTF20abbplei	SN 2020lao	−8.2	SEDM
		−7.2	DBSP
		−4.3	SEDM
		0.5	SEDM
		9.3	SEDM
		14.1	SEDM
		16.1	SPRAT
ZTF20abcjdwu	SN 2021qjv	−1.3	SEDM
		4.5	SPRAT
		15.1	LRIS
ZTF20abrmmah	SN 2020rfr	2.5	SEDM
		3.4	SEDM
		7.1	SEDM
		28.6	DBSP
		32.3	LRIS
ZTF20abswdbg	SN 2020rph	−6.2	SEDM
		−5.2	SEDM
		−0.4	NOT
		−0.4	SEDM
		5.3	SEDM
		47.5	LRIS
		78.2	LRIS
ZTF20abzoeiw	SN 2020tkx	−5.2	SPRAT
		−2.3	SEDM
		−0.4	SEDM
		6.4	SEDM
		14.2	SEDM
		20.1	SEDM
		24.9	SEDM
		50.3	SEDM
		54.2	SEDM
ZTF20achvlbs	SN 2020wgz	−0.4	SEDM
		3.8	DBSP
		21.6	DBSP
ZTF20acvcxkz	SN 2020abxl	−5.1	ePESSTO+
ZTF20acvmzfv	SN 2020abxc	−2.1	SEDM
ZTF20adadrhw	SN 2020adow	−6.4	SPRAT
ZTF21aagtpro	SN 2021bmf	−11.4	P200
		55.5	SEDM
		96.8	P200
		137.1	LRIS
		172.5	LRIS
ZTF21aaocrlm	SN 2021epp	−5.1	ePESSTO+
ZTF21aapecxb	SN 2021fop	−0.2	SEDM
ZTF21aartgiv	SN 2021hyz	−7.0	SEDM
		0.7	SEDM
		15.0	SEDM
ZTF21aaxxihx	SN 2021ktv	6.3	SEDM
		7.3	SPRAT
		23.3	DBSP
ZTF21abchjer	SN 2021ncn	−5.3	SEDM
		0.5	SEDM
		2.5	SEDM
ZTF21abmjgwf	SN 2021too	−0.4	DBSP
		5.4	LRIS
ZTF21acbnfos	SN 2021ywf	−5.3	SEDM
		−0.4	DBSP
		2.5	DBSP
		15.1	DBSP
		125.0	LRIS

Note. Spectrum phase is in rest frame with respect to *r*-band maximum.

Appendix C
Multiwavelength Modeling

We use the open-source electromagnetic transient Bayesian fitting software package `redback` (N. Sarin et al. 2023) to perform multiwavelength modeling of three events to determine if it is possible that these events had an associated

relativistic jet, through modeling the optical, radio, and X-ray data simultaneously in flux density space. We use the `arnett + tophat` model in `redback`, which utilizes a combination of radioactive decay of nickel from W. D. Arnett (1982), along with a synchrotron component from an accompanying top-hat jet generated from the software package `afterglowpy` (G. Ryan et al. 2020), to model SN emission with an off-axis accompanying relativistic jet with a jet half-opening angle of 0.1 radian.

We compare the Bayesian evidences for this model to those of the synchrotron self-absorption (SSA) model for radio SNe (Equation (4) from R. A. Chevalier 1998) to compute a Bayes factor and determine which model can better explain the multiwavelength observations. We report the free fitting parameters for each of the models and the priors used in Tables 7 and 8. Below we report the results for each of the events. Because there are only a few radio and X-ray detections/non-detections available for each event, we note that these results must be taken with a grain of salt, and therefore present them in the Appendix.

C.0.1. SN 2020tkx

SN 2020tkx has two radio detections and one X-ray non-detection reported in A. Corsi et al. (2023). Because $v_{\rm ph}$ for this event was measured from a spectrum 53 days after peak, we allow it to vary as a free parameter with uniform priors. Furthermore, the radio LC shown in Figure 11 in A. Corsi et al. (2023) shows a rise in time, and there are no significant constraints that can be put on the jet's energy or the interstellar medium (ISM) number density, so we allow both those parameters to vary with uniform priors in logarithmic space. The corner plots for the fitting are shown in the Appendix, and we find that the `Arnett + tophat` model is favored with a Bayes factor of $10^{23.0}$.

C.0.2. SN 2020adow

SN 2020adow has two radio detections and one X-ray detection, and was not reported in A. Corsi et al. (2023). There were two radio measurements obtained, at 5.3 and 16.3 days after explosion, with flux densities of 28.5 ± 7.1 and 17.1 ± 7.6 μJy (A. Corsi et al. 2021). The X-ray measurement was obtained 42 days after explosion, with a 0.3–10 keV flux of $4.9^{+2.8}_{-2.1} \times 10^{-14}$ erg cm^{-2} s^{-1}. We convert the 0.3–10 keV flux to a flux density at 5 keV for the fitting, through assuming a power-law spectrum of photon index $\Gamma = 2$. We constrain $v_{\rm ph}$ as a prior to the value obtained in Section 5 (19,500 km s^{-1}), which utilized a spectrum taken seven days before peak. We have no constraints on the jet energy or ISM number density for this object from previous works, so we allow both those parameters to vary with uniform priors in logarithmic space. The corner plots for the fitting are shown in the Appendix, and we find that the Radio + SSA model is favored qualitatively, though a conclusive Bayes factor was not able to be found for this event.

C.0.3. SN 2021ywf

SN 2021ywf has two radio detections and one X-ray detection reported in A. Corsi et al. (2023). We convert the 0.3–10 keV flux reported to a flux density at 5 keV for the fitting, through assuming a power-law spectrum of photon index $\Gamma = 2$. We constrain $v_{\rm ph}$ as a prior to the value obtained in Section 5 (12,000 km s^{-1}), which utilized a spectrum taken 0.5 days after peak. A. Corsi et al. (2023) also was able to rule out top-hat jets with energies greater than 10^{49} erg and ISM number densities (n_0) greater than 0.1 cm^{-3} for this event, so we utilize these priors in the fitting procedure as well. The corner plots for the fitting are shown in the Appendix, and we find that the Radio SSA model is favored with a Bayes factor of $K_{\rm Bayes} = 10^{28.5}$.

Table 7
Model Parameters, Description, and Priors used for the `arnett + tophat` Model in the `redback` Fitting

Parameters	Description	Prior Boundaries
z	Redshift	Set to values from Table 1
$v_{\rm ph}$	Peak photospheric expansion velocity	Set to values from Table 5
$f_{\rm Ni}$	Nickel fraction	[0.001, 1] (in $\rm Log_{10}$ space)
$M_{\rm ej}$	Ejecta mass	[0.0001, 100] $M_\odot$ (in $\rm Log_{10}$ space)
A_v	Milky Way extinction	0 mag
κ	Optical opacity	0.07 cm^2 g^{-1}
κ_γ	Gamma-ray opacity	[0.0001, 10,000] cm^2 g^{-1} (in $\rm Log_{10}$ space)
$T_{\rm floor}$	Minimum temperature reached in early explosion	[1000, 100,000] K (in $\rm Log_{10}$ space)
$\theta_{\rm observer}$	Observing angle of jet	Sine[0.2, 1.57]
$\theta_{\rm core}$	Jet opening angle	0.1
ϵ_e	$\rm Log_{10}$ fraction of thermal energy to electrons	0.1
ϵ_b	$\rm Log_{10}$ fraction of thermal energy to magnetic field	0.1
E_0	$\rm Log_{10}$ on axis isotropic equivalent energy	See individual event subsections
n_0	$\rm Log_{10}$ ISM number density	See individual event subsections
p	Electron distribution power-law index	[2, 3]
ξ_N	Fraction of electrons that get accelerated	[0,1]
Γ_0	Initial Lorentz Factor	[100, 2000]

Table 8
Model Parameters, Description, and Priors used for the Radio SSA Model in the `redback` Fitting

Parameters	Description	Prior Boundaries
z	Redshift	Set to values from Table 1
$v_{\rm ph}$	Peak photospheric expansion velocity	Set to values from Table 5
$f_{\rm Ni}$	Nickel fraction	[0.001, 1] (in $\rm Log_{10}$ space)
$M_{\rm ej}$	Ejecta mass	[0.0001, 100] $M_\odot$ (in $\rm Log_{10}$ space)
A_v	Milky Way extinction	0 mag
κ	Optical opacity	0.07 $\rm cm^2\ g^{-1}$
κ_γ	Gamma-ray opacity	[0.0001, 10,000] $\rm cm^2\ g^{-1}$ (in $\rm Log_{10}$ space)
$T_{\rm floor}$	Minimum temperature reached in early explosion	[1000, 100,000] K (in $\rm Log_{10}$ space)
t_c	Time where emission has $\tau_{\rm opt} \sim 1$ at ν_c	[0, 1000] days
ν_c	Characteristic frequency to scale t_c	[10^7, 10^9] Hz (in $\rm Log_{10}$ space)
m	Power-law index of emitting region expansion (R^m)	[$\frac{2}{3}$, 1]
γ	Electron spectral index	[1, 4]
k	Flux-scaling Factor	[0.0001, 100] (in $\rm Log_{10}$ space)
β	Spectral power-law index	[0.5, 2]
$\beta_{\rm time}$	Temporal power-law index	[0.5, 3]

ORCID iDs

Gokul P. Srinivasaragavan https://orcid.org/0000-0002-6428-2700
Sheng Yang https://orcid.org/0000-0002-2898-6532
Shreya Anand https://orcid.org/0000-0003-3768-7515
Jesper Sollerman https://orcid.org/0000-0003-1546-6615
Anna Y. Q. Ho https://orcid.org/0000-0002-9017-3567
Alessandra Corsi https://orcid.org/0000-0001-8104-3536
S. Bradley Cenko https://orcid.org/0000-0003-1673-970X
Daniel Perley https://orcid.org/0000-0001-8472-1996
Steve Schulze https://orcid.org/0000-0001-6797-1889
Nikhil Sarin https://orcid.org/0000-0003-2700-1030
Conor Omand https://orcid.org/0000-0002-9646-8710
Kaustav K. Das https://orcid.org/0000-0001-8372-997X
Christoffer Fremling https://orcid.org/0000-0002-4223-103X
Igor Andreoni https://orcid.org/0000-0002-8977-1498
Rachel Bruch https://orcid.org/0000-0001-8208-2473
Kevin B. Burdge https://orcid.org/0000-0002-7226-836X
Kishalay De https://orcid.org/0000-0002-8989-0542
Avishay Gal-Yam https://orcid.org/0000-0002-3653-5598
Anjasha Gangopadhyay https://orcid.org/0000-0002-3884-5637
Matthew J. Graham https://orcid.org/0000-0002-3168-0139
Jacob E. Jencson https://orcid.org/0000-0001-5754-4007
Viraj Karambelkar https://orcid.org/0000-0003-2758-159X
Mansi M. Kasliwal https://orcid.org/0000-0002-5619-4938
S. R. Kulkarni https://orcid.org/0000-0001-5390-8563
Julia Martikainen https://orcid.org/0000-0003-2211-4001
Yashvi S. Sharma https://orcid.org/0000-0003-4531-1745
Anastasios Tzanidakis https://orcid.org/0000-0003-0484-3331
Lin Yan https://orcid.org/0000-0003-1710-9339
Yuhan Yao https://orcid.org/0000-0001-6747-8509
Eric C. Bellm https://orcid.org/0000-0001-8018-5348
Steven L. Groom https://orcid.org/0000-0001-5668-3507
Frank J. Masci https://orcid.org/0000-0002-8532-9395
Guy Nir https://orcid.org/0000-0002-7501-5579
Josiah Purdum https://orcid.org/0000-0003-1227-3738
Roger Smith https://orcid.org/0000-0001-7062-9726

References

Ambikasaran, S., Foreman-Mackey, D., Greengard, L., Hogg, D. W., & O'Neil, M. 2015, ITPAM, 38, 252
Anand, S., Barnes, J., Yang, S., et al. 2024, ApJ, 962, 68
Anderson, J. P., Pessi, P., Galbany, L., & Irani, I. 2020, TNSCR, 2020-3755, 1
Arcavi, I., Gal-Yam, A., Yaron, O., et al. 2011, The Astrophysical Journal Letters, 742, 7
Arnett, W. D. 1982, ApJ, 253, 785
Barbarino, C., Sollerman, J., Taddia, F., et al. 2021, A&A, 651, A81
Barbary, K., Barclay, T., Biswas, R., et al., 2016 SNCosmo: Python Library for Supernova Cosmology, Astrophysics Source Code Library, ascl:1611.017
Bazin, G., Palanque-Delabrouille, N., Rich, J., et al. 2009, A&A, 499, 653
Bellm, E. C., Kulkarni, S. R., Graham, M. J., et al. 2019, PASP, 131, 018002
Bellm, E. C., & Sesar, B., 2016 pyraf-dbsp: Reduction pipeline for the Palomar Double Beam Spectrograph, Astrophysics Source Code Library, ascl:1602.002
Bennett, C. L., Larson, D., Weiland, J. L., & Hinshaw, G. 2014, ApJ, 794, 135
Berger, E., Kulkarni, S. R., & Chevalier, R. A. 2002, ApJL, 577, L5
Blagorodnova, N., Neill, J. D., Walters, R., et al. 2018, PASP, 130, 035003
Blanchard, P. K., Nicholl, M., Berger, E., et al. 2019, ApJ, 872, 90
Blanchard, P. K., Villar, V. A., Chornock, R., et al. 2023, Nature Astronomy, 8, 774
Burns, C. R., Stritzinger, M., Phillips, M. M., et al. 2011, AJ, 141, 19
Burrows, D. N., Hill, J. E., Nousek, J. A., et al. 2005, SSRv, 120, 165
Cano, Z. 2013, MNRAS, 434, 1098
Cano, Z. 2014, ApJ, 794, 121
Cano, Z., Wang, S.-Q., Dai, Z.-G., & Wu, X.-F. 2017, AdAst, 2017, 8929054
Cardelli, J. A., Clayton, G. C., & Mathis, J. S. 1989, ApJ, 345, 245
Cartier, R., Contreras, C., Pasten, A., & Fuentes, C. 2020, TNSCR, 2020-3729, 1
Chevalier, R. A. 1998, ApJ, 499, 810
Chu, M., Dahiwale, A., & Fremling, C. 2021, TNSCR, 2021-2534, 1
Chugai, N. N. 2000, AstL, 26, 797
Clocchiatti, A., Suntzeff, N. B., Covarrubias, R., & Candia, P. 2011, AJ, 141, 163
Conti, P. S., & Walborn, N. R. 1976, ApJ, 207, 502
Corsi, A., Gal-Yam, A., Kulkarni, S. R., et al. 2016, ApJ, 830, 42
Corsi, A., Ho, A., Kulkarni, S., & Perley, D. 2021, TNSAN, 47, 1
Corsi, A., Ho, A. Y. Q., Cenko, S. B., et al. 2023, ApJ, 953, 179
Corsi, A., Ofek, E. O., Gal-Yam, A., et al. 2014, ApJ, 782, 42
Coughlin, M. W., Bloom, J. S., Nir, G., et al. 2023, ApJS, 267, 31
Dahiwale, A., & Fremling, C. 2020a, TNSCR, 2020-1667, 1
Dahiwale, A., & Fremling, C. 2020b, TNSCR, 2020-688, 1
Dahiwale, A., & Fremling, C. 2020c, TNSCR, 2020-1130, 1
Dahiwale, A., & Fremling, C. 2020d, TNSCR, 2020-1186, 1
Dahiwale, A., & Fremling, C. 2020e, TNSCR, 2020-2954, 1
Dahiwale, A., & Fremling, C. 2021, TNSCR, 2021-1879, 1
De, K. 2021, TNSTR, 2021-2126, 1
Dekany, R., Smith, R. M., Riddle, R., et al. 2020, PASP, 132, 038001
D'Elia, V., Pian, E., Melandri, A., et al. 2015, A&A, 577, A116
Della Valle, M., Chincarini, G., Panagia, N., et al. 2006, Natur, 444, 1050
Dessart, L., & Hillier, D. J. 2005, A&A, 439, 671
Dessart, L., Hillier, D. J., Waldman, R., Livne, E., & Blondin, S. 2012, MNRAS, 426, L76
Drout, M. R., Soderberg, A. M., Gal-Yam, A., et al. 2011, ApJ, 741, 97
Dugas, A., Fremling, C., & Sharma, Y. 2019, TNSCR, 2019-1215, 1
Eastman, R. G., Schmidt, B. P., & Kirshner, R. 1996, ApJ, 466, 911
Forster, F., Bauer, F. E., Galbany, L., et al. 2020a, TNSTR, 2020-1027, 1
Forster, F., Bauer, F. E., Galbany, L., et al. 2020b, TNSTR, 2020-2457, 1
Forster, F., Bauer, F. E., Pignata, G., et al. 2020c, TNSTR, 2020-3690, 1
Forster, F., Mourao, A., Bauer, F. E., et al. 2021, TNSTR, 2021-1769, 1
Forster, F., Pignata, G., Bauer, F. E., et al. 2020d, TNSTR, 2020-141, 1
Forster, F., Pignata, G., Bauer, F. E., et al. 2020e, TNSTR, 2020-263, 1
Fremling, C. 2018a, TNSTR, 2018-1058, 1
Fremling, C. 2018b, TNSTR, 2018-1674, 1
Fremling, C. 2020a, TNSTR, 2020-3102, 1
Fremling, C., Dahiwale, A., & Dugas, A. 2019a, TNSCR, 2019-1855, 1
Fremling, C., Dahiwale, A., & Sharma, Y. 2019b, TNSCR, 2019-1757, 1

Fremling, C., Dugas, A., & Sharma, Y. 2018, TNSCR,, 2018-1877, 1
Fremling, C., Dugas, A., & Sharma, Y. 2019c, TNSCR, 2019-32, 1
Fremling, C., Miller, A. A., Sharma, Y., et al. 2020, ApJ, 895, 32
Fynbo, J. P. U., Watson, D., Thöne, C. C., et al. 2006, Natur, 444, 1047
Galama, T. J., Vreeswijk, P. M., van Paradijs, J., et al. 1998, Natur, 395, 670
Gal-Yam, A. 2012, Sci, 337, 927
Gal-Yam, A. 2017, in Observational and Physical Classification of Supernovae, ed. A. W. Alsabti & P. Murdin (Springer), 195
Gal-Yam, A., Fox, D. B., Price, P. A., et al. 2006, Natur, 444, 1053
Gehrels, N., Chincarini, G., Giommi, P., et al. 2004, ApJ, 611, 1005
Graham, M. J., Kulkarni, S. R., Bellm, E. C., et al. 2019, PASP, 131, 078001
Greiner, J., Mazzali, P. A., Kann, D. A., et al. 2015, Natur, 523, 189
Hamuy, M., Pinto, P. A., Maza, J., et al. 2001, ApJ, 558, 615
Hjorth, J., Sollerman, J., Møller, P., et al. 2003, Natur, 423, 847
Ho, A. Y. Q., Corsi, A., Cenko, S. B., et al. 2020a, ApJ, 893, 132
Ho, A. Y. Q., Goldstein, D. A., Schulze, S., et al. 2019, ApJ, 887, 169
Ho, A. Y. Q., Kulkarni, S. R., Perley, D. A., et al. 2020b, ApJ, 902, 86
Hu, Y. D., Castro-Tirado, A. J., Kumar, A., et al. 2021, A&A, 646, A50
Iwamoto, K., Mazzali, P. A., Nomoto, K., et al. 1998, Natur, 395, 672
Izzo, L., Auchettl, K., Hjorth, J., et al. 2020, A&A, 639, L11
Kasen, D., & Bildsten, L. 2010, ApJ, 717, 245
Kasliwal, M. M., Cannella, C., Bagdasaryan, A., et al. 2019, PASP, 131, 038003
Kelly, B. C. 2007, ApJ, 665, 1489
Kumar, A., Pandey, S. B., Gupta, R., et al. 2022, NewA, 97, 101889
Leung, S.-C., Fuller, J., & Nomoto, K. 2021, ApJ, 915, 80
Li, L., Zhong, S.-Q., & Dai, Z.-G. 2023, ApJL, 952, L39
Li, X., & Hjorth, J. 2014, arXiv:1407.3506
Liu, Y.-Q., Modjaz, M., Bianco, F. B., & Graur, O. 2016, ApJ, 827, 90
Lyman, J. D., Bersier, D., & James, P. A. 2014, MNRAS, 437, 3848
Lyman, J. D., Bersier, D., James, P. A., et al. 2016, MNRAS, 457, 328
Mahabal, A., Rebbapragada, U., Walters, R., et al. 2019, PASP, 131, 038002
Masci, F. J., Laher, R. R., Rusholme, B., et al. 2019, PASP, 131, 018003
Mazzali, P. A., Deng, J., Maeda, K., et al. 2002, ApJL, 572, L61
Mazzali, P. A., Deng, J., Nomoto, K., et al. 2006a, Natur, 442, 1018
Mazzali, P. A., Deng, J., Pian, E., et al. 2006b, ApJ, 645, 1323
Mazzali, P. A., Deng, J., Tominaga, N., et al. 2003, ApJL, 599, L95
Mazzali, P. A., Iwamoto, K., & Nomoto, K. 2000, ApJ, 545, 407
Melandri, A., Malesani, D. B., Izzo, L., et al. 2019, MNRAS, 490, 5366
Melandri, A., Pian, E., Ferrero, P., et al. 2012, A&A, 547, A82
Miller, A. A., Yao, Y., Bulla, M., et al. 2020, ApJ, 902, 47
Modjaz, M., Li, W., Butler, N., et al. 2009, ApJ, 702, 226
Modjaz, M., Liu, Y. Q., Bianco, F. B., & Graur, O. 2016, ApJ, 832, 108
Nordin, J., Brinnel, V., Giomi, M., et al. 2019, TNSTR, 2019-1202, 1
Nordin, J., Brinnel, V., Giomi, M., et al. 2020, TNSTR, 2020-1112, 1
Oke, J. B., Cohen, J. G., Carr, M., et al. 1995, PASP, 107, 375
Oke, J. B., & Gunn, J. E. 1982, PASP, 94, 586
Omand, C. M. B., & Sarin, N. 2024, MNRAS, 527, 6455
Pastorello, A., Smartt, S. J., Botticella, M. T., et al. 2010, ApJL, 724, L16
Patterson, M. T., Bellm, E. C., Rusholme, B., et al. 2019, PASP, 131, 018001
Perley, D. A. 2019, PASP, 131, 084503
Perley, D. A., Fremling, C., Sollerman, J., et al. 2020, The Astrophysical Journal, 904, 24
Phillips, M. M. 1993, ApJL, 413, L105
Pian, E., Mazzali, P. A., Masetti, N., et al. 2006, Natur, 442, 1011
Piascik, A. S., Steele, I. A., Bates, S. D., et al. 2014, Proc. SPIE, 9147, 91478H
Poznanski, D., Ganeshalingam, M., Silverman, J. M., & Filippenko, A. V. 2011, MNRAS, 415, L81
Prentice, S. J., Mazzali, P. A., Pian, E., et al. 2016, MNRAS, 458, 2973
Pritchard, T. A., Bensch, K., Modjaz, M., et al. 2021, ApJ, 915, 121
Prochaska, J. X., Hennawi, J., Cooke, R., et al. 2019, pypeit/PypeIt: Releasing for DOI, v0.11.0.1, Zenodo, doi: 10.5281/zenodo.3506873
Quimby, R. M., Kulkarni, S. R., Kasliwal, M. M., et al. 2011, Natur, 474, 487
Rodríguez, Ó., Maoz, D., & Nakar, E. 2023, ApJ, 955, 71
Rodríguez, Ó., Nakar, E., & Maoz, D. 2024, Natur, 628, 733
Rho, J., Evans, A., Geballe, T. R., et al. 2021, ApJ, 908, 232
Richardson, D., Jenkins, R. L. I., Wright, J., & Maddox, L. 2014, AJ, 147, 118
Rigault, M., Neill, J. D., Blagorodnova, N., et al. 2019, A&A, 627, A115
Roberson, M. S., Fremling, C., & Kasliwal, M. M., 2021 DBSP_DRP: DBSP Data Reduction Pipeline, Astrophysics Source Code Library, ascl:2108.020
Roming, P. W. A., Kennedy, T. E., Mason, K. O., et al. 2005, SSRv, 120, 95
Rossi, A., Rothberg, B., Palazzi, E., et al. 2022, ApJ, 932, 1
Ryan, G., van Eerten, H., Piro, L., & Troja, E. 2020, ApJ, 896, 166
Sanders, N. E., Soderberg, A. M., Levesque, E. M., et al. 2012, ApJ, 758, 132
Sarin, N., Hübner, M., Omand, C. M. B., et al. 2023, Monthly Notices of the Royal Astronomical Society, 531, 1203
Sauer, D. N., Mazzali, P. A., Deng, J., et al. 2006, MNRAS, 369, 1939
Schlafly, E. F., & Finkbeiner, D. P. 2011, ApJ, 737, 103
Schulze, S., Yaron, O., Sollerman, J., et al. 2021, ApJS, 255, 29
Smartt, S. J., Valenti, S., Fraser, M., et al. 2015, A&A, 579, A40
Smith, R. J., Piascik, A. S., Steele, I. A., & Barnsley, R. M. 2016, Proc. SPIE, 9913, 991317
Soderberg, A. M., Nakar, E., Berger, E., & Kulkarni, S. R. 2006, ApJ, 638, 930
Sollerman, J., Kozma, C., Fransson, C., et al. 2000, ApJL, 537, L127
Sollerman, J., Yang, S., Perley, D., et al. 2022, A&A, 657, A64
Srinivasaragavan, G. P., O'Connor, B., Cenko, S. B., et al. 2023, ApJL, 949, L39
Srinivasaragavan, G. P., Swain, V., O'Connor, B., et al. 2024, ApJL, 960, L18
Stanek, K. Z., & Kochanek, C. S. 2020, TNSTR, 2020-3922, 1
Steele, I. A., Smith, R. J., Rees, P. C., et al. 2004, Proc. SPIE, 5489, 679
Stritzinger, M. D., Taddia, F., Burns, C. R., et al. 2018, A&A, 609, A135
Tachibana, Y., & Miller, A. A. 2018, PASP, 130, 128001
Taddia, F., Sollerman, J., Fremling, C., et al. 2019, A&A, 621, A71
Taddia, F., Sollerman, J., Leloudas, G., et al. 2015, A&A, 574, A60
Taddia, F., Stritzinger, M. D., Bersten, M., et al. 2018, A&A, 609, A136
Tanga, M., Krühler, T., Schady, P., et al. 2018, A&A, 615, A136
Tartaglia, L., Sollerman, J., Barbarino, C., et al. 2021, A&A, 650, A174
Tonry, J., Denneau, L., Heinze, A., et al. 2019, TNSTR, 2019-1623, 1
Tonry, J., Denneau, L., Heinze, A., et al. 2020, TNSTR, 2020-3692, 1
Tonry, J., Denneau, L., Heinze, A., et al. 2021a, TNSTR, 2021-771, 1
Tonry, J., Denneau, L., Heinze, A., et al. 2021b, TNSTR, 2021-1406, 1
Tucker, M. A. 2021a, TNSCR, 2021-865, 1
Tucker, M. A. 2021b, TNSCR, 2021-1718, 1
van der Walt, S., Crellin-Quick, A., & Bloom, J. 2019, JOSS, 4, 1247
Wei, J., Cordier, B., Antier, S., et al. 2016, arXiv:1610.06892
Weiler, K. W., Panagia, N., & Montes, M. J. 2001, ApJ, 562, 670
Williamson, M., Modjaz, M., & Bianco, F. 2019, The Astrophysical Journal Letters, 880, 9
Woosley, S. E., Zhang, W., & Heger, A. 2003, in From Twilight to Highlight: The Physics of Supernovae, ed. W. Hillebrandt & B. Leibundgut (Springer), 87
Yang, S., & Sollerman, J. 2023, The Astrophysical Journal Supplement Series, 269, 18
Yaron, O., & Gal-Yam, A. 2012, PASP, 124, 668
Yoon, S.-C., Woosley, S. E., & Langer, N. 2010, ApJ, 725, 940
Yuan, W., Zhang, C., Chen, Y., & Ling, Z. 2022, in Handbook of X-ray and Gamma-ray Astrophysics (Springer), 86
Zhang, T., Li, W., Tan, H., et al. 2019, TNSTR, 2019-1699, 1
Zheltoukhov, S., Dodin, A., Tatarnikov, A., et al. 2020, TNSCR, 2020-3946, 1